AD-A282 038

DYNAMIC PROCESSES AT THE OUTER BOUNDARY OF THE MAGNETOSPHERE, INCLUDING COUPLING TO THE IONOSPHERE

Bengt U. Ö. Sonnerup
William Lotko

Dartmouth College
Thayer School of Engineering
Hanover, NH   03755-8000

DTIC
ELECTE
JUN 2 8 1994
S F D

15 April 1994

Final Report
15 January 1990 - 31 March 1994

94-19531
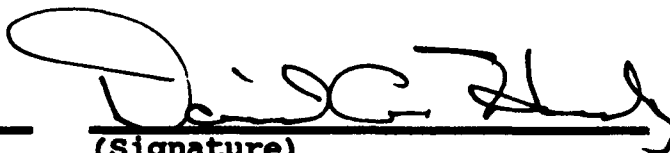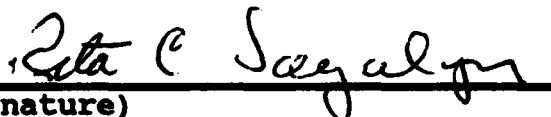
94 6 27 002

"This technical report has been reviewed and is approved for publication"

(Signature)
(Signature)
Paul Rothwell
Contract Manager

(Signature)
(Signature)
David Hardy
Branch Chief

(Signature)
(Signature)
Rita Sagalyn
Division Director

This report has been reviewed by the ESC Public Affairs Office (PA) and is releasable to the National Technical Information Service (NTIS).

Qualified requestors may obtain additional copies from the Defense Technical Information Center (DTIC). All others should apply to the National Technical Information Service (NTIS).

If your address has changed, if you wish to be removed from the mailing list, or if the addressee is no longer employed by your organization, please notify PL/TSI, 29 Randolph Road, Hanscom AFB, MA, 01731-3010. This will assist us in maintaining a current mailing list.

Do not return copies of this report unless contractural obligations or notices on a specific document requires that it be returned.

REPORT DOCUMENTATION PAGE

1. AGENCY USE ONLY (Leave blank)	2. REPORT DATE	3. REPORT TYPE AND DATES COVERED
	15 April 1994	Final (15 Jan 1990–31 Mar 1994)

4. TITLE AND SUBTITLE

Dynamic Processes at the Outer Boundary of the Magnetosphere, Including Coupling to the Ionosphere

5. FUNDING NUMBERS

PE 61102F
PR 2311 TA G5 WU JC
Contract F19628-90-K-0009

6. AUTHOR(S)

Bengt U.O. Sonnerup
William Lotko

7. PERFORMING ORGANIZATION NAME(S) AND ADDRESS(ES)

Dartmouth College
Thayer School of Engineering
Hanover, NH 03755-8000

8. PERFORMING ORGANIZATION REPORT NUMBER

9. SPONSORING/MONITORING AGENCY NAME(S) AND ADDRESS(ES)

Phillips Laboratory
29 Randolph Road
Hanscom AFB, MA 01731-3010

Contract Manager: Paul Rothwell/GPSG

10. SPONSORING/MONITORING AGENCY REPORT NUMBER

PL-TR-94-2121

11. SUPPLEMENTARY NOTES

12a. DISTRIBUTION/AVAILABILITY STATEMENT

Approved for public release; distribution unlimited

12b. DISTRIBUTION CODE

13. ABSTRACT (Maximum 200 words) Three numerical models relevant to the Earth's low-latitude boundary layer (LLBL) and its coupling to the dayside auroral ionosphere have been developed: (1) A self-consistent steady state model of the equatorial portion of the LLBL, located immediately Earthward of the magnetopause, in which dense plasma of magnetosheath origin flows in the antisolar (tailward) direction across closed geomagnetic field lines. The flow, which is compressible, is controlled by inertia forces, pressure forces, viscous forces and electromagnetic (jxB) forces associated with coupling to the ionosphere via field-aligned "Region 1" currents. The boundary layer approximation is used, and the magnetic field is calculated in a self-consistent manner from the currents, the result being field lines of parabolic shape in the LLBL; (2) A self-consistent model of the narrow layers that connect the equatorial LLBL to the northern and southern ionospheres. In these layers inertia, pressure, and viscous forces are negligible so that the field configuration must be force free: jxB = 0. This model should be connected, ultimately, to the equatorial LLBL model at the height above and below the equatorial plane where the plasma pressure in the LLBL has dropped off to its ambient magnetospheric value. The combined model would then be able to predict the total magnetic-field line draping in the (OVER)

14. SUBJECT TERMS

Magnetopause
Low Latitude Boundary Layer
Field Aligned Currents
Tearing Instability
Kelvin-Helmholtz
Instability

15. NUMBER OF PAGES

114

16. PRICE CODE

17. SECURITY CLASSIFICATION OF REPORT	18. SECURITY CLASSIFICATION OF THIS PAGE	19. SECURITY CLASSIFICATION OF ABSTRACT	20. LIMITATION OF ABSTRACT
Unclassified	Unclassified	Unclassified	SAR

CONT OF BLOCK 13:

region just Earthward of the magnetopause where current magnetic field models are unreliable; (3) A three-dimensional time-dependent simulation model of Kelvin-Helmholtz (KH) instability in the LLBL, including the effects of parabolic field lines with different curvature in different parts of the layer. The simulations indicate that the KH instability can be severely suppressed by this curved field geometry. When the instability does develop, it leads to three-dimensional vortex/current structures that may be related to auroral bright spots. In addition, the properties of the resistive tearing mode instability at the subsolar magnetopause have been investigated theoretically, the principal new element being the presence of stagnation point flow in the unperturbed equilibrium and also viscosity. It is estimated that the subsolar region may sometimes be stable or only weakly unstable. Finally, spacecraft data from AMPTE/IRM have been studied in an effort to explain the occasional occurrence of magnetic field maxima in the LLBL. It is found that two distinct effects may lead to such maxima: (i) a depression within the layer of medium-energy ions of magnetospheric origin; (ii) field curvature effects associated with undulations of the magnetopause itself.

Accesion For

NTIS CRA&I	✓
DTIC TAB	
Unannounced	
Justification	

By

Distribution /

Availability Codes

| Dist | Avail and / or Special |
| A-1 | |

CONTENTS

OVERVIEW OF RESEARCH

1. Introduction

The research conducted under this contact has been concerned principally with the development of numerical models of the Earth's low-latitude boundary layer (LLBL), a thin layer of antisunward flowing plasma, located immediately Earthward of the equatorial magnetopause current layer which marks the outer boundary of the Earth's magnetic field. The work has been concentrated in five areas:

1. Development of a self-consistent steady-state numerical model of the equatorial portion of the LLBL on closed field lines, including coupling to the ionosphere via field-aligned currents.

2. Development of a self-consistent numerical model of the force-free boundary layer that provides the link between the equatorial LLBL and the dayside auroral ionosphere.

3. Examination, by use of numerical simulation, of the stability of laminar flow in the equatorial LLBL in the presence of coupling to the ionosphere and associated nonuniform bending of the magnetic field lines in the LLBL.

4. Examination of resistive tearing-mode instability in a current sheet with equilibrium viscous stagnation-point flow.

5. Examination of magnetic-field maxima observed in the low-latitude boundary layer.

In the following sections of the report, a brief summary and discussion of the results obtained in each area is provided. Details of the research are provided in five papers, three that have been published and two more that have been submitted for publication. Also provided are appropriate extracts from E. Drakou's Ph.D. thesis which is concerned with the LLBL model and was developed with principal support from the present contract. All of these documents are appended to, and form an integral part of, this final report. The research described in the five papers has also received partial support from other sources, as indicated in their acknowledgment sections.

1

2. Numerical Model of the Equatorial Low-Latitude Boundary Layer on Closed Field Lines

The low-latitude boundary layer (LLBL) is a narrow region, located in the low latitude region immediately inside the outer boundary of the magnetosphere, the magnetopause. The LLBL contains plasma, mostly of magnetosheath origin, that flows along the layer in the antisolar direction at a speed comparable to the magnetosheath flow speed. This plasma flow is at an angle — in the simplest model at a 90° angle — to the geomagnetic field in the vicinity of the equatorial plane and thus it has an associated convection electric field, E_e, which is projected, in part at least, into the ionosphere at the footpoints of the geomagnetic field lines threading the LLBL. This impressed electric field, E_i, drives a horizontal Pedersen current, J_i, in the ionosphere; the divergence in E_i gives rise to a corresponding divergence in this horizontal current, i.e., it gives rise to a corresponding magnetic-field-aligned current into or out of the ionosphere. This field-aligned current connects the ionosphere to the LLBL, where it is again deflected to form a current J_e that flows across the equatorial geomagnetic field. In the ionosphere, the product $E_i \cdot J_i > 0$, whereas in the LLBL the product $E_e \cdot J_e < 0$; thus the former region acts as an electrical load and the latter region as an electrical generator, connected to the ionospheric load via the field-aligned currents. In the simplest conceptual model, the projection of the equatorial electric field into the ionosphere occurs by assuming the geomagnetic field lines to be equipotentials. In more realistic modeling, a potential drop, $\Delta\Phi_{\parallel}$, along the field lines is incorporated via a field-aligned conductance K, so that $J_{\parallel} = K\Delta\Phi_{\parallel}$. In the post-noon LLBL, the field-aligned current, $J_{\parallel}$, flows out of the post-noon ionosphere so that the potential drop $\Delta\Phi_{\parallel}$ can accelerate electrons precipitating into the ionosphere to energies comparable to those needed to explain auroral emissions. On the pre-noon side, a potential drop $\Delta\Phi_{\parallel}$ will accelerate electrons upwards and ions downwards instead. A schematic drawing of the dawnside LLBL configuration and its coupling to the ionosphere is shown in Figure 1. The equatorial portion of the LLBL, in which plasma inertia, pressure and viscosity are important, is located in the region $|z| \leq H$. The force-free coupling region, where the currents are entirely field aligned, connects to the LLBL at $|z| = H$ and then extends along magnetic field lines into the northern and southern ionospheres. Note that the main field-aligned current associated with the LLBL provides the portion of the so-called Region 1 current that is observed to flow into the pre-noon (8 - 12 LT, say) and out of the post-noon (12 - 16 LT, say) sides of the dayside auroral oval. Any field-aligned return current, at the outer edge of the LLBL, i.e., at the magnetopause itself, could correspond to the so-called NBZ currents, observed at low altitudes during conditions of northward interplanetary magnetic field (IMF). Note also that the actual local time extent of the LLBL projection into the ionosphere is unknown a priori and must be calculated in a self-consistent manner from the currents in the LLBL and in the coupling region.

2
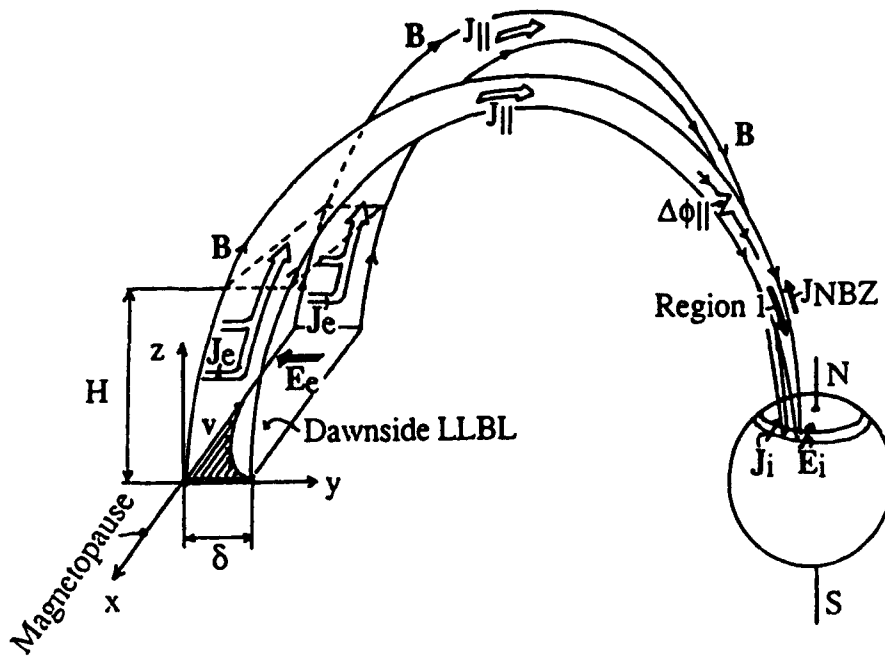
Figure 1. View from the sun of the dawnside low-latitude boundary layer and its coupling to the dayside auroral oval. Coordinates (x,y,z) are the usual GSM coordinates.

Finally, it is emphasized that the boundary layer is assumed to be located on closed geomagnetic field lines, i.e., field lines that have both ends rooted in the Earth. There is observational evidence that, at least during periods of southward interplanetary magnetic field (IMF), the portion of the LLBL immediately adjoining the subsolar magnetopause is on open field lines as a result of reconnection. The model developed under this contract does not apply to this portion but it would apply to any remaining part of the subsolar LLBL, which is on closed field lines: in such a situation, the outer edge of the LLBL described by the model would be located at the first closed field line (i.e., the inner separatrix of the reconnection configuration) rather than at the magnetopause itself. For northward IMF it is expected that most or all of the LLBL will be on closed field lines; this may also be the case on the magnetospheric flanks, regardless of IMF direction.

The model of the equatorial portion of the LLBL that has been developed under the present contract is an outgrowth of earlier one-dimensional analytic descriptions of the LLBL on closed field lines, developed by Sonnerup [1980], Lotko et al. [1987] and, in particular, Phan et al. [1989]. The new model is numerical rather than analytic. It represents the simplest possible extension of the Phan et al. model to include evolution of boundary layer structure and thickness in the main flow direction (-x) along the magnetopause. From a computational viewpoint the model is two dimensional in the sense that the equations describe behavior in the equatorial (xy) plane. However, variations with the third coordinate (z) are described to lowest order, including a self-

consistently calculated bending of the magnetic field lines in the xz plane as well as diamagnetic changes of the field component B_z. This field deformation results from currents flowing in the y direction across the boundary layer and being gradually deflected to field-aligned currents that flow into the ionosphere; diamagnetic currents also flow in the x direction. The height, H, (in the z direction) of the boundary layer above and below the equatorial plane should also be allowed to be a function of x and y, rather than being constant as in the Phan et al. model, although this feature has not yet been incorporated. The condition that should be used to determine H is that, at $z = \pm H$, the boundary-layer plasma pressure has dropped off to its ambient magnetospheric value.

The model, which is described in detail in Appendix 1, is based on four important simplifications of the full 3D MHD equations: (1) steady flow; (2) the boundary layer approximation $\partial/\partial y >> \partial/\partial x$ which leads to kinematic treatment of the transverse (y) motion and to neglect of magnetopause curvature effects; (3) kinematic treatment of the plasma motion in the $\pm z$ direction towards or away from the equatorial plane; (4) division of the model into three modules, namely the equatorial LLBL module (the current generator), the force-free coupling module, and the ionospheric module (the resistive load). At present, each module contains only the simplest description of the most important physics. As mentioned already, self-consistent variations of pressure, density and magnetic field with the coordinate z are included but the main computation is in effect two-dimensional, dealing only with quantities evaluated at z=0. The equations governing the complete model are

$$\rho_0 v_0 \cdot \nabla v_x = - dP_\infty(x)/dx + B_{z0}B_{x1}/\mu_0 H_r + (\partial/\partial y)(\eta \partial v_x/\partial y), \tag{1}$$

$$p_0 + B_{z0}^2/2\mu_0 = P_\infty(x), \tag{2}$$

$$H(x,y)/H_r = \{2\mu_0[p_0(x,y) - p_\infty(x)]/B_{x1}^2(x,y)\}^{1/2}, \tag{3}$$

$$\nabla \cdot (\rho_0 H v_0) = 0, \qquad \nabla \cdot (B_{z0} v_0) = 0, \qquad v_0 \cdot \nabla(p_0/\rho_0^\gamma) = 0. \tag{4}$$

The quantities ρ_0, p_0 and B_{z0}, along with the velocity $v_0 = (v_x, v_y, 0)$ are evaluated in the equatorial plane; $p_\infty(x)$ is the magnetospheric plasma pressure, η is the viscosity (which may be of either microscopic or turbulent origin), and $B_x(x,y,z) = B_{x1}(x,y)(z/H_r)$, H_r being a constant reference value of H. This z dependence of B_x leads to approximately parabolic field lines in the model, with field-line curvature that varies with the coordinate y, being a maximum at the magnetopause and then decreasing as one moves further Earthward. In order, the above equations express: momentum/force balance in the x, y, and z directions (the expression for H(x,y) given in the third equation is derived from $p + B_x^2/2\mu_0 = p_0(x,y)$); mass conservation; flux conservation; and isentropic compression/expansion, respectively. To these equations are added $j \times B = 0$ in the coupling module, and the ionospheric laws $j_{\parallel i} = K(\Phi_e - \Phi_i) \equiv K\Delta\Phi_\parallel$, and $\partial/\partial y(\Sigma_p \partial \Phi_i/\partial y) = - j_{\parallel i}$,

4

where $\Phi_e(x,y,H)$ and $\Phi_i(x_i,y_i)$ are the potential distributions in the LLBL and in the ionosphere, respectively. In the simplified version of the model produced under this contract, the LLBL height H is constant, the conductance, K, along field lines is infinite, and the ionospheric conductivity, Σ_p, is constant. Relations between the coordinates (x,y) and (x_i,y_i), expressed via mapping factors, can be calculated self-consistently in the coupling region, although in the current version of the model the mapping factors are taken to be constant. In other words, the magnetic field configuration in the LLBL itself, as well as in the force-free coupling region, would ultimately be computed self consistently (albeit in the boundary layer approximation). Thus, a complete version of the model would provide an accurate mapping along B from the ionosphere to the equatorial plane. The field from a realistic model of the inner magnetospheric B field (e.g., one of the Tsyganenko models) would then be used as a boundary condition at the magnetospheric edge of the LLBL computational box. The mapping in the coupling region and the interface with a suitable magnetospheric field model are described in Section 3 and in Appendix 5.

The boundary layer equations are parabolic and are therefore integrated by use of a marching procedure (in the -x direction) that allows one to follow the development of the layer for as large distances in the flow direction as available computer resources permit. Since the downstream state obtained from one run can be used as the upstream state for a second run, etc., the boundary layer evolution can in principle be followed to arbitrarily large distances along the magnetospheric flank. One of the difficulties associated with the numerical marching procedure is that it cannot handle reversals in the main flow direction, i.e., in the velocity component v_x. This difficulty is associated with the inertia term $\rho v_x \partial v_x / \partial x$, which does not reverse sign when v_x reverses sign. The situation is similar to the integration of a diffusion equation backwards in time which is numerically unstable. This problem has been overcome in the present code by neglecting inertia near the flow reversal and in the entire region of slow sunward flow on the magnetospheric side of the LLBL. Furthermore, in the present version of the code, the velocity profile, $v_x(x,y)$, in the slow-flow region is obtained analytically by assuming that the plasma properties and the field component B_z have reached their asymptotic magnetospheric values in this region. In other words, they depend on x but not on y. This procedure decreases the size, along y, of the computational domain, thus providing for substantial computational economy. Benchmark tests (Appendix 4) in which solutions from the program are checked against certain exact self-similar solutions indicate that the procedure adopted provides satisfactory accuracy.

Details of the numerical procedure, along with benchmark tests and a discussion of various generalizations of the model, are given in Appendices 3, 4 and 2, respectively.

Sample results from a test run of the numerical code (with H = const, $\Delta\Phi_{\parallel} = 0$ and constant mapping factors, which represents its current status) are shown in Figure 2. A complete presentation of results to date is given in the article by Drakou et al. [1994] which is reproduced in Appendix 1.
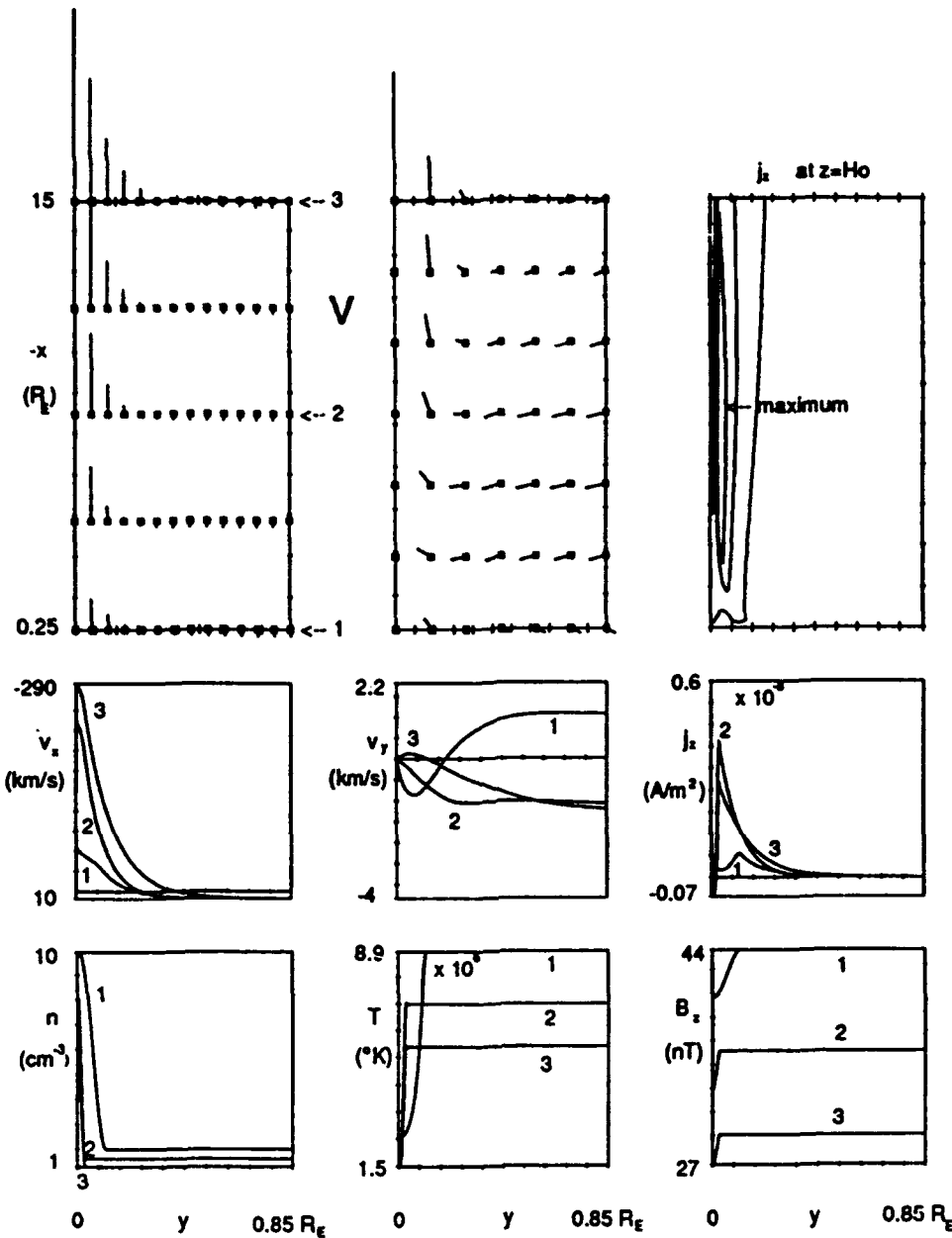
Figure 2. Results of trial run, using the present boundary layer model.

The boundary conditions used in Figure 2 include an accelerating tailward plasma flow speed, $v_x(x,0)$, at the magnetopause, a small constant sunward convection speed, $v_{x\infty}$, in the magnetosphere, where plasma number density, n_∞, pressure, p_∞, and temperature, T_∞, as well as B_z field component, $B_{z\infty}$, all decrease with increasing distance, -x, down the tail. Viscosity, assumed in this run to be proportional to ρ/B, is included. Entrainment by the LLBL of magnetospheric plasma is illustrated in the top middle panel where the v_y velocity component has been artificially augmented in order to make the effect visible. Viscous widening of the velocity profile $v_x(x,y)$ is seen in the middle left panel, whereas, n, T, and B_z (bottom panels) have profile

6

widths that decrease as one moves downstream. The field-aligned current shows considerable structure (middle right panel) and substantial evolution (top right panel) in the flow direction. Note in particular that a maximum in j_z occurs at a particular x value, i.e., at a particular local time; such a maximum has indeed been reported in the observational study by Iijima and Potemra [1978]. These results are shown here for illustrative purposes only; their details are expected to change considerably when additional features such as field-aligned potential drops are incorporated.

3. Numerical Model of the Force-Free Coupling Module

In the narrow region that connects the equatorial LLBL to the ionosphere, the plasma density, pressure, and velocity are sufficiently small and the magnetic field intensity sufficiently high so that the electric currents connecting the LLBL to the ionosphere must be field-aligned to a high degree of accuracy. Thus the basic governing equations in this region are

$$\mathbf{j} \times \mathbf{B} = 0, \qquad \mathbf{j} = (1/\mu_0)\nabla \times \mathbf{B}, \qquad \nabla \cdot \mathbf{B} = 0. \qquad (5)$$

These equations lead to

$$\mu_0 \mathbf{j} = \alpha(x,y,z)\mathbf{B} = \nabla \times \mathbf{B} \qquad (6)$$

where α is a proportionality factor which has a constant value along any magnetic field line so that

$$\mathbf{B} \cdot \nabla \alpha = 0 \qquad (7)$$

The latter two relations have been simplified by use of the boundary layer approximation (described in Section 2) and a computer code has been developed for generating self-consistent current and magnetic field configurations in the connection layer. Boundary conditions for the code consist of specification of the magnetic field at the Earthward edge of the layer by use of an empirical magnetospheric field model such as one of the Tsyganenko models and specification of a field-aligned current distribution and magnetic field at the interface to the LLBL at $|z| = H$ (alternatively, these quantities can be specified in the ionosphere). Ultimately, this code should be appended to the main LLBL code described in Section 2 but this step has not yet been taken. When the two codes have been combined, the resulting code will be able to give accurate information about the magnetic field mapping in the regions immediately Earthward of the magnetopause where existing field models such as the various Tsyganenko models fail to provide reliable information. However, the utility of the force-free boundary layer module is not restricted to the LLBL: it has independent applications to any field-aligned current sheets in the magnetosphere.

A detailed description of the force-free boundary layer model is provided in Appendix 5, along with a benchmark test and a simple application using measured Region 1 currents above the ionosphere [Iijima and Potemra, 1978] in conjunction with a dipolar magnetospheric field. These results suggest typical azimuthal deflections of dayside magnetic field lines in the range 21–26°.

7

4. Kelvin-Helmholtz Instability in the Low-Latitude Boundary Layer

The stability of the plasma flow in the LLBL is of importance for the construction of any realistic model of this layer. Stable behavior implies that any transport of momentum or mass across the layer is caused by microscopic plasma processes while unstable behavior implies transport by eddy viscosity and eddy diffusivity. To date, studies of the Kelvin-Helmholtz (KH) instability relevant to the LLBL have assumed the unperturbed magnetic field lines to be straight. However, in a realistic model of this layer, the currents flowing across it and being gradually deflected into field-aligned currents, as the Earthward edge of the layer is approached, produce bending of the field lines into approximately parabolic shapes with vertices pointing in the (antisolar) flow direction (see Figure 5 of Appendix 1). Parabolas close to the magnetopause have larger curvature than those close to the magnetospheric edge of the LLBL so that one may expect interchange motions to be impeded.

We have carried out a fully three-dimensional simulation of a velocity shear layer of the hyperbolic tangent type in the presence of coupling to the northern and southern ionospheres, represented in the simulation model by two parallel electrically conducting plates. The current system produced by this coupling leads to parabolic field lines of opposite curvature on the two sides of the shear layer.

The results of the simulation are reported in detail in Appendix 6. In brief, it is found that the field line curvature, if substantial, may severely suppress the KH instability. When the curvature is less strong, as in the dayside LLBL, the instability proceeds albeit at a somewhat reduced rate compared to the case of straight field lines transverse to the flow, and leads to the formation of three-dimensional vortex/current structures that may be related to observed auroral bright spots.

5. Resistive Tearing Mode

The behavior of the resistive tearing mode near the subsolar magnetopause has been investigated with the objective of finding out how the presence of stagnation point flow and viscosity influence this instability. The unperturbed equilibrium is an exact solution of the incompressible MHD equations, including resistivity and viscosity so that the stability properties can be investigated even for small magnetic and viscous Reynolds numbers where the traditional tearing mode analysis is invalid. The results indicate stability of the tearing mode for magnetic Lundquist numbers, S, (based on the Alfvén speed) less than 12.25, regardless of viscous Reynolds number, Re, and for $S \leq 18.3$ when $Re = 0$. For large values of S and Re, the classical asymptotic growth rates of Furth, Killeen and Rosenbluth are recovered. It is also found that the stagnation point flow stabilizes long wavelength perturbations so that the tearing mode has a cut-off at small as well as at large wave numbers. The main effect of viscosity is to reduce the growth

rate of the instability, in particular at short wavelengths. The stabilization at low magnetic Reynolds numbers is relevant to the subsolar magnetopause where estimates of S are in the range 2 < S < 100 [Lee and Fu, 1986].

6. Magnetic Field Maxima in the LLBL

It has been known for a long time that the magnetic field often exhibits a maximum immediately Earthward of the magnetopause instead of the minimum one would expect from the diamagnetic effect of the dense plasma in the LLBL. We have investigated this effect by use of plasma and magnetic field data from the AMPTE/IRM spacecraft and find two fundamentally different causes for the excess field: (i) a depression within the LLBL of the density of medium energy ions of magnetospheric origin and (ii) field curvature effects associated with undulations of the magnetopause itself. When case (i) is at hand, medium-energy electron fluxes are also depressed, suggesting that the field lines in the LLBL may have been open. However, this is not the only possible explanation for the absence of energetic particles.

7. References

Drakou, E., B.U.Ö. Sonnerup, and W. Lotko, Self-consistent steady state model of the low latitude boundary layer, *J. Geophys. Res.*, *99*, 2351, 1994.

Iijima, T. and T.A. Potemra, Large-scale characteristics of field-aligned currents associated with substorms, *J. Geophys. Res.*, *83*, 599, 1978.

Lee, L.C. and Z.F. Fu, Collisional tearing instability in the current sheet with a low magnetic Lundquist number, *J. Geophys. Res.*, *91*, 3311, 1086.

Lotko, W., B.U.Ö. Sonnerup, and R.L. Lysak, Nonsteady boundary layer flow including ionospheric drag and parallel electric fields, *J. Geophys. Res.*, *92*, 8635, 1987.

Phan, T.-D., B.U.Ö. Sonnerup, and W. Lotko, Self-consistent model of the low latitude boundary layer, *J. Geophys. Res.*, *94*, 1281, 1989.

Sonnerup, B.U.Ö., Theory of the low-latitude boundary layer, *J. Geophys. Res.*, *85*, 2017, 1980.

8. Students Supported

•T.-D. Phan	Ph.D. (March, 1991)	•V. Galinsky	Ph.D. (Expected June, 1995)
•K. Vatan,	M.S. (June, 1993)		
•E. Drakou	Ph.D. (December, 1993)	•L.-N. Hau	Postdoctoral Fellow

9. Papers Published or Submitted

1. Self-Consistent Steady-State Model of the Low-Latitude Boundary Layer, E. Drakou, B.U.Ö. Sonnerup, and W. Lotko, *J. Geophys. Res.*, *99*, 2352, 1994.
2. Force-Free Boundary Layer Model for Mapping Field-Aligned Currents, K. Vatan, W. Lotko, and B.U.Ö. Sonnerup, submitted to *J. Geophys. Res.*, March, 1994.
3. Dynamics of Shear Velocity Layer with Bent Magnetic Field Lines, V.L. Galinsky and B.U.Ö. Sonnerup, submitted to *Geophys. Res. Lett.*, April, 1994.
4. Resistive Tearing-Mode Instability in a Current Sheet with Equilibrium Viscous Stagnation-Point Flow, T.-D. Phan and B.U.Ö. Sonnerup, *J. Plasma Phys.*, *46*, 407, 1991.
5. Magnetic Field Maxima in the Low-Latitude Boundary Layer, B. Sonnerup, G. Paschmann, T.-D. Phan, and H. Lühr, *Geophys. Res. Lett.*, *19*, 1727, 1992.

10. Presentations

B. Sonnerup, The Magnetopause During Reconnection: A Review, Workshop on Magnetic Fluctuations, Diffusion, and Transport in Geoplasmas, MIT, Summer, 1990. (INVITED)

W. Lotko, Connecting the Boundary Electrically to the Dayside Ionosphere, AGU Fall Meeting, December, 1990. (INVITED)

E. Drakou, B. Sonnerup, and W. Lotko, Self-Consistent Model of the Low-Latitude Boundary Layer, AGU Spring Meeting, May, 1991. (POSTER)

W. Lotko, Low-Latitude Boundary Layer Model - Structure, Signatures and Mapping, GEM Workshop, UCLA, September, 1991. (INVITED)

W. Lotko, B. Sonnerup, E. Drakou and K. Vatan, Coupling of the Low-Latitude Boundary Layer to the Ionosphere, AGU Fall Meeting, December, 1991. (INVITED)

B. Sonnerup and W. Lotko, Status Report on the Dartmouth Low-Latitude Boundary Layer Model, Review Meeting for Air Force Magnetospheric Specification and Forecast Model, Rice University, March, 1992. (INVITED)

B. Sonnerup, The Magnetospheric Low-Latitude Boundary Layer, AGU Spring Meeting, May, 1992. (INVITED)

E. Drakou, B.U.Ö. Sonnerup, and W. Lotko, Self-Consistent Three-Dimensional Compressible Model of the Low Latitude Boundary Layer, American Geophys. Union, Spring Meeting, May, 1992. (POSTER)

K. Vatan, W. Lotko, and B.U.Ö. Sonnerup, Force-Free Boundary Layer Model for Mapping Field-Aligned Currents, American Geophys. Union, Spring Meeting, May, 1992. (POSTER)

T.-D. Phan, G. Paschmann, W. Baumjohann, N. Sckopke, B.U.Ö. Sonnerup, and H. Lühr, The Dayside Magnetopause and Low-Latitude Boundary Layer for Large Magnetic Shear

AMPTE/IRM Observations, American Geophys. Union, Spring Meeting, May, 1992. (POSTER)

W. Lotko, B. Sonnerup, E. Drakou, and K. Vatan, Low-Latitude Boundary Layer Model, Geospace Environment Modeling (GEM) Workshop, Snowmass, June, 1992. (POSTER)

E. Drakou, B.U.Ö. Sonnerup, and W. Lotko, Self-Consistent Three-Dimensional Model of the Low-Latitude Boundary Layer, Cambridge Workshop in Theoretical Geoplasma Physics, MIT, Cambridge, August, 1992. (POSTER)

B. Sonnerup and D. Walthour, The FTE and Some of Its Signatures, Cambridge Workshop in Theoretical Geoplasma Physics, MIT, August, 1992. (INVITED)

E. Drakou, B.U.Ö. Sonnerup, and W. Lotko, Self-Consistent Steady-State Model of the Low-Latitude Boundary Layer, AGU Fall Meeting, December 1992. (CONTRIBUTED) (This presentation was given an AGU Outstanding Student Paper Award)

E. Drakou, B.U.Ö. Sonnerup, and W. Lotko, Self-Consistent Steady-State Model of the Low-Latitude Boundary Layer, AGU Spring Meeting, May, 1993. (POSTER)

B. Sonnerup, The Magnetopause Region, Inter-Agency Consultative Group for Science (IACG), Second Workshop on "Boundaries in Collisionless Plasmas," Austria, April, 1993. (INVITED)

V.L. Galinsky and B.U.Ö. Sonnerup, Dynamics of Shear Velocity Layer with Bent Magnetic Field Lines, AGU Spring Meeting, May, 1993. (POSTER)

W. Lotko, K. Vatan, and B. Sonnerup, Mapping Region 1 Currents in a Force-Free Boundary Layer Model, Geospace Environment Modeling Workshop, Snowmass, June, 1993. (POSTER)

E. Drakou, B. Sonnerup, and W. Lotko, Self-Consistent Steady-State Model of the Low-Latitude Boundary Layer, ibid. (POSTER)

W. Lotko and B. Sonnerup, Overview of the Low-Latitude Boundary Layer, GEM Workshop, Boston College, October, 1993. (INVITED)

W. Lotko, From Collective Microprocesses to Meso-Scale Structure: Formation of Magnetospheric Boundary Layers and Auroral Arcs, AGU Fall Meeting, December, 1993. (INVITED)

W. Lotko, The Magnetospheric Boundary Layer, National Center for Atmospheric Research, High Altitude Observatory, Boulder, February, 1994. (SEMINAR)

W. Lotko, B. Sonnerup, and E. Drakou, The Low-Latitude Boundary Layer on Closed Field Lines, Chapman Conference on Physics of the Magnetopause, San Diego, March, 1994. (INVITED)

LIST OF APPENDICES

1. Self-Consistent Steady State Model of the Low-Latitude Boundary Layer, E. Drakou, B.U.Ö. Sonnerup, and W. Lotko, *J. Geophys. Res.*, 99, 2351, 1994.
2. Extensions of the Model, Chapter 3 in Ph.D. thesis entitled "Self-consistent steady state model of the low-latitude boundary layer" by E. Drakou, Dartmouth College, December, 1993.
3. Numerical Method, Chapter 4 in Ph.D. thesis by E. Drakou.
4. Benchmark Tests, Chapter 5 in Ph.D. thesis by E. Drakou.
5. Force-Free Boundary Layer Model for Mapping Field-Aligned Currents, K. Vatan, W. Lotko, and B.U.Ö. Sonnerup, submitted to *J. Geophys. Res.*, March, 1994.
6. Dynamics of Shear Velocity Layer with Bent Magnetic Field Lines, V.L. Galinsky and B.U.Ö. Sonnerup, submitted to *Geophys. Res. Lett.*, April, 1994.
7. Resistive Tearing-Mode Instability in a Current Sheet with Equilibrium Viscous Stagnation-Point Flow, T.-D. Phan and B.U.Ö. Sonnerup, *J. Plasma Phys.*, 46, 407, 1991.
8. Magnetic Field Maxima in the Low-Latitude Boundary Layer, B. Sonnerup, G. Paschmann, T.-D. Phan, and H. Lühr, *Geophys. Res. Lett.*, 19, 1727, 1992.

Self-consistent steady state model of the low-latitude boundary layer

E. Drakou,[1] B. U. Ö. Sonnerup, and W. Lotko

Thayer School of Engineering, Dartmouth College, Hanover, New Hampshire

Results are presented from a steady state numerical model of the low-latitude boundary layer (LLBL) on closed field lines and its coupling to the dayside auroral ionosphere. In the model the boundary layer approximation is used, the result being that inertial forces are taken into account only in the main flow direction ($-x$) where they are balanced by pressure forces, $j \times B$ forces, and viscous forces. Motion in the transverse directions (y and z) is treated kinematically, the force balances in these two directions being purely static. Computationally, the model is two dimensional, describing the motion of plasma and frozen-in magnetic field in the equatorial (xy) plane but allowing for lowest-order polynomial variation of some quantities with the coordinate (z) perpendicular to that plane. The plasma expands and compresses isentropically; the magnetic field is calculated self-consistently, which leads to approximately parabolic field line shape in planes parallel to the magnetopause (the xz plane), with maximum field curvature near the magnetopause edge of the LLBL. Coupling to the ionosphere via region 1 field-aligned currents is included. The effects of the ionosphere are represented by two parallel resistive plates at fixed height above and below the equatorial plane. The model can be used to investigate the influence of various physical parameters, for example, viscous and magnetic Reynolds numbers, and of boundary conditions at the magnetopause and in the magnetosphere on the LLBL development in the $-x$ direction. Special attention is given to viscous effects which, under suitable circumstances, lead to a region 1 current that first increases and then reduces with increasing longitude away from local noon. Asymptotic matching of the antisunward motion of the cool LLBL plasma to sunward convection of hot plasma in the magnetosphere is illustrated along with the entrainment of magnetospheric plasma by the antisunward LLBL flow.

INTRODUCTION

The low-latitude boundary layer (LLBL) is a narrow region of tailward flowing plasma located in the magnetosphere, immediately inside the magnetopause current sheet, at low geomagnetic latitudes. It was first observed by *Hones et al.* [1972] and *Akasofu et al.* [1973] along the flanks of the geomagnetic tail. Since then, a number of authors have discussed observational data and theoretical models of the LLBL. From these studies we know the following: the LLBL is intermittently present at almost all local times along the entire dayside portion of the magnetopause. It was also recently found to be extended to evening local times [*Woch et al.*, 1993]. Its thickness appears to increase, on average, with increasing distance from the subsolar point [*Eastman and Hones*, 1979], although the growth may be slow beyond the dawn-dusk meridian plane. A typical boundary layer thickness at that location is 0.5-1 R_E [*Eastman and Hones*, 1979; *Sckopke et al.*, 1981]. When the interplanetary magnetic field is northward, the LLBL appears thicker and is thought to be located on closed field lines, that is, on magnetic field lines that have both feet in the ionosphere [*Haerendel et al.*, 1978; *Williams et al.*, 1985; *Mitchell et al.*, 1987; *Traver et al.*, 1991]. It is this kind of LLBL we are modeling in the present paper. During periods of southward interplanetary magnetic field the situation is less clear: reconnection may dominate in which case the LLBL on closed field lines may be mostly absent. The experimental evidence in this case is not conclusive, but it indicates that the layer is par-

tially on open and partially on closed field lines: our model applies only to the part on closed field lines. As one moves inward from the magnetopause across the LLBL, the density falls from a high magnetosheath like value to a low magnetospheric value, while the magnetic field usually rises slightly (although a field enhancement is sometimes seen instead [*Sonnerup et al.*, 1992]) and the plasma pressure falls accordingly [*Sckopke et al.*, 1981]. The dense plasma in the LLBL appears to be mainly of magnetosheath origin. How this plasma enters the LLBL is not yet clear. It may leak diffusively over portions of the magnetopause surface [*Tsurutani and Thorne*, 1982] or enter onto closed field lines in the cusps [*Paschmann et al.*, 1976] or at the edges of a dayside reconnection segment of the magnetopause. It is also possible that, during northward IMF, magnetosheath flux tubes reconnect in the north and south beyond the cusps and then shorten and reorient themselves to eventually become assimilated with other magnetospheric field lines [*Dungey*, 1963; *Cowley and Owen*, 1989; *Song and Russell*, 1992]. As noted by *Mitchell et al.* [1987], *Sckopke et al.* [1981], *Eastman and Hones* [1979], and others, the cool, dense magnetosheath like plasma in the LLBL is usually mixed to some extent with hot tenuous magnetospheric plasma.

There are also ionospheric signatures of the LLBL [*Eastman et al.*, 1976]. These signatures are controlled to a great extent by the plasma flow in the LLBL which is mostly in the antisunward direction, although a region of relatively slow sunward flow, with occasional large velocity peaks, appears to be present towards the magnetospheric edge of the layer [*Williams et al.*, 1985; *Mitchell et al.*, 1987]. The flow is mainly perpendicular to the magnetic field and therefore creates an electric field across the LLBL. The resulting electric potential differences map, at least approximately, along the magnetic field lines to the ionosphere where they drive horizontal ionospheric currents. Where the ionospheric electric field changes with latitude, the above currents have to be partially deflected into field-aligned currents, thus forming the dayside part

---

[1]Now at Herzberg Institute of Astrophysics, National Research Council of Canada, Ottawa, Ontario.

of the region 1 current system [Iijima and Potemra, 1976a, b]. These currents flow in a narrow layer into (on the eveningside) and out of (on the morningside) the LLBL, where they are again deflected to flow across the magnetic field in a direction opposite to the electric field there. In the connecting region between the ionosphere and the LLBL, field-aligned potential drops are likely to occur. In the current system described above, the LLBL acts as a magnetohydrodynamic generator while the ionosphere plays the role of a dissipator. Recent observations [Woch et al., 1993] provide added support for the notion that the LLBL is source of the dayside region 1 currents.

Compared to some other interfaces in the solar wind-magnetospheric system, relatively little theoretical work has been devoted to the LLBL. Perhaps the first qualitative theoretical model was proposed by Coleman [1971]. Eastman et al. [1976] discussed the LLBL in detail with emphasis on the role it plays in transferring mass, momentum, and energy from the solar wind to the magnetosphere. In that work, coupling to the auroral ionosphere plays an important role and the role of the LLBL as a generator is explained. Kan and Lee [1980] studied imperfect ionosphere-magnetosphere coupling in a simple evolving boundary layer, using concepts of field-aligned potential drops developed by Fridman and Lemaire [1980], Chiu and Cornwall [1980], and Lyons [1980]. Their model is nonviscous, the result being that the ionospheric drag gradually slows down the boundary layer plasma as it moves in the downstream direction. The role of viscosity in the layer was studied by Sonnerup [1980] in a one-dimensional steady state model. Lotko et al. [1987] reexamined this model by including a simple conductance law to describe the relation between field-aligned currents and field-aligned potential drops. In those papers, induced magnetic fields were not included. Wei et al. [1990] examined the formation of vortices and other turbulent structures in the LLBL caused by the Kelvin-Helmholtz instability. In their study the plasma flow was assumed incompressible, two dimensional, and time dependent and the magnetic field was taken to be constant. Their model included viscosity. Wei and Lee [1993] extended that model to include coupling to the polar ionosphere. Siscoe et al. [1991] described the coupling of the LLBL model of Lotko et al. [1987] to a high-latitude boundary layer model, and Siscoe and Maynard [1991] also included coupling to the region 2 current system.

Following the ideas of Sonnerup [1980] and Lotko et al. [1987], Phan et al. [1989] developed a fully self-consistent one-dimensional model of a viscous LLBL in which the magnetic field deformation in the layer, caused by the currents in it, is included. The present model, some aspects of which have not yet been numerically implemented, is an extension of the analysis by Phan et al. to allow for slow variations of the layer in the flow direction (the negative z direction). The boundary layer occupies the region $y \geq 0$, starting at the magnetopause ($y = 0$), where the antisunward flow velocity has a maximum value, and extending earthward into the magnetosphere, where the velocity first reverses sign and then asymptotically approaches a low sunward magnetospheric value as $y \rightarrow \infty$. The surfaces $z = \pm H_0(x, y)$ represent the northern and southern edges of the layer, where the magnetic and plasma pressures reach their magnetospheric values. The model includes self-consistent calculation of the magnetic field in the layer from the currents via Ampère's law. The normal component of the current is continuous at the surfaces $z = \pm H_0$, whereas the j_y current switches abruptly to zero there; for $|z| > H_0$ the current is field-aligned. As a result of the cross-field currents, the field lines have approximately parabolic shapes in the boundary layer. This deformation of the magnetic field along with the deformation caused by field-aligned currents in the coupling regions between $z = \pm H_0$ and

the ionosphere are important features of the model because they provide the mapping along LLBL field lines from the equatorial plane to the auroral ionosphere. However, in the simplified version of the model to be discussed here the lumped properties of the two ionospheres and the low-pressure (low plasma beta) regions between the ionospheres and the LLBL proper are replaced by resistive parallel plates located a fixed distance, $2H_0$, apart; as a consequence, the magnetic mapping is not included in a self-consistent manner and field-aligned potential drops are excluded.

The paper is organized as follows: The mathematical formulation of the model is presented in section 2 along with the assumptions and approximations used. Section 3 contains a description of the numerical procedure. In section 4 we present three runs of the numerical code, and in section 5 we summarize the results and discuss generalizations of the present model that remain to be implemented.

DEVELOPMENT OF MODEL EQUATIONS

The geometry of the system to be studied is shown qualitatively in Figure 1. Figure 1a shows the dawnside LLBL, viewed from the north ecliptic pole. The coordinate system is as follows: the y axis is across the LLBL and points inward toward the magnetosphere;
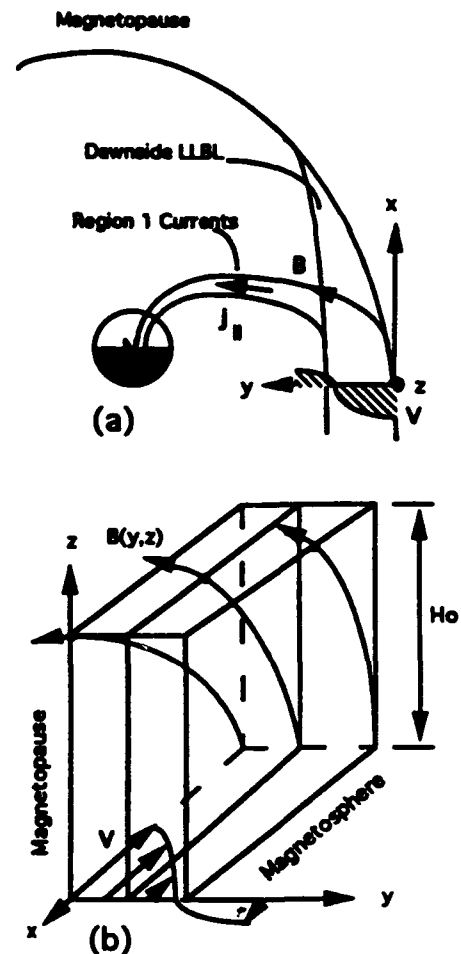
Fig. 1. Boundary layer geometry. (a) Dawnside low-latitude boundary layer on closed field lines, viewed from above the north ecliptic pole. Velocity profile across the layer is shown qualitatively, including a region of sunward flow. Region 1 field-aligned currents flow into the ionosphere. (b) View of the LLBL from the Sun: the layer extends to height H_0 above and below the equatorial plane. Parabolic magnetic field lines are shown; parabolas close to the magnetopause have larger curvature.

the x axis is directed south to north in the equatorial plane; and the z axis is perpendicular to the previous two axes and points in the upstream direction. The spanwise width of the LLBL, which is very small in comparison with the scale of the curvature of the magnetopause and geomagnetic field lines and with the scales for variation in the streamwise direction and for flaring of the magnetopause boundary, permits a simple mapping of the slab (x, y, z) coordinates of the mathematical model described below onto natural curvilinear coordinates such as (L, M, N) boundary normal coordinates. In Figure 1 a velocity profile across the layer is shown qualitatively, the main flow being in the $-x$ direction, with slow sunward flow in the magnetosphere. Closed magnetic field lines connect the LLBL to the northern and southern ionospheres. In the coupling regions, field-aligned currents occur. Figure 1b offers a view of the layer from the Sun; it indicates that the LLBL extends to a height H_0 above and below the equatorial plane in the z direction and that the magnetic field lines are bent into approximate parabolas with increasingly large curvature as the magnetopause is approached. In the current version of the model, electrically conducting planes at $z = \pm H_0$ with appropriate conductivity are used to represent the ionospheric substrate and the low-pressure regions between it and the effective high-latitude boundaries of the LLBL.

Boundary Layer Approximation

The plasma flow in the equatorial LLBL is governed by the steady state mass and momentum conservation laws, the isentropic law, the induction law, and the law of magnetic flux conservation:

$$\nabla \cdot \rho \mathbf{v} = 0 \tag{1}$$

$$\rho \mathbf{v} \cdot \nabla \mathbf{v} = -\nabla p + \frac{1}{\mu_0}(\nabla \times \mathbf{B}) \times \mathbf{B} + \nabla \cdot \underline{\tau} \tag{2}$$

$$\mathbf{v} \cdot \nabla (p/\rho^\gamma) = 0 \tag{3}$$

$$\nabla \times (\mathbf{v} \times \mathbf{B}) = 0 \tag{4}$$

$$\nabla \cdot \mathbf{B} = 0. \tag{5}$$

Here ρ, p, and $\mathbf{v}$ are the plasma density, pressure, and velocity, respectively. Also, $\underline{\tau}$ is the viscous stress tensor, $\mathbf{B}$ and μ_0 are the magnetic field and the vacuum permeability, respectively, and $\gamma = c_p/c_v$ is the ratio of specific heats. For simplicity, we have neglected resistivity as well as heat conduction and viscous dissipation in the LLBL. These effects may in reality be of some importance and should ultimately be included.

As mentioned already, the effects of the two ionospheres are represented by parallel resistive plates at fixed height $z = \pm H_0$. These plates are assumed impenetrable in the present version of the model so that $v_z = 0$ at $z = \pm H_0$. It will be shown in the next subsection that, in the approximate equations describing the LLBL, this boundary condition implies $v_z = 0$ in the entire layer, that is, for $-H_0 \leq z \leq H_0$.

The boundary layer or narrow-channel approximation is now applied to the above equations, taking advantage of the fact that changes across a narrow layer (in the y direction) occur on a scale length δ, which is much smaller than both the scale length L, for changes along the main flow direction (x), and the scale length H, for changes in the third direction (z). From the mass conservation law it then follows that, if the characteristic velocity in the x direction is V_0, the velocity in the y direction is of the order of $(\delta/L)V_0$. Similarly, from the flux conservation law it follows that if the characteristic value of B_x and of B_z is B_0, then the y compo-

nent of the magnetic field is of the order of $(\delta/L)B_0$ or $(\delta/H)B_0$. As mentioned already, another consequence of the boundary layer approximation is that the magnetopause surface curvature can be ignored if the characteristic thickness δ is much smaller than the radius of curvature, R, a condition that is well satisfied for the LLBL. Thus, neglecting terms of order δ/R compared to terms of order unity, one is allowed to use a Cartesian coordinate system and the flat geometry shown in Figure 1b. By neglecting terms of order δ^2/L^2, δ^2/HL, and δ^2/H^2 compared to terms of order unity and by setting $v_z = 0$, the three components of (2) can be written in the following approximate form:

$$\rho(v_x \frac{\partial}{\partial x} + v_y \frac{\partial}{\partial y})v_x \simeq$$

$$-\frac{\partial p}{\partial x} + \frac{1}{\mu_0} B_z(\frac{\partial B_x}{\partial z} - \frac{\partial B_z}{\partial x}) + \frac{1}{\mu_0} B_y \frac{\partial B_x}{\partial y} + \frac{\partial}{\partial y}(\eta \frac{\partial v_x}{\partial y}) \tag{6}$$

$$0 \simeq -\frac{\partial p}{\partial y} - \frac{1}{\mu_0}(B_x \frac{\partial B_x}{\partial y} + B_z \frac{\partial B_z}{\partial y}) \tag{7}$$

$$0 \simeq -\frac{\partial p}{\partial z} + \frac{1}{\mu_0} B_y \frac{\partial B_z}{\partial y} - \frac{1}{\mu_0} B_x(\frac{\partial B_z}{\partial x} - \frac{\partial B_x}{\partial z}) \tag{8}$$

In this approximation, inertia and viscous forces enter only the x component of the momentum equation; in the y and z directions the equations express a static balance between the ∇p and $\mathbf{j} \times \mathbf{B}$ forces. The motion in y is treated purely kinematically via the mass conservation law (1). The viscous term in (6) has been assumed comparable to the inertia terms, which is true provided the viscous Reynolds number, $Re = \rho V_0 L/\eta$, is of the order of L^2/δ^2; over large flow distances, one expects the boundary layer thickness to adjust itself to satisfy this condition. In the same approximation, that is, again neglecting δ^2/L^2, δ^2/LH, and δ^2/H^2, the currents in the LLBL are given by Ampère's law:

$$j_x \simeq \frac{1}{\mu_0} \frac{\partial B_z}{\partial y} \tag{9}$$

$$j_y \simeq \frac{1}{\mu_0}(\frac{\partial B_x}{\partial z} - \frac{\partial B_z}{\partial x}) \tag{10}$$

$$j_z \simeq -\frac{1}{\mu_0} \frac{\partial B_x}{\partial y} \tag{11}$$

Series Expansion in z

We proceed now to expand all quantities as power series in terms of the z variable. We assume a boundary layer symmetric with respect to the equator (the plane $z = 0$) and express each dependent variable in terms of even or odd powers of z, according to whether they are symmetric or antisymmetric with respect to the equatorial plane:

$$v_x = v_{x0}(x, y) + v_{x2}(x, y)\frac{z^2}{H^2} + \dots ;$$

$$v_y = v_{y0}(x, y) + v_{y2}(x, y)\frac{z^2}{H^2} + \dots ;$$

$$v_z = v_{z1}(x, y)\frac{z}{H} + v_{z3}(x, y)\frac{z^3}{H^3} + \dots \tag{12}$$

$$B_x = B_{x1}(x,y)\frac{z}{H} + B_{x3}(x,y)\frac{z^3}{H^3} + \cdots \;;$$

$$B_y = B_{y1}(x,y)\frac{z}{H} + B_{y3}(x,y)\frac{z^3}{H^3} + \cdots \;;$$

$$B_z = B_{z0}(x,y) + B_{z2}(x,y)\frac{z^2}{H^2} + \cdots \tag{13}$$

$$\rho = \rho_0(x,y) + \rho_2(x,y)\frac{z^2}{H^2} + \cdots \;;$$

$$p = p_0(x,y) + p_2(x,y)\frac{z^2}{H^2} + \cdots \tag{14}$$

In the model we shall keep only the lowest-order terms in the expansions of velocity and magnetic field, that is, terms independent of z for symmetric quantities and terms proportional to z for antisymmetric quantities. From the boundary condition $v_z = 0$ at $z = \pm H_0$ it then follows that $v_{z1} = 0$, that is, that $v_z = 0$ throughout the boundary layer. We emphasize that, in contrast to the nonevolving model of *Phan et al.* [1989], the lowest-order terms do not form an exact solution in the present model. We can nevertheless evaluate all equations at $z = 0$; corresponding quantities are denoted by the subscript zero. It is then found that (5) and (8) are identically satisfied and that (1), (3), (4), (6), and (7) become

$$\frac{\partial}{\partial x}(\rho_0 v_{x0}) + \frac{\partial}{\partial y}(\rho_0 v_{y0}) = 0 \tag{15}$$

$$\rho_0\left(v_{x0}\frac{\partial}{\partial x} + v_{y0}\frac{\partial}{\partial y}\right)v_{x0} =$$

$$-\frac{dP_\infty(x)}{dx} + \frac{1}{\mu_0 H}B_{z0}B_{x1} + \frac{\partial}{\partial y}\left(\eta_0\frac{\partial v_{x0}}{\partial y}\right) \tag{16}$$

$$p_0 + \frac{B_{z0}^2}{2\mu_0} = P_\infty(x) \tag{17}$$

$$\left(v_{x0}\frac{\partial}{\partial x} + v_{y0}\frac{\partial}{\partial y}\right)\frac{p_0}{\rho_0^\gamma} = 0 \tag{18}$$

$$\frac{\partial(B_{z0}v_{x0})}{\partial x} + \frac{\partial(B_{z0}v_{y0})}{\partial y} = 0 \tag{19}$$

In (16), η_0 is the viscosity coefficient evaluated in the equatorial plane, and in (17) the quantity $P_\infty(x)$ is the sum of the plasma pressure and the magnetic pressure in the equatorial plane. This total pressure is independent of y and therefore has the same value in the boundary layer as in the magnetosphere, where it can be considered to be known for the purposes of our model. By use of (15), equation (19), which represents the z component of the induction law, can also be written in the form

$$\left(v_{x0}\frac{\partial}{\partial x} + v_{y0}\frac{\partial}{\partial y}\right)\frac{B_{z0}}{\rho_0} = 0 \tag{20}$$

The z and y components of the induction law are identically satisfied at $z = 0$. Finally, note from (18) and (20) that p_0/ρ_0^γ and B_{z0}/ρ_0 are constant along streamlines.

Equation (8) can be used to estimate the plasma pressure in the LLBL for $z \neq 0$, after the magnetic field is known. This equation implies that p has a negative quadratic term in z, in addition to the term $p_0(x,y)$, which describes the pressure in the equatorial plane. The variation in pressure described by this term is consistent with the

expectation that in the LLBL the plasma pressure should fall from a high value in the equatorial plane toward lower values at the high-latitude edge ($z = \pm H_0$) of the LLBL, although the magnetospheric pressure level is not actually reached in the present model due to the assumption of constant H_0. Extension of the model to include a variable boundary layer height so that the plasma pressure reaches its ambient magnetospheric level at $z = \pm H_0(x,y)$ is planned, as discussed further in section 5. It is also noted that (8) contains B_y; this field component, which is of the form $B_{y1}(z/H)$, can be calculated from B_{x1} by use of (5) and assuming $B_{x2}(x,y) = 0$.

In general, the density must be assumed to vary with z as well, falling toward a lower magnetospheric value at $z = \pm H_0$, which means that, in addition to the term $\rho_0(x,y)$, it has a negative quadratic term in z as well. In the present model, where all higher-order terms in the z expansions for velocity and magnetic field are neglected, the quadratic term in ρ can be obtained from the mass conservation law, which then takes the form $(v_{x0}\partial/\partial x + v_{y0}\partial/\partial y)(\rho_2/\rho_0) = 0$, together with the known upstream density distribution. Thus the lowest-order truncation of the z expansion of velocity and magnetic field allows us to calculate second-order terms in density and pressure by requiring mass conservation and exact force balance in the z direction to be maintained. If the expansions of **v** and **B** are carried to higher order, the lowest-order terms in these quantities and the terms describing density and pressure would all change. Therefore the z expansion used is not exact, in the sense that each term retained is not the same as the corresponding term in the expansion of the exact solution in a power series in z; rather it represents a polynomial approximation to the exact solution.

The system of (15), (16), (17), (18), and (20) contains six unknown quantities, namely v_{x0}, v_{y0}, B_{x1}, B_{z0}, ρ_0, and p_0. Thus we need one more equation to form a closed set. This equation will be provided by coupling to the ionosphere, as discussed in the following subsection; it will lead to an explicit expression for B_{x1} in the x momentum (equation (16)).

Ionospheric Closure

As mentioned already, in the present simplified model, the mapped, lumped properties of the ionosphere are represented by two parallel resistive plates at fixed height $z = \pm H_0$, that is, at the top and bottom of the LLBL. In the remainder of this paper we choose the characteristic scale height H in (12)-(14) to be the fixed boundary layer height H_0. The net current flowing on the surface of the plates at $z = \pm H_0$ may be expressed by

$$J_x = \Sigma E_x , \quad J_y = \Sigma E_y \tag{21}$$

where $J_{x,y}$ is the surface current density and Σ is an effective height-integrated conductivity representing the lumped response of the ionosphere and the low-pressure (low plasma beta) regions between $z = \pm H_0$ and the ionosphere. The components of the electric field, E_x and E_y, imposed on the plate by the boundary layer dynamo, are given by

$$E_x = E_x \mid_{z=\pm H_0} = -v_y B_z \mid_{z=\pm H_0} \sim (\delta/L)E_y$$

$$E_y = E_y \mid_{z=\pm H_0} = v_x B_z \mid_{z=\pm H_0} \tag{22}$$

An expression for the conductivity of the resistive plates that represent the ionosphere in our model was given by *Sonnerup* [1980]:

$$\Sigma \equiv H_0\sigma = \Sigma_P \frac{B_i}{B}\left(\frac{dx_i}{dx}\right)^2 \kappa$$

Here Σ_P is the height-integrated ionospheric Pedersen conductivity.

Also, B_i is the ionospheric magnetic field; B is a representative value of the magnetic field z component in the equatorial LLBL; dz_i/dz is the ratio of a length element dz_i in the ionosphere to a corresponding length element dz in the LLBL, and κ is a coupling factor which is unity when the magnetic field lines that connect the LLBL to the ionosphere are equipotentials. In its present form our model allows for field-aligned potential drops in the coupling region between the LLBL and the ionosphere only in the average sense obtained by letting the factor $\kappa < 1$. This restriction will be eliminated eventually, as explained in section 5. In principle, the effective conductivity Σ is a function of x and y, because the mapping factor dz_i/dz, as well as B and Σ_P vary in space.

We now impose current continuity at the top of the LLBL, that is, at $z = \pm H_0$, which leads to

$$ j_z \mid_{z=\pm H_0} = \frac{\partial J_z}{\partial x} + \frac{\partial J_y}{\partial y} \simeq \frac{\partial J_y}{\partial y} \qquad (23) $$

In this expression, J_z is smaller than J_y by a factor of the order of δ/L; thus $\partial J_z/\partial x$ is smaller than $\partial J_y/\partial y$ by a factor δ^2/L^2 and can be neglected. Using (11), (21), (22), and (23), we find

$$ B_z \mid_{z=\pm H_0} = \mp \mu_0 (\Sigma v_z B_z) \mid_{z=\pm H_0} + c(x) $$

where $c(x)$ is a constant of integration, and the negative and positive signs on the right side of the equation correspond to $z = +H_0$ or $z = -H_0$, respectively. In evaluating the left side of the above equation, B_{z3} and all higher terms in B_z will be ignored, as before, so that $B_z = B_{z1}(z/H_0)$. Similarly, we use only the lowest-order terms, v_{z0} and B_{z0}, in evaluating the right-hand side, the result being

$$ B_{z1} = -\mu_0 \Sigma v_{z0} B_{z0} + c(x) \qquad (24) $$

The function $c(x)$ is given by the boundary conditions at $y = \infty$ (for convenience, the interface between the LLBL and the magnetosphere is thought of as located at a large but finite y value: $y = y_\infty$): at that location v_{z0} assumes the low magnetospheric (sunward or antisunward) value $v_{z\infty}(x)$, the magnetic field B_{z0} becomes $B_\infty(x)$, B_{z1} becomes $B_{z1\infty}(x)$, the conductivity becomes Σ_∞, and the current j_y becomes $j_{y\infty}(x)$. That the latter quantity can be nonzero indicates that, as is the case in the geomagnetic tail, a net current may be flowing across the magnetic field, from the LLBL into the magnetosphere, or vice versa. Equations (10) and (24), both evaluated at $y = \infty$, can now be combined to eliminate $B_{z1\infty}$, the result being

$$ c(x) = \mu_0 \Sigma_\infty v_{z\infty} B_\infty + \mu_0 H_0 j_{y\infty} + H_0 \frac{\partial B_\infty}{\partial x} \qquad (25) $$

Substitution of (24) and (25) into (16) gives the following final form of the x component of the momentum conservation law in the equatorial plane ($z = 0$)

$$ \rho_0 \left(v_{z0} \frac{\partial}{\partial x} + v_{y0} \frac{\partial}{\partial y} \right) v_{z0} = $$

$$ -\frac{dP_\infty(x)}{dx} + \left(\sigma_\infty v_{z\infty} B_\infty + j_{y\infty} + \frac{1}{\mu_0} \frac{dB_\infty}{dx} \right) B_{z0} $$

$$ -\sigma B_{z0}^2 v_{z0} + \frac{\partial}{\partial y} \left(\eta_0 \frac{\partial v_{z0}}{\partial y} \right) . \qquad (26) $$

Note that σ, as defined in the equation following (22), can in principle depend on x and y, although $\sigma = \sigma_\infty = $ const is used in the calculations reported here. Note also that all magnetospheric quantities (denoted by subscript ∞) are functions of x, in general.

NUMERICAL PROCEDURE

Finite Difference Scheme and Boundary Conditions

For the solution of the five coupled equations (15), (17), (18), (20), and (26), of which four are partial differential equations with independent variables x and y, a Crank-Nicolson implicit finite difference scheme was implemented, similar to marching procedures that have been used in the past for fluid mechanical boundary layers [e.g., *Anderson et al.*, 1984]. The computational domain is a rectangular region in the xy plane. The lines $y = 0$ and $y = y_\infty$ represent the magnetopause and magnetospheric boundaries respectively. At those boundaries, appropriate boundary conditions are imposed, as described below.

At $y = 0$ the velocity $v_{z0}(x,0) \equiv V_0(x)$ is specified from an appropriate model of the magnetosheath flow (located in the region $y < 0$), assuming v_{z0} to be continuous across the magnetopause. The model in principle allows for a specified plasma flow normal to the magnetopause, but in the results reported here we have used the condition $v_{y0}(x,0) = 0$. This means that the cold plasma mass flux in the LLBL remains constant as one moves downstream from the computational boundary at $x = 0$ where velocity, magnetic field, and plasma properties are specified as functions of y, subject to certain consistency requirements to be explained presently. The restriction $v_{y0}(x,0) = 0$ also means that the upstream station cannot be located at local noon in the magnetosphere, unless a delta function mass source for the LLBL is assumed to be present there. In principle, the initial conditions at $x = 0$ could be chosen to match data from a satellite traversal of the LLBL; the evolution of the LLBL downstream from the satellite crossing could then be determined by the model.

At $y = y_\infty$ the x velocity v_{z0}, the magnetic field B_{z0}, the plasma density and pressure are fixed to their specified equatorial magnetospheric values, $v_{z\infty}(x)$, $B_\infty(x)$, $\rho_\infty(x)$ and $p_\infty(x)$, respectively, and are assumed to approach those values asymptotically so that $(\partial/\partial y)_{y=y_\infty} = 0$. For reasons of mass conservation the y component of the velocity $v_{y\infty}$ cannot be specified: it is determined from the numerical calculations and represents entrainment of magnetospheric plasma ($v_{y\infty} < 0$) or mass feeding of the magnetosphere from the LLBL ($v_{y\infty} > 0$). Finally, at the downstream boundary, located at $x = L$, say, no conditions are needed as a consequence of the parabolic nature of the problem.

The finite difference equations comprise a non-linear algebraic system of equations that involves all quantities to be calculated across n grid points in the y direction, at two consecutive steps in the $-x$ (main flow) direction. As mentioned already, initial conditions for various quantities are imposed. Note that $p_0(0,y)$ and $B_{z0}(0,y)$ must be chosen to obey (17). One can also show that the initial velocity profile $v_{y0}(0,y)$ cannot be chosen independently but is determined from the other variables. After $B_{z0}(0,y)$, $p_0(0,y)$, $\rho_0(0,y)$, and $v_{z0}(0,y)$ have been chosen, $v_{y0}(0,y)$ is obtained from the equation:

$$ v_{y0}(0,y) = v_{y0}(0,0) + v_{z0} \int_0^y \frac{dy}{\rho_0 v_{z0}^2} $$

$$ \left[\sigma B_{z0}^2 v_{z0} - \left(\sigma_\infty v_{z\infty} B_\infty + j_{y\infty} + \frac{1}{\mu_0} \frac{dB_\infty}{dx} \right) B_{z0} \right. $$

$$ \left. + \frac{dP_\infty}{dx} \left(1 - \frac{\rho_0 v_{z0}^2}{\gamma p_0 + \frac{B_{z0}^2}{\mu_0}} \right) - \frac{\partial}{\partial y} \left(\eta_0 \frac{\partial v_{z0}}{\partial y} \right) \right] \qquad (27) $$

Equation (27) is derived as follows: The term $\partial v_{z0}/\partial x$ on the left in the x momentum equation (equation (26)) can be substituted

17

from the mass conservation law (equation (15)). The term $\partial \rho_0 / \partial x$ will then appear, but the system of (17), (18) and (20) can be solved for $\partial \rho_0 / \partial x$ as well as $\partial B_{z0} / \partial x$ and $\partial p_0 / \partial x$. By further substitution of $\partial \rho_0 / \partial x$ into (26), only derivatives with respect to y will appear. Equation (27) follows by first forming the derivative $(d/dy)(v_{y0}/v_{x0})$ and then integrating. It is evident that (27) is true, not just for $x = 0$, but for any value of x.

After the problem is initiated at $x = 0$ the solution is found simultaneously at all grid points across the boundary layer at the next step in the main flow direction ($-x$), by solving the nonlinear algebraic system mentioned above; this solution is then used to march forward. The system is solved by Newton's method [*Burden and Faires*, 1989], which is a fixed point (iterative) procedure requiring an initial guess close to the actual solution. Since the variations of the boundary layer in the x direction are slow, this guess is provided by the values at the previous step in x.

Asymptotic Region

It is one of the goals of the model and the numerical scheme to be able to predict not only the antisunward LLBL flow but also variations of slow sunward flow observed on the earthward side of the LLBL. It should be noted here that, partly for instrumental reasons, some ambiguity exists in the data regarding the latter region: *Sckopke et al.* [1981] report a halo region adjacent to and earthward of the LLBL, where the density and temperature are intermediate between those in the LLBL and in the magnetosphere and where the velocities are, for the most part, small and have variable direction. However, sometimes they find time intervals in which the flow is clearly antiparallel to the magnetosheath flow. *Williams et al.* [1985] report a stagnation region adjacent to the main antisunward LLBL flow region, where velocities are small and have variable direction, and a region of small but steady sunward flow earthward of it. It is not clear whether the intermediate region contains actual turbulent flow or whether it is simply a region of gradual transition in which the small velocities are not well-resolved. As described in detail below, our model contains an asymptotic flow region earthward of the boundary layer proper which includes a flow reversal followed by monotonically increasing and then constant sunward flow as one moves from the boundary layer proper into the magnetosphere. Inclusion of field-aligned potential drops in the coupling region between the LLBL and the ionosphere is expected to change this asymptotic velocity profile into one that includes an overshoot in the sunward flow adjacent to the velocity reversal [*Lotko et al.*, 1987].

An integration procedure that marches forward in the antisunward direction fails within a few steps in a reverse flow region, a difficulty that can be traced to the term $v_{x0} \partial v_{x0} / \partial x$ in the x momentum equation. This term retains its sign, while all other terms in the equation containing v_{x0} reverse their signs, when v_{x0} reverses sign. In the reverse-flow region the correct marching direction is therefore reversed. This problem has long been recognized in computational fluid dynamics and different solutions have been proposed. Noticing that the reverse flow is usually slow, *Reyhner and Flügge-Lotz* [1968] suggested neglecting the term $v_{x0} \partial v_{x0} / \partial x$ or reversing its sign. On the basis of that idea we have proceeded to neglect the above term in the x momentum equation in the reverse flow region as well as in a narrow region on the magnetopause side of the flow reversal point, where v_{x0} is negative but sufficiently small so that $v_{x0} \partial v_{x0} / \partial x$ can be justifiably neglected. The reason for including the latter region is that there is also a second difficulty at the flow reversal: when the reversal point falls close to a grid point, a numerical singularity appears. We emphasize that the above

approximation is consistent with slow-flow convection models of the inner magnetosphere (e.g., the Rice convection model) to which the LLBL model should eventually be matched.

To implement these approximations, we have terminated our regular computational box at $y = y_b$ but appended to its magnetospheric side what we call an asymptotic box, $y_\infty \geq y \geq y_b$, in which the inertia term $\rho_0 v_{x0} \partial v_{x0} / \partial x$ is neglected. The location $y = y_b$ is different in every step of the calculation along the $-x$ direction: in the runs presented here it is defined by the requirement that v_{x0} at that location be 9 km/s or less, in the antisunward direction. Furthermore, in the asymptotic box we take ρ_0, p_0, and B_{z0} to be independent of y so that $\rho_0 = \rho_\infty(x)$, $p_0 = p_\infty(x)$, and $B_{z0} = B_\infty(x)$ there. With the above assumptions the resulting x momentum equation becomes

$$\rho_0 v_{y0} \frac{\partial v_{x0}}{\partial y} = -\sigma_\infty (v_{x0} - v_{x\infty}) B_\infty^2 + \eta_\infty \frac{\partial^2 v_{x0}}{\partial y^2} \quad . \quad (28)$$

Equation (28) follows from (26) by setting $v_{x0} \partial v_{x0} / \partial x$ equal to zero and by noticing that the third term inside the parenthesis of the right-hand side of (26) cancels the magnetic pressure part of the term $-dP_\infty(x)/dx$. The plasma pressure part of that term is canceled by $j_{y\infty} B_\infty$ if one requires the solution for v_{x0} to be independent of y as $y \rightarrow \infty$. Also, the viscosity η_0 in the asymptotic box is taken to be $\eta_\infty(x)$, because it is assumed that η_0 depends in a general way upon ρ_0, p_0, and B_{z0}, all of which have become independent of y in that box. If the y variation of v_{y0} is neglected in the asymptotic box, equation (28) has a simple analytic solution, namely

$$v_{x0} = v_{x\infty}(x) + [v_{x0}(x, y_b) - v_{x\infty}(x)]e^{-a(x)(y - y_b)} \quad (29)$$

where

$$a(x) = \frac{-\rho_0 v_{y0}(x, y_b) + \sqrt{\rho_0^2 v_{y0}^2(x, y_b) + 4\eta_\infty \sigma_\infty B_\infty^2}}{2\eta_\infty} \quad (30)$$

In reality, v_{y0} is a function of y in the asymptotic box; the above solution is therefore only an approximation to the actual solution. In the runs presented in this paper, the above solution is close to the exact solution when v_{y0} has a slow variation with y as it usually does away from the upstream location. The exact solution can be found by integrating equation (28); one may assume that v_{y0} is approximately known from the previous step, so that (28) becomes an ordinary differential equation for v_{x0}.

At the boundary between the asymptotic box and the computational box, $y = y_b$, we require that v_{x0} and v_{y0} be continuous and that

$$a(x)v_{x0}(x, y_b) + \frac{\partial v_{x0}(x, y)}{\partial y}\bigg|_{y = y_b} = a(x)v_{x\infty}(x) \quad (31)$$

which guarantees that $\partial v_{x0} / \partial y$ and $\partial v_{y0} / \partial y$ will also be continuous at $y = y_b$. Equation (31) is obtained from (29) by differentiation. As can be seen from (29) and (31), only v_{x0} and its first derivative can be made continuous at $y = y_b$. A small discontinuity in the second derivative of v_{x0} remains and leads to a corresponding discontinuity in the first derivative of the current j_x. In the results presented in this paper we have therefore allowed the exponent $a(x)$ to differ slightly from the value given by (30), in such a way that the second derivative of v_{x0} is also continuous at $y = y_b$. By differentiating (29) twice, the following condition is found at that boundary:

$$a^2(x)v_{x0}(x, y_b) + \frac{\partial^2 v_{x0}(x, y)}{\partial y^2}\bigg|_{y = y_b} = a^2(x)v_{x\infty}(x) \quad (32)$$

Eliminating $a(x)$ between (31) and (32) yields the following modi-

fied boundary condition at the interface between the computational box and the asymptotic box:

$$\frac{\partial^2 v_{x0}(x,y)}{\partial y^2}\Big|_{y=y_b} = -\frac{\left(\frac{\partial v_x(x,y)}{\partial y}\Big|_{y=y_b}\right)^2}{v_{x0}(x,y_b) - v_{x\infty}(x)} \qquad (33)$$

We can finally obtain v_{y0} in the asymptotic box by integration of the mass conservation law:

$$v_{y0}(x,y) = v_{y0}(x,y_b) - (y - y_b)\frac{1}{\rho_\infty(x)}\frac{d(\rho_\infty v_{x\infty})}{dx} +$$

$$\frac{1}{\rho_\infty(x)}\frac{d}{dx}$$

$$[\frac{\rho_\infty(x)}{a(x)}(v_{x0}(x,y_b) - v_{x\infty}(x))(e^{-a(x)(y-y_b)} - 1)] \qquad (34)$$

Note from (34) that, in general, $v_{y\infty}$ does not reach a constant value but retains a linear variation with y as $y \to \infty$.

Since the nature of the solution in the asymptotic box is such that v_{x0} decays at a relatively slow exponential rate to $v_\infty(x)$, the reduction of the size of the computational box that results from use of an asymptotic box saves a great deal of computer time.

Normalization

We now explain the normalization of all variables in (15), (17), (18), (20), and (26), which leads to an important result regarding the role of viscosity in our simplified model. The normalized variables, denoted by an asterisk, are

$$x^* = x/H_0, \quad y^* = y\sqrt{Re}/H_0,$$

$$v_x^* = v_{x0}/V_n, \quad v_y^* = v_{y0}\sqrt{Re}/V_n, \quad B_x^* = \frac{B_{x0}}{V_n\sqrt{\mu_0\rho_n}}$$

$$\rho^* = \rho_0/\rho_n, \quad p^* = \frac{p_0}{\rho_n V_n^2}, \quad P_\infty^* = \frac{P_\infty}{\rho_n V_n^2},$$

$$j_{y\infty}^* = \frac{j_{y\infty}H_0}{V_n}\sqrt{\frac{\mu_0}{\rho_n}} \qquad (35)$$

In the above, H_0 is the characteristic height of the LLBL while V_n and ρ_n are reference values of the flow velocity and density. Also, Re is the viscous Reynolds number, $Re = \rho_n V_n H/\eta_n$, η_n being a reference value for the viscosity, and Rm is the magnetic Reynolds number, defined by $Rm = \mu_0\sigma_\infty V_n H_0$.

The dimensionless system of (15), (17), (18), (20), and (26) now becomes (the asterisks are dropped for convenience):

$$\frac{\partial}{\partial x}(\rho v_x) + \frac{\partial}{\partial y}(\rho v_y) = 0 \qquad (36)$$

$$p + \frac{B_x^2}{2} = P_\infty(x) \qquad (37)$$

$$(v_x\frac{\partial}{\partial x} + v_y\frac{\partial}{\partial y})\frac{p}{\rho^\gamma} = 0 \qquad (38)$$

$$(v_x\frac{\partial}{\partial x} + v_y\frac{\partial}{\partial y})\frac{B_x}{\rho} = 0 \qquad (39)$$

$$\rho(v_x\frac{\partial}{\partial x} + v_y\frac{\partial}{\partial y})v_x =$$

$$-\frac{dP_\infty(x)}{dx} + (Rmv_{x\infty}B_\infty + j_{y\infty} + \frac{dB_\infty}{dx})B_x$$

$$- RmB_x^2 v_x + \frac{\partial}{\partial y}(\frac{p^{p_1}\rho^{p_2}}{B_x^{p_3}}\frac{\partial v_x}{\partial y}) . \qquad (40)$$

The viscous Reynolds number has been scaled out of the equations because of our particular normalization of y and v_y. This implies that the reference value of the viscosity affects our system only as a scaling factor for the width of the LLBL and the magnitude of v_y. In other words, a thin LLBL with low viscosity evolves in the same way as a proportionately thicker layer with higher viscosity. However, for one and the same upstream width, boundary layers with different viscosity evolve differently. Note also that we have chosen viscosity to depend parametrically on pressure, density and magnetic field, as indicated by the factor $(p^{p_1}\rho^{p_2}/B_x^{p_3})$ in the last term of (40). For example, the collisional viscosity transverse to a strong magnetic field has $p_1 = -0.5$, $p_2 = 2.5$, $p_3 = 2$ [*Spitzer*, 1962]; for Bohm diffusion one finds $p_1 = 1$, $p_2 = 0$, $p_3 = 1$. The reason for using a nonconstant viscosity is that, as discussed later on, uniform viscosity throughout the LLBL is found to result in excessive entrainment of magnetospheric plasma and high acceleration of this plasma downstream. To avoid this effect, viscosity must decrease with increasing distance from the magnetopause: this is accomplished, for example, for positive values of p_1, p_2, and p_3.

APPLICATIONS

We now present three examples of LLBL flow obtained from the numerical code. We first describe the boundary conditions and initial conditions used in the three runs; in the remainder of the section we discuss the results obtained.

All three runs were initiated at $x = 0$. The initial $v_x(y)$ velocity profile is a somewhat arbitrarily chosen, smooth function of y, with continuous first and second derivatives. This profile satisfies (31) at the interface between the computational box and the asymptotic box; in the latter, it includes a region of reverse flow as $y \to y_\infty$ and v_x becomes independent of y in that limit. With known initial profile $v_x(y)$ the initial v_y is given by (27). We assumed an initial number density decrease of 80% across the LLBL, from 10 protons/cm³ at the magnetopause to 2 protons/cm³ in the magnetosphere, a corresponding increase of 10% in the x component of the magnetic field, from 40 to 44 nT, and a constant total pressure of 1 nPa across the layer. The initial plasma pressure can then be calculated from (17), the result being that the temperature, $T_0(y) = p_0(y)/R\rho_0(y)$, where $R = k/m_p$ is the gas constant, varies from 230 eV at the magnetopause to 775 eV in the magnetosphere. The parameters chosen for these runs are representative of typically observed boundary layer crossings [*Sckopke et al.*, 1981; *Eastman and Hones*, 1979]. They result in an average electric field component across the layer of a few mV/m, as measured directly by *Mozer* [1984] and as inferred by *Mitchell et al.* [1987], *Williams et al.* [1985], and others on the basis of particle measurements. Note that the magnetic field decrease together with the flow acceleration lead to an approximately constant value of this electric field as one moves downstream in the layer.

The values of the characteristic density ($\rho_n = 10\ m_p$ kg/cm³) and viscosity η_n are such that the kinematic viscosity at $x = y =$

0 is $\nu_n \equiv \eta_n/\rho_n = 10^9$ m^2/s [Sonnerup, 1980; LaBelle and Treumann, 1988] in the first two runs, while in the third run viscosity has been reduced by a factor of 3. Also, $p_{1,2,3} = 0$ in the first run and $p_1 = 0, p_{2,3} = 1$ in the second and third run. The velocity V_n used for normalization is taken to be 280 km/s and $H_0 = 10$ R_E. All calculations are performed with the ratio of specific heats, $\gamma = 2$. The viscous Reynolds number Re used in the first two runs is 1.8×10^4, based on the half height of the LLBL, H_0, and on the value of the dynamic viscosity at $z = 0$, $y = 0$. Note that the Reynolds number based on the width of the layer is at least 20 times smaller. The magnetic Reynolds number Rm, based on the effective conductivity σ_∞ which embodies the effects of coupling to the ionosphere, is 0.1; this choice leads to realistic values for the field-aligned currents at the top of the ionosphere, of the order of 5×10^{-6} A/m^2. To achieve that, the value of the effective conductivity σ_∞ is reduced by a factor of 10 from the value 5.96×10^{-8} mho/m given by Sonnerup [1980] for orange-segment mapping and perfect coupling to the ionosphere.

The boundary conditions are as follows:

1. At the magnetospheric boundary, that is, at $y = y_\infty$, v_x is constant, $v_{x\infty} = +10$ km/s in the sunward direction, while the magnetic field falls exponentially in the downstream $(-x)$ direction, according to the formula $B_z = B_\infty(x) = 44\exp(0.03x/R_E)$ nT. This simple functional form is not necessarily an accurate representation of the actual field variation in the magnetosphere, but it qualitatively models the variation of B_∞ with downstream distance. For given x the density, plasma pressure, and total pressure are constant across the asymptotic box and are the same as in the magnetosphere. They can be calculated from the following three conditions:

$$\frac{B_\infty(x)}{\rho_\infty(x)} = \frac{B_\infty(0)}{\rho_\infty(0)}$$

$$\frac{p_\infty(x)}{\rho_\infty^\gamma(x)} = \frac{p_\infty(0)}{\rho_\infty^\gamma(0)}$$

$$p_\infty(x) + \frac{B_\infty^2(x)}{2\mu_0} = P_\infty(x) \qquad (41)$$

These relations follow from the induction law and the isentropic law, applied along the dividing streamline passing through the point $y = y_b$ at $x = 0$, and from the y component of the momentum equation. If there is inflow into the computational box, across $y = y_b$, this streamline is located in that box; therefore the values calculated from (41) can be used as boundary conditions at $y = y_b$. If there is outflow from the computational box across $y = y_b$, the dividing streamline is located in the asymptotic box; in that case the values from (41) can be used as boundary conditions at $y = y_b$ only if plasma leaving the computational box also carries with it those uniform values of B, ρ and p. In other words, a region of uniform values must always be present in the computational box itself, immediately adjacent to $y = y_b$. As $y \rightarrow y_\infty$, we require a balance between the pressure force $-\partial p_\infty/\partial x$ and the force $j_{y\infty}B_\infty$ from which the current $j_{y\infty}(x)$ that flows from the LLBL into the magnetosphere can be calculated; in the simulations presented here $j_{y\infty} \neq 0$.

2. At the magnetopause, that is, at $y = 0$, the plasma is assumed to accelerate in the antisunward direction from 50 km/s, at $x = 0$, to 290 km/s at $x = -15$ R_E, approximately, 150 km/s being gained within the first 5 R_E, as described by the formula $v_x(x,0) = -[308 - 258\exp(x/5.75R_E)]$ km/s. Again, this formula is only a qualitative representation of the actual variation of $v_x(x,0)$ in the magnetosphere. Since we do not allow flow across

the magnetopause, that is, since $v_y(x,0) = 0$, the line $y = 0$ is a streamline. Thus, B_x, ρ, and p at $y = 0$ are defined by relations similar to (41).

Figure 2 shows results of the first simulation example. The bottom row of the figure consists of three plots representing, in order from left to right, density, temperature and z component of the magnetic field, all in the equatorial plane, as functions of y at three different locations along the magnetopause, namely, at $x = -0.25$ R_E, -7.5 R_E and -15 R_E. The pressure profile is not shown but can be calculated from ρ_0 and T_0; it has the property that $p_0 + B_{z0}^2/2\mu_0$ is constant across the layer. The x and y components of the flow velocity and the z component of the current at the top of the LLBL are plotted in the middle row as functions of y at the same locations downstream. The values of the current density in Figure 2, multiplied by B_i/B_{z0}, give the actual field-aligned currents at the top of the ionosphere; here $B_i = 5 \times 10^4$ nT is the ionospheric magnetic field. The top panels consist of two vector plots followed by one contour plot representing the z component of the current. The first vector plot represents the actual velocity vectors; in the second plot, v_y was magnified by a factor of 27 in order to make visible the inflow from the magnetospheric boundary. The horizontal axis in all three top panels corresponds to the y direction (across the LLBL), whereas the vertical axis is the distance downstream (the $-x$ direction). The width of all panels is 0.85 R_E, $y = 0$ at the left being the magnetopause boundary.

The dynamic viscosity in this first example is taken to be constant (i.e., $p_{1,2,3} = 0$ in (40)) throughout the LLBL and to be such that the kinematic viscosity at the magnetopause and at $x = 0$ is equal to the reference value, 10^9 m^2/s. The v_x profiles in Figure 2 indicate that the velocity boundary layer is becoming thicker and that its earthward portions accelerate downstream, as plasma enters from the magnetospheric boundary to become entrained in the boundary layer flow. This plasma moves into the LLBL carrying with it a higher magnetic field and lower density. Thus, while the velocity layer increases in width, the magnetic field, the temperature and density layers all decrease their widths, as shown in the bottom plots in Figure 2. Notice also the decrease in density and temperature levels with increasing x, behavior that is in agreement with (41) and with our choice of the x dependence of the magnetic field in the magnetosphere.

The plots of current density require special comment. The z component of the current at the top of the LLBL is

$$j_z|_{z=H_0} = -\frac{1}{\mu_0}\frac{\partial B_{z1}}{\partial y} = \Sigma(B_{x0}\frac{\partial v_{x0}}{\partial y} + v_{x0}\frac{\partial B_{x0}}{\partial y}) \qquad (42)$$

The contour plot as well as the current profile show that the current evolves in a complicated manner creating a secondary maximum at some distance away from the magnetopause: the two terms on the right in (42) have opposite signs and compete in a way that results in an intervening local minimum. As seen in Figure 2, this effect can even create a current reversal; this occurs when a relatively large negative v_y makes the magnetic field profile become very steep, thus increasing the magnitude of the negative term $v_{x0} \partial B_{x0}/\partial y$ in (42). We draw attention to this point because the observational data often show a highly structured behavior of the region 1 currents as a function of latitude. However, field-aligned potential drops $\Delta\Phi_{||}$ in the coupling region between the LLBL and the ionosphere, which were included by Lotko et al. [1987] and Phan et al. [1989], are expected to modify the current profile significantly. When $\Delta\Phi_{||} = 0$, the value of the current, j_z, at the magnetopause is specified by the conductivity Σ and by the magnetic-field and velocity profiles, as can be seen from (42): in the runs described here the conductivity has been adjusted, as discussed by Sonnerup [1980], to produce realistic values for the average field-aligned currents at the iono-
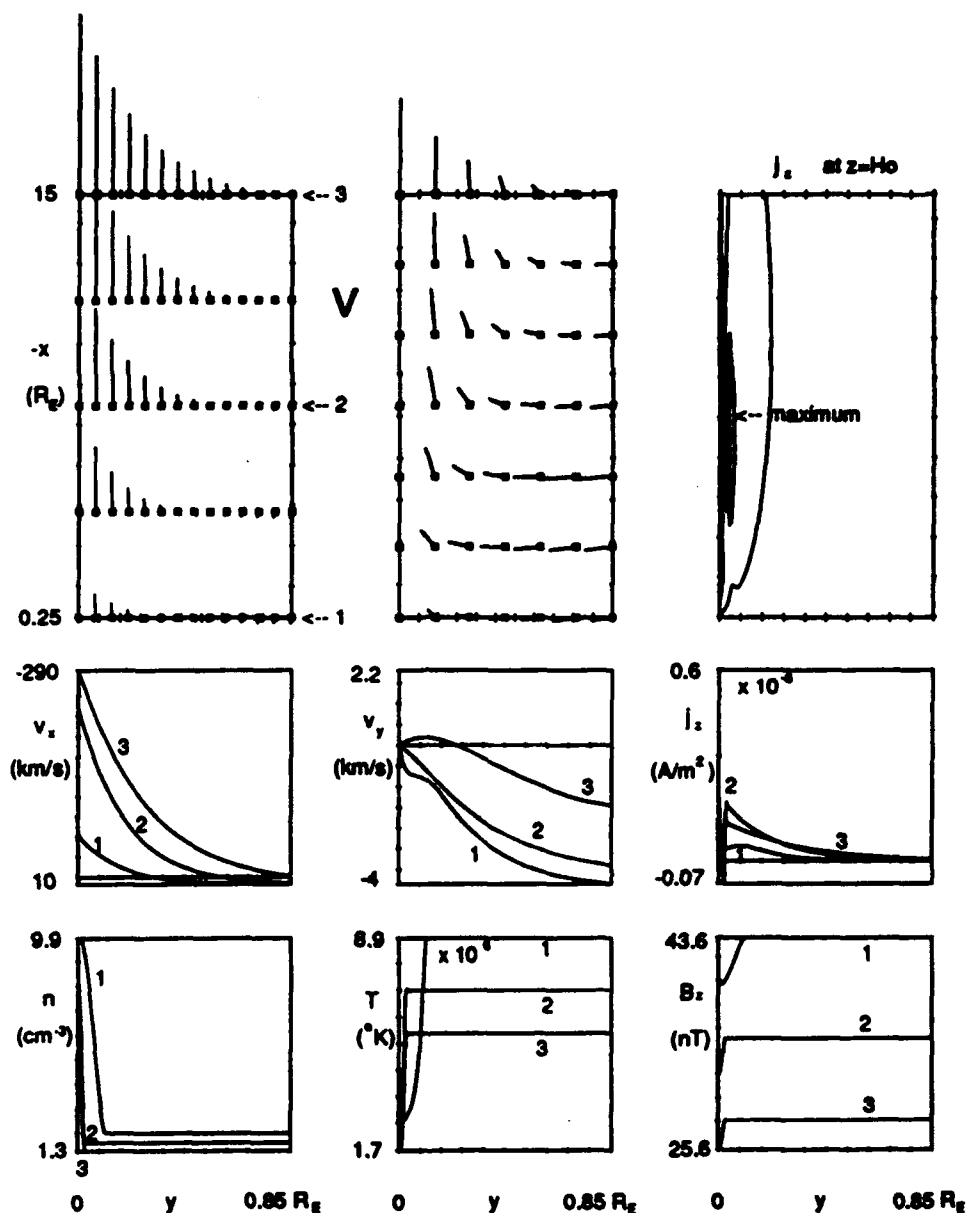
20

Fig. 2. Results from run 1: constant dynamic viscosity. Top panels show two velocity vector plots and a contour plot of the current density j_z at $z = H_0$. Magnitude of v_y has been magnified by a factor 27 in the second vector plot to show the entrainment of magnetospheric plasma into the layer. Remaining panels show profile plots of various quantities across the layer at $z = -0.25 R_E$, $-7.5 R_E$ and $-15 R_E$ (marked by 1, 2 and 3, respectively). The computational box ends at $y = 0.18 R_E$, $0.47 R_E$, and $0.72 R_E$ at the locations 1, 2 and 3, respectively. The $v_x(y)$ profiles indicate large viscous entrainment of magnetospheric plasma and a rapidly widening velocity layer. The current density profiles, j_z, at $z = H_0$ are double peaked with an intervening current reversal; j_z has an absolute maximum at a certain z value (near $z = -7 R_E$), that is, at a certain local time. The corresponding ionospheric currents are given by the currents presented here, multiplied by a factor $B_i/B_{BL} = 1667$. The thickness of the density, temperature, and magnetic field boundary layers decrease as the plasma moves downstream, even though the thickness of the velocity layer increases.

sphere [Iijima and Potemra, 1976a]. On the other hand, when $\Delta\Phi_{||} \neq 0$ the resulting fourth order differential equation describing the LLBL [Lotko et al., 1987] allows one to specify $j_z = 0$ at the magnetopause in which case the maximum in region 1 current by necessity appears at some distance away from that surface.

The longitudinal variation of j_z shown in Figure 2 is a consequence of the variation of the flow parameters in the $-z$ direction, which, unlike the previous models of Lotko et al. [1987] and Phan et al. [1989], continuously modifies the two terms in (42). An observed feature [Iijima and Potemra, 1976a] that is predicted by our model is that the peak intensity in the region 1 current density

first increases in magnitude with increasing flow distance, reaching a maximum value at some distance $|z|$ downstream, and then reduces. In our model, two effects compete to produce this result. First, the flow accelerates downstream, thus increasing the velocity shear, $\partial v_{x0}/\partial y$, which increases the magnitude of the first term in (42). Second, the velocity layer increases in thickness downstream as a result of viscosity, thus decreasing the shear, and consequently the magnitude of the current. Initially, the first effect dominates and the current peak increases in magnitude as one moves downstream, but later on the second effect takes over and causes the maximum current to decrease again.

21

In the example presented above, substantial entrainment of magnetospheric plasma into the LLBL occurs. As shown in Figure 2, the velocity layer becomes thick compared to the density layer and its earthward portions accelerate rapidly, owing to the assumption that viscosity remains high also in the magnetospheric plasma. Observations by *Sckopke et al.* [1981] and *Eastman et al.* [1979] do not show such behavior: during passage from the magnetosphere into the LLBL proper the velocity increase precedes the density increase by only a small distance so that only a small amount of hot magnetospheric plasma is entrained by the tailward flow in the LLBL. Although inclusion of field-aligned potential drops in the coupling region can be expected to modify the velocity profile predicted by the model in a significant way [*Lotko et al.*, 1987], it seems plausible that this observed weak entrainment of magnetospheric plasma

is accomplished naturally because the viscosity varies across the layer. In the next simulation example the viscosity is assumed to drop across the layer in proportion to the drop in density and in inverse proportion to the increase in magnetic field, as one moves into the magnetospheric plasma. In other words, $p_1 = 0$, $p_2 = 1$, and $p_3 = 1$ in (40).

Figure 3 represents our second example. The panel arrangement here is the same as in Figure 2. Except for the viscosity model, all parameters, and the initial and boundary conditions are the same as in the first example. The v_x profiles now indicate a curvature reversal at the approximate location of maximum slope of the density and magnetic field profiles, a result of the variable viscosity, that is, of the fact that viscosity drops rapidly as one leaves the dense boundary layer plasma and enters the tenuous magneto-
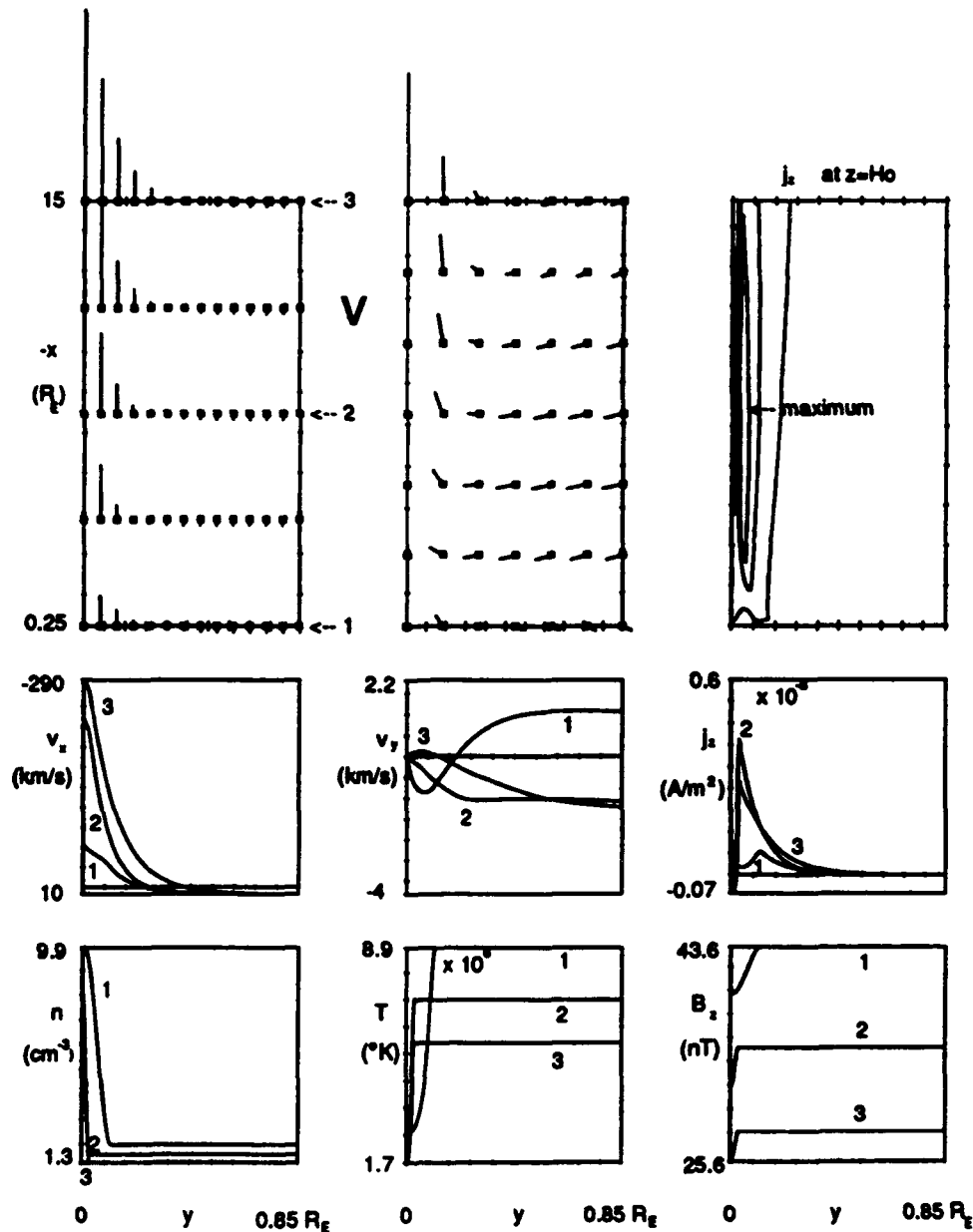

Fig. 3. Results from run 2: dynamic viscosity proportional to ρ/B_z. Format is the same as in Figure 2. The computational box ends at $y = 0.18\ R_E$, $0.22\ R_E$, and $0.33\ R_E$ at the locations 1, 2, and 3, respectively. The velocity boundary layer is now much thinner. Notice also the curvature reversal, near the magnetopause, of the profiles of $v_x(y)$ at the location of maximum slope of the profiles of $\rho(y)$ and $B_z(y)$. The $v_y(y)$ profiles show evidence of the partial relaxation of the system from its initial conditions. The secondary current density maximum is now higher than the one at the magnetopause and current densities are higher overall.

spheric plasma. The field-aligned current again develops a reversal region followed by a secondary maximum at some distance away from the magnetopause, which is now higher than the value at the magnetopause.

The first v_y profile, at $z = -0.25\ R_E$, differs in shape from v_y profiles further downstream. This behavior is caused by a rapid relaxation from the arbitrary initial velocity profile $v_x(0, y)$: within a short distance downstream the flow settles down to a more regular, slow evolution determined mainly by the boundary conditions. As an illustration of the fading memory of the system with respect to the initial velocity distribution, we refer to the analytic solution given by Sonnerup [1980]. With constant values of V_0, B_{x0}, and σ, and with $dP_\infty/dx = 0$, $v_{x\infty} = 0$ and $j_{y\infty} = 0$, (26) has the asymptotic solution

$$v_{x0} = -V_0 e^{-y/\delta_\nu}, \quad v_{y0} = 0 \qquad (43)$$

as $z \to -\infty$, where δ_ν is the viscous length, used by Atkinson [1967], Sonnerup [1980], and others:

$$\delta_\nu = \left(\frac{\eta_\infty}{\sigma_\infty B_\infty^2}\right)^{1/2} \qquad (44)$$

This solution also satisfies (15), (17), (18), and (20) identically. The density profile can be arbitrary in this solution. Any chosen initial $v_x(0, y)$ profile and its associated $v_y(0, y)$ profile evolves in such a way that, after some relaxation distance along the main flow direction, $v_x(z, y)$ becomes identical to (43) and $v_y(z, y) \equiv 0$. In this case the system loses memory of the initial velocity state completely, the final state being determined entirely by the boundary conditions. However, information about the initial density profile remains. In the general case, memory of nonconstant initial magnetic field, density, and temperature profiles is retained and a state that is independent of z is never reached, unless the boundary conditions at $y = 0$ and $y = y_\infty$ become independent of z.

In the first example the relatively higher viscosity at the location of the secondary maximum, reduces the velocity shear, thereby spreading the velocity boundary layer and decreasing the magnitude of the first term in (42). The result is relatively lower magnitudes of the current at that location and overall. In the second example the velocity boundary layer is narrower, and the shear is larger at the location of the secondary maximum, as a result of lower viscosity in the magnetosphere. The secondary current maximum is larger and lower $|v_y|$ values are generated, that is, less magnetospheric plasma is being entrained into the layer. The total potential difference across the LLBL, between the magnetopause and the location where the velocity reverses sign in this run, is 1.65 kV initially, 4.4 kV at a distance 7.5 R_E downstream, and 5.65 kV at a distance 15 R_E downstream. These values of the potential drop across the LLBL are consistent with typically measured potential drops [Mozer, 1984].

In our last simulation, shown in Figure 4, we reduce the reference viscosity by a factor of 3, from $\nu_n = 10^9$ to $\nu_n = 3.3 \times 10^8\ m^2/s$ but maintain its dependence on ρ and B ($p_{1,3} = 1$, $p_2 = 0$). As a result, the viscous Reynolds number increases by a factor of 3. We initiate this case with the same upstream conditions as in example 2 and use the same boundary conditions as well. At the downstream locations, $z = -7.5\ R_E$ and $z = -15\ R_E$, the velocity boundary layer is now thinner than in the previous two runs. There is a relatively large initial outflow of plasma ($v_y > 0$) across the magnetospheric boundary during which the initial excessive amount of plasma participating in the downstream motion leaves the layer. As a result of lower viscosity close to the magnetopause, no reversal of field-aligned current occurs.

In Figure 5 we plot magnetic field lines from run 2 at $z = -7.5\ R_E$ in three zz planes, namely, at the magnetopause plane,

$y = 0$, and two planes parallel to it, located at $y = 700$ km and $y = 4700$ km, respectively. The view is from outside the dawnside LLBL, looking towards the magnetosphere and with the Sun on the right. Figure 5 shows that the field lines are bent into approximate parabolas; their curvature is greatest near the magnetopause and is least at the magnetospheric boundary; some curvature remains at $y = 4700$ km because $j_{y\infty} \neq 0$; as a result of the increasing flow speed and decreasing magnetic field the curvature increases as one moves downstream. Notice that the scale in the z direction has been exaggerated: at $z = 10\ R_E$ the lines are in reality displaced $\sim 1.5\ R_E$ sunward of their intersection point with the equatorial plane. We believe that in the real LLBL such a field configuration may reduce or eliminate turbulence in the layer, because magnetic flux tubes of different curvature do not easily interchange their locations. The magnetic field configuration described above and its stabilizing effect were also noted by Southwood [1979].

DISCUSSION

In this paper we have presented initial results of a steady state numerical model of the low-latitude boundary layer on closed field lines. The model is experimental: our purpose is to see if it can predict certain features, such as spatial distribution of field-aligned currents flowing into the ionosphere, that are observed in the data and to examine the effect of different parameters in the model such as the viscosity formula, viscous and magnetic Reynolds numbers, upstream conditions and boundary conditions at the magnetopause and in the magnetosphere. In contrast to the models by Phan et al. [1989], Lotko et al. [1987], and Sonnerup [1980] the present model includes variation of boundary layer properties such as flow velocity, magnetic field, plasma pressure, and density as one moves in the downstream ($-z$) direction, thus allowing for evolution of the LLBL in the flow direction. The variation of all quantities with distance (z) away from the equatorial plane is parameterized in a simple way. The flow evolution in the z direction is governed by a balance between inertia forces, $j \times B$ forces, pressure forces, and viscous forces, whereas in the two perpendicular directions (y and z) the boundary layer approximation results in static balance of forces. The currents in the LLBL are calculated in a self-consistent manner, via Ampère's law. As a result, the magnetic field components B_x and B_z are allowed to be of comparable magnitude, the field lines being approximately parabolic, with vertices pointing in the antisunward direction and with maximum curvature for field lines adjacent to the magnetopause. At the magnetospheric edge of the layer the curvature is smaller but need not be zero as a consequence of allowing a finite cross-field current $j_{y\infty}(z)$ to flow from the boundary layer into the magnetosphere. We distinguish here between the Phan et al. [1989] model, where the magnetic field lines are exact parabolas, and the present model where, owing to the (slow) z variation, they are only approximate parabolas.

We emphasize the following results obtained from the present version of the model: (1) The velocity boundary layer increases in thickness downstream as a result of viscous entrainment leading to inflow into the boundary layer region of low density magnetospheric plasma carrying higher magnetic field. This inflow leads to thinning and steepening of the density, temperature and magnetic field profiles. (2) The velocity profile tends to relax from an arbitrarily assumed upstream shape to shapes that are mainly governed by the boundary conditions. However, the LLBL never loses memory of the initial magnetic field, density and pressure profiles. (3) The thickness of the velocity profile is greatly influenced by viscosity which enters the system as a scaling factor (see equation (35)), larger viscosity resulting in thicker velocity profiles. (4) The field-aligned currents that flow into the ionosphere from the
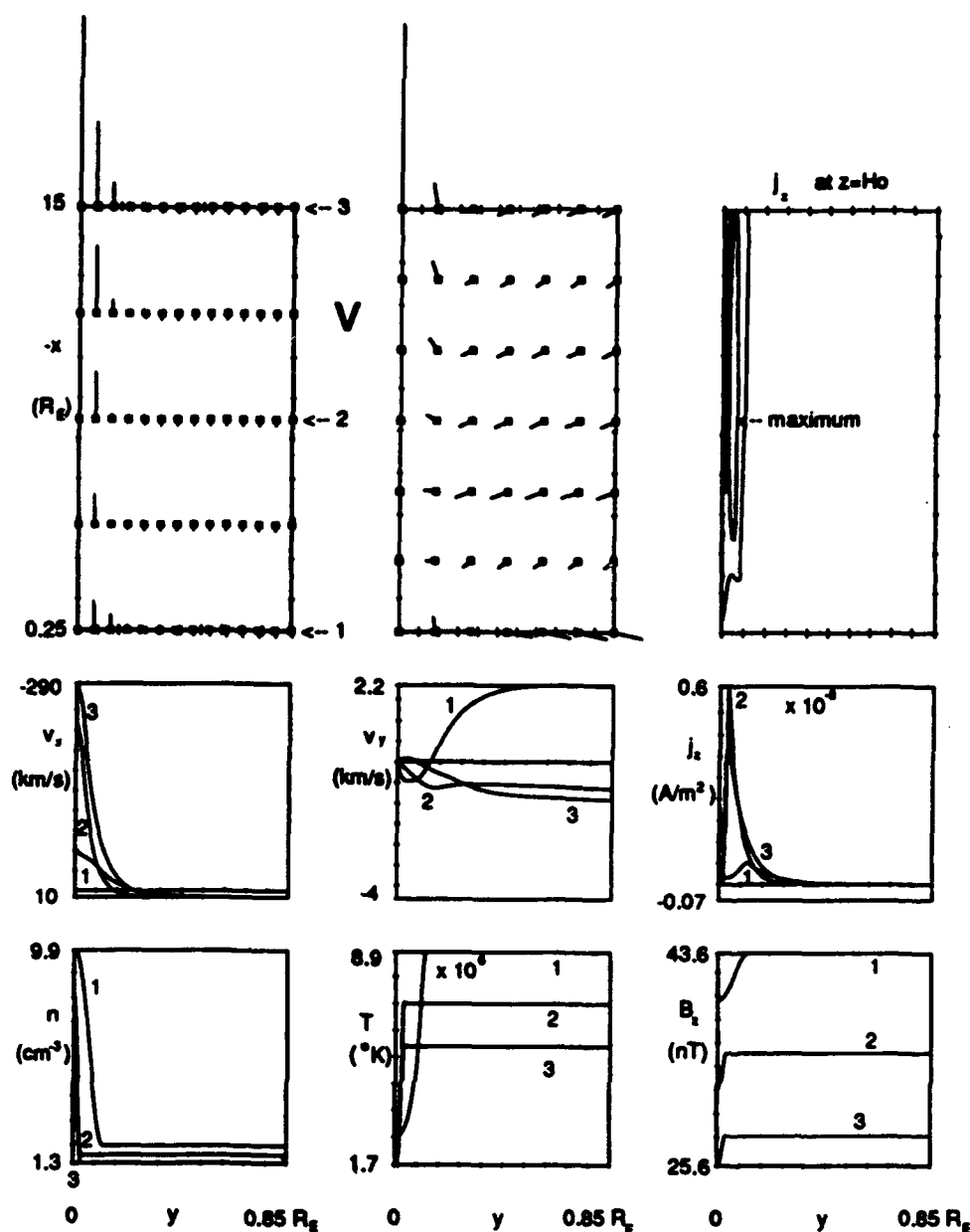
Fig. 4. Results from run 3: dynamic viscosity proportional to ρ/B_z and three times lower than in run 2. The computational box ends at $y = 0.18\ R_E$, $0.15\ R_E$, and $0.21\ R_E$ at the locations 1, 2 and 3, respectively. The velocity layer is thinner than in runs 1 and 2. No current reversal ($j_z < 0$) is present in this case.

upper and lower edges of the LLBL, at $s = \pm H_0$, represent the dayside region 1 current system [Iijima and Potemra, 1976a], or at least those portions of it that are generated on closed field lines. These currents are found to form a secondary maximum away from the magnetopause. Between the magnetopause maximum and the secondary maximum a current minimum occurs, often including a reversal of the current. The region 1 field-aligned current peak is found to reach a maximum at a certain local time, as observed by Iijima and Potemra [1976a]. However, experience with the Lotko et al. [1987] model indicates that significant changes in the details of velocity and field-aligned current distributions will occur when field-aligned potential drops are incorporated.

In the future the model will be improved in the following two

major respects. First, the ionosphere will be incorporated in a more realistic way. The connection region between the LLBL and the ionosphere is a narrow channel starting at the upper and lower edges of the boundary layer, that is, at $s = \pm H_0$, where the currents are field-aligned and extending along the magnetic field into the ionosphere. In this region the magnetic field will be calculated self-consistently, rather than by using the constant mapping factor (dx_i/dz) employed here. Also, field-aligned potential drops will be included as in the works by Lotko et al. [1987] and Phan et al. [1989], according to the empirical formula $j_{\|i} = K(\phi_e - \phi_i)$. Here $j_{\|i}$ is the field-aligned current into the ionosphere, K is an effective field-aligned conductance density, and ϕ_e and ϕ_i are the electric potential at $s = \pm H_0$ and in the ionosphere, respectively. The
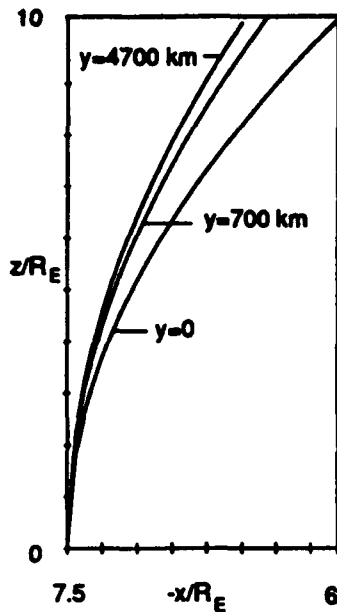
24

Fig. 5. Magnetic-field lines in the dawnside LLBL from run 2 at $x = -7.5\ R_E$. View from outside the layer, looking towards the magnetosphere, with the Sun on the right. The lines have approximately parabolic shape (exaggerated in the plot by a factor of 3.3 in the horizontal scale) and maximum curvature near the magnetopause.

ionosphere will continue to be treated as a conductive substrate; combining Ohm's law with current continuity and the boundary layer approximation, we can show that

$$\frac{\partial}{\partial y_i}\Sigma_p\frac{\partial\phi_i}{\partial y_i} = -j_{\|i} .$$

The height-integrated Pedersen conductivity Σ_p may have a spatial dependence or a dependence on the electron precipitation associated with the field-aligned potential drops.

The second improvement of the model is to include a variable height $H_0(x, y)$ of the LLBL, to be calculated self-consistently with the other variables. In this case the velocity component v_z will not be zero, except at $z = 0$; it will be allowed to have a linear z dependence. The surface $z = \pm H_0(x, y)$ will be located where the plasma pressure in the layer, as determined by the z momentum equation (equation (8)), has dropped to its magnetospheric value. By requiring the velocity to be tangential to that surface it can be shown that the mass conservation law, at $z = 0$, becomes

$$\frac{\partial}{\partial x}(H_0\rho_0v_{x0}) + \frac{\partial}{\partial y}(H_0\rho_0v_{y0}) = 0$$

As a further generalization, this equation may be modified to allow plasma entry from the upper and lower edges of the LLBL, at $z = \pm H_0(x, y)$.

Further improvements of the model can be made by permitting mass diffusion across the magnetic field.

REFERENCES

Akasofu, S.-I., E. Hones, Jr., S.J. Bame, J.R. Asbridge, and A.T.Y. Lui, Magnetotail and boundary layer plasma at geocentric distance of 18 RE: Vela 5 and 6 observations, *J. Geophys. Res., 78*, 7257, 1973.

Anderson, D.A., J.C. Tannehill, and R.H. Fletcher (Eds.), *Computational Fluid Mechanics and Heat Transfer*, p. 329, McGraw-Hill, New York, 1984.

Atkinson, G., An approximate flow equation for geomagnetic flux tubes and its application to polar substorms, *J. Geophys. Res., 72*, 5373, 1967.

Burden, R.L., and J.D. Faires, *Numerical Analysis*, p. 536, PSW-KENT, Boston, Mass., 1989.

Chiu, Y.T., and J.M. Cornwall, Electrostatic model of a quiet auroral arc, *J. Geophys. Res., 85*, 543, 1980.

Coleman, P.J., Jr., A Model of the geomagnetic cavity, *Radio Sci., 6*, 321, 1971.

Cowley, S.W.H., and J. Owen, A simple illustrative model of open flux tube motion over the dayside magnetopause, *Planet. Space Sci., 37*, 1461, 1989.

Dungey, J.W., The structure of the exosphere or adventures in velocity space, in *Geophysics, The Earth's Environment*, edited by C. DeWitt et al., p. 526, Gordon and Breach, New York, 1963.

Eastman, T.E., and E.W. Hones., Jr., Characteristics of the magnetospheric boundary layer and magnetopause layer as observed by IMP 6, *J. Geophys. Res., 84*, 2019, 1979.

Eastman, T.E., E.W. Hones, Jr., S.J. Bame, and J.R. Asbridge, The magnetospheric boundary layer: Site of plasma, momentum and energy transfer from the magnetosheath to the magnetosphere, *Geophys. Res. Lett., 3*, 685, 1976.

Fridman, M., and J. Lemaire, Relationship between auroral electron fluxes and field-aligned electric potential differences, *J. Geophys. Res., 85*, 664, 1980.

Haerendel, G., G. Paschmann, N. Sckopke, and H. Rosenbauer, Frontside boundary layer of the magnetosphere and the problem of reconnection, *J. Geophys. Res., 83*, 3195, 1978.

Hones, E.W., Jr., J. R. Asbridge, S. J. Bame, M. D. Montgomery, S. Singer, and S.-I. Akasofu, Measurements of the magnetotail plasma flow made by VELA 4B, *J. Geophys. Res., 77*, 5503, 1972.

Iijima, T., and T.A. Potemra, The amplitude distribution of field-aligned currents at northern high latitudes observed by TRIAD, *J. Geophys. Res., 81*, 2165, 1976a.

Iijima, T., and T. A. Potemra, Field-aligned currents in the dayside cusp observed by TRIAD, *J. Geophys. Res., 81*, 5971, 1976b.

Kan, J.R., and L.C. Lee, Theory of imperfect magnetosphere-ionosphere coupling, *Geophys. Res. Lett., 7*, 633, 1980.

LaBelle, J., and R.A. Treumann, Plasma waves at the dayside magnetopause, *Space Sci. Rev. 47*, 175, 1988.

Lotko, W., B.U.Ö. Sonnerup, and R.L. Lysak, Nonsteady boundary layer flow including ionospheric drag and parallel electric fields, *J. Geophys. Res., 92*, 8635, 1987.

Lyons, L. R., Generation of large-scale regions of auroral currents, electric potential, and precipitation by the divergence of the convection electric field, *J. Geophys. Res., 85*, 17, 1980.

Mitchell, D.G., F. Kutchko, D.J. Williams, T.E. Eastman, L.A. Frank, and C.T. Russell, An extended study of the low-latitude boundary layer on the dawn and dusk flanks of the magnetosphere, *J. Geophys. Res., 92*, 7394, 1987.

Mozer, F.S., Electric field evidence on the viscous interaction at the magnetopause, *J. Geophys. Res., 11*, 135, 1984.

Paschmann, G., G. Haerendel, N. Sckopke, and H. Rosenbauer, Plasma and field characteristics of the distant polar cusp near local noon: the entry layer, *J. Geophys. Res., 81*, 2883, 1976.

Phan, T.D., B.U.Ö. Sonnerup, and W. Lotko, Self-consistent model of the low latitude boundary layer, *J. Geophys. Res., 94*, 1281, 1989.

Reyhner, T.A., and I. Flügge-Lotz, The interaction of a shock wave with a laminar boundary layer, *Int. J. Non-Linear Mech., 3*, 173, 1968.

Sckopke, N., G. Paschmann, G. Haerendel, B.U.Ö. Sonnerup, S. J. Bame, T. G. Forbes, E. W. Hones, Jr., and C. T. Russell, Structure of the low-latitude boundary layer, *J. Geophys. Res., 86*, 2099, 1981.

Siscoe, G.L., and N. Maynard, Distributed two-dimensional Region 1 and Region 2 currents: Model results and data comparisons, *J. Geophys. Res., 96*, 21,071, 1991.

Siscoe, G.L., W. Lotko, and B.U.Ö. Sonnerup, A high-latitude, low-latitude boundary layer model of the convection current system, *J. Geophys. Res., 96*, 3487, 1991.

Sonnerup, B.U.Ö., Theory of the low-latitude boundary layer, *J. Geophys. Res., 85*, 2017, 1980.

Sonnerup, B.U.Ö., G. Paschmann, T.D. Phan, and H. Lühr, Magnetic field maxima in the low latitude boundary layer, *Geophys. Res. Lett.*, *19*, 1727, 1992.

Song, P., and C.T. Russell, Model of the formation of the low-latitude boundary layer for strongly northward interplanetary magnetic field, *J. Geophys. Res.*, *97*, 1411, 1992.

Southwood, D.J., Magnetopause Kelvin-Helmholtz instability, in Magnetospheric Boundary Layers, edited by B. Battrick, *ESA Spec. Publ.*, *SP-148*, 357, 1979.

Spitzer, L., Jr., *Physics of Fully Ionized Gases*, p. 146, Interscience, New York, 1962.

Traver, D.P., D.G. Mitchell, D.J. Williams, L.A. Frank, and C.Y. Huang, Two encounters with flank low-latitude boundary layer: further evidence for closed field topology and investigation of the internal structure, *J. Geophys. Res.*, *96*, 21,025, 1991.

Tsurutani, B.T., and R.M. Thorne, Diffusion processes in the magnetopause boundary layer, *Geophys. Res. Lett.*, *9*, 1247, 1982.

Wei, C. Q., and L. C. Lee, Coupling of magnetopause-boundary layer to the polar ionosphere, *J. Geophys. Res.*, *98*, 5707, 1993.

Wei, C. Q., L. C. Lee, and A. L. LaBelle-Hamer, A simulation study of the vortex structure in the low-latitude boundary layer, *J. Geophys. Res.*, *95*, 20,793, 1990.

Williams, D.J., D.G. Mitchell, T.E. Eastman, and L.A. Frank, Energetic particle observations in the low-latitude boundary layer, *J. Geophys. Res.*, *90*, 5097, 1985.

Woch, J., M. Yamauchi, R. Lundin, T.A. Potemra, and L.J. Zanetti, The low-latitude boundary layer at mid-altitudes: relation to large-scale Birkeland currents, *J. Geophys. Res.*, *20*, 2251, 1993.

E. Drakou, Herzberg Institute of Astrophysics, National Research Council of Canada, 100 Sussex Drive, Ottawa, Ontario, Canada K1A 0R6.

W. Lotko, and B.U.Ö. Sonnerup, Thayer School of Engineering, Dartmouth College, Hanover, NH 03755.

APPENDIX 2: EXTENSIONS OF THE MODEL

In this chapter, the equations are presented that describe the LLBL with (a) variable height, $2H_0(x,y)$, in the z direction and (b) field-aligned potential drops in the force-free coupling region between the LLBL and the southern and northern ionospheres.

2.1 Variable Boundary Layer Height

The basic formulation of the low-latitude boundary layer model remains as described in Appendix 1, but in addition, the half-height, H_0 is now a function of x and y to be calculated self-consistently. It is assumed that, at the location $z = \pm H_0$, the plasma pressure has fallen to its corresponding magnetospheric value, $p_\infty(x,z)$, which is considered to be a known function of x and z only. At the same location, a force-free ($j \times B = 0$) region begins that connects the LLBL to the two ionospheres. Equations (1)-(5) describe the plasma flow in the equatorial LLBL. By using the series expansions (12) and (14), the mass conservation law, equation (1), evaluated at $z = 0$, takes the following form

$$\frac{\partial(\rho_0 v_{x0})}{\partial x} + \frac{\partial(\rho_0 v_{y0})}{\partial y} + \frac{\rho_0 v_{z1}}{H} = 0 \qquad (45)$$

Notice that v_z is now non-zero everywhere in the LLBL except at $z = 0$. It is required that the plasma velocity vector be tangential to the upper and lower boundary surfaces at $z = \pm H_0$:

$$\{v \cdot \nabla(z - H_0(x,y))\}_{z=\pm H_0} = 0$$

or, by keeping the zeroth and first-order terms only in the series expansion in z,

$$-\frac{v_{x0}\partial H_0}{\partial x} - \frac{v_{y0}\partial H_0}{\partial y} + \frac{v_{z1} H_0}{H} = 0 \qquad (46)$$

By substituting v_{z1}/H from (46) into (45), the mass conservation law finally becomes

$$\frac{\partial(\rho_0 H_0 v_{x0})}{\partial x} + \frac{\partial(\rho_0 H_0 v_{y0})}{\partial y} = 0 \qquad (47)$$

The induction law should now be used in the form of equation (19), instead of (20), since the latter was derived by use of (15), which is no longer valid.

The x and y components of the momentum conservation law, equation (2), evaluated at $z = 0$, are given by equations (16) and (17). In the boundary layer approximation, described in Appendix 1, the z-momentum equation is given by

$$\frac{\partial(p + B_z^2/2\mu_0)}{\partial z} = \frac{1}{\mu_0}(B_x \frac{\partial B_z}{\partial x} + B_y \frac{\partial B_z}{\partial y}) - \rho v \cdot \nabla v_z + \frac{\partial}{\partial y}(\eta \frac{\partial v_z}{\partial y}) \qquad (48)$$

In the above equation, the magnetic terms on the right are of order (H/L) compared to the term on the left-hand side, and the inertia and viscous terms are of order $(H/L)^2$, where H and L are the characteristic scale lengths for changes in the z direction and the x direction, respectively. At this point, one can proceed to different levels of approximation: if H/L is of order unity, one would need to solve the full z-momentum equation; if H/L is much less than unity, one can either neglect the terms of order $(H/L)^2$ and keep the terms of order H/L, or neglect both. In the following we will neglect terms of order $(H/L)^2$, a choice that is consistent with the assumption that second order terms in the z expansions could also be neglected. According to this latter assumption, terms of order H/L should be kept; however, significant simplifications result from neglecting those terms as well. The two different options for the z-momentum equation are stated below.

(1) *Terms of order H/L and $(H/L)^2$ are neglected*

In this case, the z-momentum equation (8) reduces to the simple pressure balance

$$p + \frac{B_z^2}{2\mu_0} = p_0(x, y) \qquad (49)$$

where $p_0(x,y)$ is the plasma pressure in the equatorial plane. If the left-hand side of the expression is now evaluated at $z = \pm H_0$ where the pressure has become equal to the magnetospheric plasma pressure, $p_\infty(x, H_\infty)$, evaluated at the top of the boundary layer, one finds

$$p_0 - p_\infty(x, H_\infty) - \frac{B_{x1}^2 H_0^2}{2\mu_0 H^2} = 0 \tag{50}$$

According to the series expansion in z, the magnetospheric plasma pressure contains a term proportional to z^2, i.e.,

$$p_\infty(x, z) = p_\infty(x, 0) - \left(\frac{z}{H}\right)^2 p_2(x)$$

At $z = H_\infty(x)$ this pressure has reached the value that is assumed to be present at the top of the LLBL, $z = H_0$, throughout the layer, as shown in Figure 6. Its value, $p_\infty(x, H_\infty)$ is considered known so that equation (50) can be used to calculate $H_0(x, y)$.

(2) *Terms of order (H/L) retained*

In this case, the z-momentum equation (8) reduces to the static force balance

$$p_0 - p_\infty(x, H_\infty) - \frac{B_{x1}^2 H_0^2}{2\mu_0 H^2} = -\left(\frac{B_{x1}}{\mu_0}\frac{\partial B_{x0}}{\partial x} + \frac{B_{y1}}{\mu_0}\frac{\partial B_{x0}}{\partial y}\right)\frac{H_0^2}{2H} \tag{51}$$

which replaces (50) as the equation for $H_0(x,y)$. In this expression the y component of the magnetic field can be obtained from equation (5), which simplifies to the form

$$\frac{\partial B_{x1}}{\partial x} + \frac{\partial B_{y1}}{\partial y} = 0 \tag{52}$$

provided $\partial B_z/\partial z$ is zero which is the case if quadratic and higher-order terms in the series expansion of B_z are neglected.

The system of equations (46), (47), (16), (17), (51), (18), (19) and (52) contains nine unknown quantities, namely, v_{x0}, v_{y0}, v_{z1}, B_{x1}, B_{y1}, B_{x0}, ρ_0, p_0 and H_0. If option

(1) above is used B_{y1} does not appear, except in equation (52), and equation (50) replaces (51). To obtain a closed system of equations, coupling to the ionosphere must be incorporated. We first apply current continuity at $z = \pm H_0$. The surface $z = H_0(x, y)$ is defined by the equation $F(x, y, z) = z - H_0(x, y) = 0$; the unit vector normal to this surface is $\hat{n} = \nabla F / |\nabla F|$. In what follows, all quantities just below the surface $F = 0$ carry the superscript $-$ while quantities just above $F = 0$ carry the superscript $+$. Current continuity across the surface $z = H_0(x, y)$ implies that

$$j^- \cdot \hat{n} = j^+ \cdot \hat{n} \tag{53}$$

where the current j^- at $z = H_0^-$ is given by (9)-(11). By use of these equations and the magnetic field as given by (13) one then finds

$$\frac{1}{\mu_0} \frac{\partial B_{x0}}{\partial y} \frac{\partial H_0}{\partial x} + \frac{1}{\mu_0} \frac{\partial H_0}{\partial y} \left(\frac{B_{x1}}{H} - \frac{\partial B_{x0}}{\partial x} \right) + \frac{H_0}{\mu_0 H} \frac{\partial B_{x1}}{\partial y} = j_x^+ \frac{\partial H_0}{\partial x} + j_y^+ \frac{\partial H_0}{\partial y} - j_z^+ \tag{54}$$

The force free condition above the surface $F = 0$, namely $j^+ \times B^+ = 0$, along with $B^- = B^+$, which implies that there are no surface currents at $z = H_0$, result in

$$\frac{j_x^+}{j_z^+} = \frac{H B_{x0}}{H_0 B_{x1}} \ , \quad \frac{j_z^+}{j_y^+} = \frac{H B_{x0}}{H_0 B_{y1}} \tag{55}$$

If the magnetic field lines in the coupling region are equipotentials, the relationship between the electric field E_y at the top of the LLBL and E_i in the ionosphere is, to lowest order, given by

$$E_i = E_y \frac{dy}{dy_i} \cong v_{x0} B_{x0} \frac{dy}{dy_i} \tag{56}$$

Here, dy_i is the ionospheric counterpart of a length element dy in the equatorial LLBL; a relation between these lengths is obtained from the conservation of flux in a magnetic flux tube

$$\frac{dy_i}{dy} = \frac{B_{x0}}{B_i} \frac{dx}{dx_i} \tag{57}$$

where B_i is the ionospheric magnetic field and dx_i is the ionospheric counterpart of an equatorial length element dx. Note that if the equatorial vector elements $d\boldsymbol{x}$ and $d\boldsymbol{y}$ are orthogonal, the corresponding ionospheric elements $d\boldsymbol{x}_i$ and $d\boldsymbol{y}_i$ are generally not orthogonal and vice versa. However, in the boundary layer approximation this feature of the mapping does not enter the equations explicitly. The ratios dx/dx_i and dy/dy_i are known only after the field-line geometry in the coupling region has been calculated self-consistently, as explained later in this chapter. In the simplest case, one may assume a known average value for this ratio, as was done in Appendix 1.

In the ionosphere, the height integrated current is

$$\boldsymbol{I}_i = \Sigma_P(\boldsymbol{E}_i + \boldsymbol{v}_n \times \boldsymbol{B}_i) - \Sigma_H(\boldsymbol{E}_i + \boldsymbol{v}_n \times \boldsymbol{B}_i) \times \hat{\boldsymbol{z}}_i \tag{58}$$

In the above equation, Σ_I is the height-integrated Pedersen conductivity, Σ_H is the height integrated Hall conductivity, and $\boldsymbol{v}_n$ is the ionospheric neutral wind velocity. By applying current continuity at the top of the ionosphere and by assuming constant $\boldsymbol{v}_n$ and $\boldsymbol{B}_i$ we can use the boundary layer approximation to find

$$j_{\|_i} = \boldsymbol{\nabla}_i \cdot \boldsymbol{I}_i = \frac{\partial}{\partial y_i}(\Sigma_P E_i) = \frac{dy}{dy_i}\frac{\partial}{\partial y}(\Sigma_P E_i) \tag{59}$$

where $j_{\|_i}$ is the field-aligned current leaving the ionosphere. From charge and magnetic flux conservation it also follows that

$$\frac{j_{\|_i}}{j_z^+} = \frac{B_i}{B_{x0}} \tag{60}$$

By use of (56) and (57) equation (59) becomes

$$j_{\|_i} = \frac{B_i}{B_{x0}}\frac{dx_i}{dx}\frac{\partial}{\partial y}\left(\Sigma_P \frac{B_i}{B_{x0}}\frac{dx_i}{dx}v_{x0}B_{x0}\right) \tag{61}$$

Finally, by use of (55) and (60) equation (54) gives

$$\frac{1}{\mu_0}\frac{\partial B_{x0}}{\partial y}\frac{\partial H_0}{\partial x} + \frac{1}{\mu_0}\frac{\partial H_0}{\partial y}\left(\frac{B_{x1}}{H} - \frac{\partial B_{x0}}{\partial x}\right) + \frac{H_0}{\mu_0 H}\frac{\partial B_{x1}}{\partial y} =$$

31

$$\frac{j_{\|_i}}{B_i}\{\frac{H_0 B_{x1}}{H}\frac{\partial H_0}{\partial x} + \frac{H_0 B_{y1}}{H}\frac{\partial H_0}{\partial y} - B_{x0}\}. \tag{62}$$

In the approximation (2) in which terms of order H/L are retained, all terms in (62) must be used; in the approximation (1) in which both terms of order H/L and $(H/L)^2$ are neglected compared to terms of order unity, it simplifies to

$$\frac{1}{\mu_0}\frac{\partial B_{x0}}{\partial y}\frac{\partial H_0}{\partial x} + \frac{1}{\mu_0}\frac{\partial H_0}{\partial y}(\frac{B_{x1}}{H} - \frac{\partial B_{x0}}{\partial x}) + \frac{H_0}{\mu_0 H}\frac{\partial B_{x1}}{\partial y} = -j_{\|_i}\frac{B_{x0}}{B_i} \tag{63}$$

In this case, equations (61) and (63) close the system (46), (47), (16), (17), (50), (18), (19) and (52) mentioned above, with one more dependent variable, namely $j_{\|_i}$. For convenience, the complete system of equations to lowest order is repeated here:

$$\frac{\partial(\rho_0 H_0 v_{x0})}{\partial x} + \frac{\partial(\rho_0 H_0 v_{y0})}{\partial y} = 0$$

$$\rho_0(v_{x0}\frac{\partial}{\partial x} + v_{y0}\frac{\partial}{\partial y})v_{x0} = -\frac{dP_\infty(x)}{dx} + \frac{1}{\mu_0 H}B_{x0}B_{x1} + \frac{\partial}{\partial y}(\eta_0\frac{\partial v_{x0}}{\partial y})$$

$$p_0 + \frac{B_{x0}^2}{2\mu_0} = P_\infty(x)$$

$$p_0 - p_\infty(x, H_\infty) - \frac{H_0^2 B_{x1}^2}{2\mu_0 H^2} = 0$$

$$(v_{x0}\frac{\partial}{\partial x} + v_{y0}\frac{\partial}{\partial y})\frac{p_0}{\rho_0^\gamma} = 0$$

$$\frac{\partial(B_{x0}v_{x0})}{\partial x} + \frac{\partial(B_{x0}v_{y0})}{\partial y} = 0$$

$$-\frac{v_{x0}\partial H_0}{\partial x} - \frac{v_{y0}\partial H_0}{\partial y} + \frac{v_{z1}H_0}{H} = 0$$

$$\frac{\partial B_{x1}}{\partial x} + \frac{\partial B_{y1}}{\partial y} = 0$$

2.2 Field-Aligned Potential Drops

In addition to all features of the LLBL, the ionospheric substrate, and the force-free region connecting the two, described in the previous sections, the field-aligned

current in the ionosphere, $j_{\|_i}$, is now assumed to be given by the lumped relation

$$j_{\|_i} = \kappa(\phi_e - \phi_i) \tag{64}$$

where κ is an effective field-aligned conductance density and the subscripts e and i denote quantities evaluated at the top of the boundary layer and the ionosphere, respectively. The potential distribution in the LLBL region is

$$\phi_e = -\int_0^y E_y dy = -\int_0^y v_{x0}B_{x0}dy \tag{65}$$

The potential distribution in the ionosphere is related to the ionospheric electric field by $\mathbf{E}_i = -\nabla_i \phi_i$. By use of this expression for $\mathbf{E}_i$, and by noting that in the boundary layer approximation $E_{xi} \ll E_{yi}$, equation (59) becomes

$$j_{\|_i} = -\frac{dy}{dy_i}\frac{\partial}{\partial y}(\Sigma_P \frac{dy}{dy_i}\frac{\partial \phi_i}{\partial y}) \tag{66}$$

By substituting ϕ_i from (64) into (66) and by using (57) and (65), one then finds

$$j_{\|_i} = \Sigma_P \left(\frac{B_i}{B_{x0}}\frac{dx_i}{dx}\right)^2 \left(\frac{1}{\kappa}\frac{\partial^2 j_{\|_i}}{\partial y^2} + \frac{\partial(v_{x0}B_{x0})}{\partial y}\right)$$
$$-\frac{B_i}{B_{x0}}\frac{dx_i}{dx}\frac{\partial}{\partial y}(\Sigma_P \frac{B_i}{B_{x0}}\frac{dx_i}{dx})\left(\frac{1}{\kappa}\frac{\partial j_{\|_i}}{\partial y} + v_{x0}B_{x0}\right) \tag{67}$$

Equation (67) instead of (61) now completes the system of equations derived above. Note that, without field-aligned potential drops, i.e., with $\kappa = \infty$, equation (67) reduces to equation (61).

2.3 Asymptotic Solution

The system of equations in the previous sections cannot be integrated in the region of slow sunward flow by a marching procedure in the $-x$ direction, for the reasons mentioned in Appendix 1. As in the approach taken in that Appendix, the term $v_{x0}\partial v_{x0}/\partial x$ in the x-momentum equation will be neglected in the slow sunward

33

flow region. However, it is not possible to derive a simple solution there under the same assumptions as in Appendix 1, namely, that B_{x0}, p and ρ are independent of y. The reason is that the z-momentum equation, in its simplest form (i.e., equation (50)), forces the height H_0 to be a function of both x and y. The remaining equations are then inconsistent with those assumptions and without them, we have not found a simple straightforward method to reduce the equations describing the LLBL in the asymptotic region to a system of ordinary differential equations. One then has the option, either to integrate this system, without the above inertia term in the x-momentum equation, using the same numerical method as in the computational box in Appendix 1, or to make the assumption that the height of the layer is a function of x only and does not vary with y. In the latter case, the z-momentum equation cannot be used to satisfy the condition that the pressure drops to its magnetospheric value at $z = H_0$. Instead, the pressure above and below the surface $z = H_0$ will be different, except in the magnetosphere where $H_0 = H_\infty(x)$ is chosen to provide continuity of pressure across this surface. As explained in the next two sections, one may account for this pressure difference by including a surface current at $z = H_0$, as shown in Figure 6. Note that this pressure difference has been ignored in the earlier models by *Sonnerup* [1980] and *Lotko et al.* [1987].

(1) *No Surface Currents at $z = H_0$*

In this approach the resulting pressure at $z = H_0$ differs from the magnetospheric pressure; the difference can be considered as the pressure exerted mechanically by the surface itself on the LLBL; it results in an inconsistent evaluation of the currents and the magnetic field above the surface $z = H_0$. This approach, however, leads to a simple analytic solution in the asymptotic region, under certain assumptions to

be explained presently. It should be mentioned that the analysis presented below is essentially the same as that performed by *Lotko et al.* [1987] and used by *Siscoe et al.* [1991], and *Siscoe and Maynard* [1991].

As in Appendix 1, we will assume that B_{x0}, p and ρ are independent of y. This assumption is not necessary, but it is now allowed by the equations, and it is used to illustrate the simplest case. With the above assumptions, the current continuity, equation (63), becomes

$$\frac{H_0}{\mu_0 H}\frac{\partial B_{x1}}{\partial y} = -\frac{B_{x0}}{B_i}j_{\|_i} \tag{68}$$

and the x-momentum equation becomes

$$\eta_0\frac{\partial^2 v_{x0}}{\partial y^2} - \frac{dP_\infty(x)}{dx} + \frac{1}{\mu_0 H}B_{x0}B_{x1} = \rho_0 v_{y0}\frac{\partial v_{x0}}{\partial y} \tag{69}$$

Equation (67) can be written in the following form if one assumes that Σ_P, B_i and dx_i/dx are also independent of y in the asymptotic region.

$$(\frac{1}{c^2} - \lambda^2\frac{\partial^2}{\partial y^2})j_{\|_i} = \Sigma_P B_{x0}\frac{\partial v_{x0}}{\partial y} \tag{70}$$

where, using the notation of *Lotko et al.* [1987]

$$c = \frac{B_i}{B_{x0}}\frac{dx_i}{dx}, \quad \lambda = \sqrt{\frac{\Sigma_P}{\kappa}} \tag{71}$$

We now operate on (69) with $(1/c^2 - \lambda^2\partial^2/\partial y^2)\partial/\partial y$ and express $\partial B_{x1}/\partial y$ in terms of $j_{\|_i}$ from (68). Furthermore, we neglect the y-dependence of v_{y0} in the asymptotic region. The result is

$$(\frac{1}{c^2} - \lambda^2\frac{\partial^2}{\partial y^2})\frac{\partial}{\partial y}\left(\eta_0\frac{\partial^2 v_{x0}}{\partial y^2} - \rho_0 v_{y0}(x, y_b)\frac{\partial v_{x0}}{\partial y}\right) - \frac{B_{x0}^2}{H_0 B_i}(\frac{1}{c^2} - \lambda^2\frac{\partial^2}{\partial y^2})j_{\|_i} = 0 \tag{72}$$

which, after substitution of the right most term from (70) and one integration, becomes

$$\frac{\partial}{\partial y}\left(\frac{\partial^2}{\partial y^2} - \frac{1}{c^2\lambda^2}\right)\left(\frac{\partial}{\partial y} - \frac{\rho_0 v_{y0}(x, y_b)}{\eta_0}\right)v_{x0} + \frac{\Sigma_P B_{x0}^3}{\eta_0\lambda^2 H_0 B_i}v_{x0} = \frac{\Sigma_P B_{x0}^3}{\eta_0\lambda^2 H_0 B_i}v_{x\infty} \tag{73}$$

The above equation has the general solution

$$v_{x0} = v_{x\infty} + e^{-c_1 y}(A\cos(c_2 y) + B\sin(c_2 y)) \tag{74}$$

where the growing exponential has been discarded. The constants A and B are to be determined from the boundary conditions at $y = y_b$. Furthermore, c_1 and c_2 can be obtained by requiring the first and second derivative of v_x to be continuous at the interface between the computational and the asymptotic region.

(2) *Surface Current at* $z = H_0$

In addition to the assumptions used in case (1), a surface current K is now assumed to flow in the surface $z = H_{0,}$. This current exerts a vertical force on the plasma in the boundary layer which represents the net effect of j_y currents flowing in the "triangular" (shaded) region in Figure 6, and accounts for the difference in pressure at the edge of the LLBL (at $z = H_0 = H_\infty(x)$) and the magnetospheric pressure. This requirement is given by the relation

$$K_y \frac{B_x^+ + B_x^-}{2} = p^+ - p^- \tag{75}$$

where the superscripts $+$ and $-$ denote quantities evaluated above and below the surface $z = H_0$, respectively. In the above equation, the magnetic field in the surface $z = H_\infty$ is the average between the value above and below this surface. In the boundary layer approximation, the boundary condition on the magnetic field there requires that $B_x^+ - B_x^- = \mu_0 K_y$, where $B_x^- = (H_0/H)B_{x1}$. The plasma pressure below the surface, p^-, which can be taken from the z-momentum equation (49), is equal to $p_0 - B_{x1}^2 H_0/2\mu_0 H^2$; the plasma pressure above the surface is the magnetospheric plasma pressure at $z = H_\infty$, i.e., it is $p_\infty(x, H_\infty)$. With those substitutions, the

relation (75) gives the surface current K_y

$$K_y = -\frac{H_0}{\mu_0 H}B_{x1} + \sqrt{\frac{2H_0^2}{\mu_0^2 H^2}B_{x1}^2 + 2\frac{p_0 - p_\infty}{\mu_0}} \tag{76}$$

The condition of current continuity at $z = H_0$ should now include this surface current, i.e.,

$$j^- \cdot \hat{n} = j^+ \cdot \hat{n} + \frac{\partial K_y}{\partial y} \tag{77}$$

which leads to

$$\frac{H_0}{\mu_0 H}\frac{\partial B_{x1}}{\partial y} = \frac{B_{x0}}{B_i}j_{\|_i} + \frac{\partial K_y}{\partial y} \tag{78}$$

Equations (69), (70) and (78) contain x only as a parameter; they are in effect ordinary differential equations which, along with (76), can be used to calculate v_{x0}, B_{x1} and $j_{\|_i}$ as functions of y at any x location.

2.4 Self-Consistent Coupling Region

It is an important objective of a boundary layer model to provide the actual mapping of the magnetic field lines from the equatorial LLBL to the ionosphere. In order to accurately provide this information, the model must include a self-consistent calculation of the magnetic field deformation in the coupling region, i.e., it must incorporate the mapping factor dx/dx_i in a self-consistent manner. This can be accomplished by an iterative procedure, as follows: In the first iteration a constant value of the above ratio is used, equal to the value given by an internal magnetospheric model, such as the Tsyganenko model. After the model equations have been solved numerically, the magnetic field geometry in the LLBL will be known. A force-free boundary layer model can then be used to calculate the further deformation of the magnetic field in the connecting region that is caused by field-aligned currents there.

This calculation will provide the new mapping factor dx/dx_i to be used in a second iteration in the LLBL model, and so on. A self-consistent boundary-layer model of the connecting region is currently under development by Professor Lotko and his students [see Appendix 5].

REFERENCES

Lotko, W., B.U.Ö. Sonnerup, and R.L. Lysak, Nonsteady boundary layer flow including ionospheric drug and parallel electric fields, *J. Geophys. Res.*, *92*, 8635, 1987.

Siscoe, G.L., W. Lotko, and B.U.Ö. Sonnerup, A high-latitude, low-latitude boundary layer model of the convection current system, *J. Geophys. Res.*, *96*, 3487, 1991.

Siscoe, G.L., and N. Maynard, Distributed two-dimensional Region 1 and Region 2 currents: Model results and data comparisons, *J. Geophys. Res.*, *96*, 21,071, 1991.

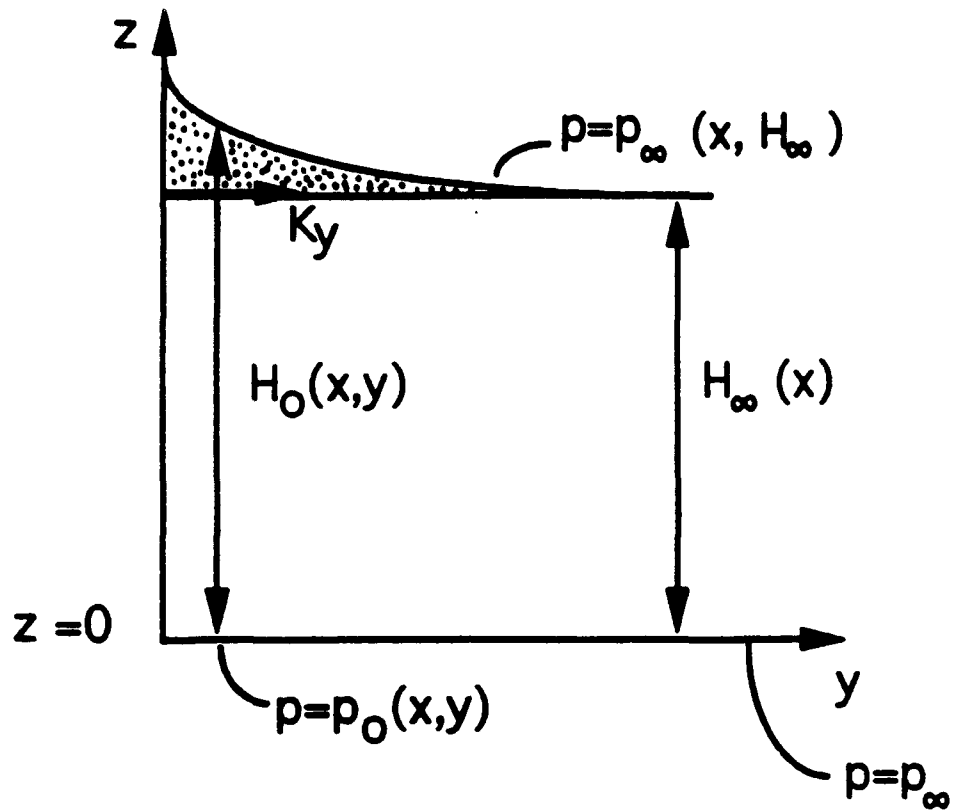Sonnerup, B.U.Ö., Theory of the low-latitude boundary layer, *J. Geophys. Res.*, *85*, 2017, 1980.

Fig. 6. A schematic of the LLBL height, H_0, as a function of y at fixed x value. If $H_0(x)$ is assumed independent of y and equal to $H_\infty(x)$, a surface current K_y can be used to account for the difference in pressure above and below the surface $z = H_\infty$.

APPENDIX 3: NUMERICAL METHOD

In Appendix 1, it was explained how the system of equations (15), (17), (18), (20) and (26), i.e., the mass conservation law, the y component of the momentum equation, the isentropic law, the induction law, and the x component of the momentum equation, respectively, all evaluated at the equatorial plane, ($z = 0$), were solved by a numerical procedure. The reader is reminded that the model represented by those equations does not include field-aligned potential drops in the coupling region between the LLBL and the ionosphere, and assumes that the LLBL has constant height in the z direction.

As already mentioned, the computational box is a rectangular region in the xy plane. The lines $y = 0$ and $y = y_\infty$ represent the magnetopause and the magnetospheric boundaries, respectively; appropriate boundary conditions are applied there. At the line $x = 0$, the upstream conditions across the boundary layer (i.e., in the y direction) are imposed. The box is divided into two parts: the first part, attached to the magnetopause, extends from $y = 0$ to $y = y_b$; in this part, the velocity in the negative x direction is higher than a chosen small positive value, v_{min}. In the present chapter, the finite difference method used in this part of the box is explained in some detail. The analytical method used in the box attached to it, called the asymptotic box, and extending from $y = y_b$ to $y = y_\infty$, was explained in Appendix 1. A schematic of the computational region and the asymptotic region is shown in Figure 7.

The system of equations contains five unknown quantities, namely, $v_{x0}(x,y)$, $v_{y0}(x,y)$, $B_{x0}(x,y)$, $\rho_0(x,y)$ and $p_0(x,y)$; we wish to find the x dependence (along the main antisunward flow direction) and y dependence (across the layer) of these variables. The system is written in a finite difference form according to the Crank-

Nicolson scheme, to be explained presently. There are n+2 grid points in the y direction, including the two boundary grids, and the calculation can proceed for as long as needed along the x direction. The equations are expressed in backward difference form in the x direction; this allows all variables to be calculated (simultanuously at all n grid points in the y direction) at only one step in the x direction each time, based on the values of the previous step. The grids are equally spaced in the x and y directions, but $\Delta x \neq \Delta y$, and also, care is taken so that $\Delta x / \Delta y \approx v_{x0}/v_{y0}$. The latter condition guarantees that information about the velocities in the x and y direction travel a distance of about one step in the corresponding direction in time Δt, i.e., $\Delta t = \Delta x / v_{x0} = \Delta y / v_{y0}$. This marching procedure in the downstream direction takes advantage of the slow parabolic evolution of the flow; in fluid mechanics it has been found to be the most economical method as far as computational time is concerned.

At every step in the x direction, the number of grid points, n, along the y direction is different in general. Before the calculation at each step in x starts, a simple check on the magnitude of v_{x0} at the right boundary is performed; for computational convenience this check is applied at the previous step. If the value is lower than v_{min}, as many grid points as necessary are discarded at the right edge of the box and the calculation at the present step is performed on the remaining grid points. If the value is higher than v_{min}, grid points are added: the values of all variables at those new points at the previous x-step are taken from the asymptotic (analytic) solution explained in Appendix 1. It is sufficient to check the value of v_{x0} at the very last grid point on the magnetospheric edge of the numerical box because the velocity is expected to change with y relatively slowly at that boundary.

3.1 Finite Difference Method

The finite difference form of the x-momentum equation in non-dimensional form is given below. The superscript i denotes the grid-point number in the x direction while the subscript j denotes the grid-point number in the y direction. In the following, the notation for v_{x0}, v_{y0}, B_{x0}, ρ_0, j_y and p_0 is also changed, for convenience, to u, v, B, ρ, j, and p, respectively. The x-momentum equation becomes

$$\frac{[\theta(\rho_j^{i+1}u_j^{i+1}) + (1-\theta)(\rho_j^i u_j^i)](u_j^{i+1} - u_j^i)}{\Delta x} +$$

$$\frac{\theta(\rho_j^{i+1}v_j^{i+1})(u_{j+1}^{i+1} - u_{j-1}^{i+1}) + (1-\theta)(\rho_j^i v_j^i)(u_{j+1}^i - u_{j-1}^i)}{2\Delta y}$$

$$= -\left(\frac{dP_\infty}{dx}\right)^{i+1} +$$

$$\theta\left(R_m u_\infty B_\infty + j_\infty + \frac{dB_\infty}{dx}\right)^{i+1} B_j^{i+1} + (1-\theta)\left(R_m u_\infty B_\infty + j_\infty + \frac{dB_\infty}{dx}\right)^i B_j^i +$$

$$R_m \theta(uB)_j^{i+1} + R_m(1-\theta)(uB)_j^i +$$

$$\frac{1}{\Delta y^2}\left\{\theta\left(\mu_{j+1/2}^{i+1}(u_{j+1}^{i+1} - u_j^{i+1}) - \mu_{j-1/2}^{i+1}(u_j^{i+1} - u_{j-1}^{i+1})\right) + \right.$$

$$\left. (1-\theta)\left(\mu_{j+1/2}^i(u_{j+1}^i - u_j^i) - \mu_{j-1/2}^i(u_j^i - u_{j-1}^i)\right)\right\}, \quad i = 0,\ldots, i_{final}, \; j = 1,\ldots, n \quad (79)$$

In the above, the viscosity is assumed to be of the form $\mu = p^{p1}\rho^{p2}/B^{p3}$. Also, the notation $\mu_{j+1/2} = (\mu_{j+1} + \mu_j)/2$ and $\mu_{j-1/2} = (\mu_j + \mu_{j-1})/2$ is used, with $0 \leq \theta \leq 1$, where θ is a weighting factor. For $\theta = 0$ the method is explicit; in this case, the von Neumann stability constraint presents a severe limitation on the marching step size [e.g., *Anderson et al.*, 1984]. For $\theta = 1$ the method is fully implicit with truncation error $O(\Delta x) + O(\Delta y)^2$. The value for θ used here is 1/2, which gives the Crank-Nicolson implicit scheme with truncation error $O(\Delta x)^2 + O(\Delta y)^2$, when all coefficients and properties are evaluated at the expansion point (i+1/2, j). In this case, no stability constraint arises from the von Neumann analysis.

The y-momentum equation is not a differential equation. One could possibly eliminate one of the variables and not use this equation. However, for the purpose of keeping the non-linear terms as simple as possible in the code, the equation was written in a discrete form and was included in the system along with the other four differential equations. In non-dimensional form, this equation is written as:

$$p_j^{i+1} + \frac{1}{2}(B^2)_j^{i+1} = (P_\infty)^{i+1} \tag{80}$$

The mass conservation law is expanded at the point (i+1/2, j-1/2) as follows:

$$\frac{\rho_j^{i+1} u_j^{i+1} - \rho_j^i u_j^i + \rho_{j-1}^{i+1} u_{j-1}^{i+1} - \rho_{j-1}^i u_{j-1}^i}{\Delta x}$$

$$+\frac{\rho_j^{i+1} v_j^{i+1} - \rho_{j-1}^{i+1} v_{j-1}^{i+1} + \rho_j^i v_j^i - \rho_{j-1}^i v_{j-1}^i}{\Delta y} = 0 \tag{81}$$

Notice that the derivative across the layer (in the y direction) is written in a backward difference form here, while the derivatives across the layer in the x-momentum equation are in a central difference form. As a result, no boundary condition on v_y is required at the right edge of the computational box.

The isentropic law and the induction law are written in a form that contains convective terms similar to the inertia terms in the x-momentum equation; therefore, they are expressed in a similar finite difference form. It should be noted, however, that, in both equations, the derivative across the layer is not represented exactly by a central difference, as in the x-momentum equation, but as a combination of backward and forward differences, with weighting factors θ_1 and $(1 - \theta_1)$, respectively. Without those weighting factors, a numerical oscillation, which grows as the computation proceeds downstream, appears between alternate grid poins in the values of B, ρ and p. Empirically, the value $\theta_1 = 0.35$ was found to work well.

The isentropic law and the induction law have the following finite difference form.

$$\frac{[\theta u_j^{i+1} + (1-\theta)u_j^i]\left((p/\rho^\gamma)_j^{i+1} - (p/\rho^\gamma)_j^i\right)}{\Delta x}$$

$$+\theta v_j^{i+1}\frac{\theta_1\left((p/\rho^\gamma)_j^{i+1} - (p/\rho^\gamma)_{j-1}^{i+1}\right) + (1-\theta_1)\left((p/\rho^\gamma)_{j+1}^{i+1} - (p/\rho^\gamma)_j^{i+1}\right)}{2\Delta y}$$

$$+(1-\theta)v_j^i\frac{\theta_1\left((p/\rho^\gamma)_j^{i} - (p/\rho^\gamma)_{j-1}^{i}\right) + (1-\theta_1)\left((p/\rho^\gamma)_{j+1}^{i} - (p/\rho^\gamma)_j^{i}\right)}{2\Delta y} = 0 \qquad (82)$$

$$\frac{[\theta u_j^{i+1} + (1-\theta)u_j^i]\left(\left(\frac{B}{\rho}\right)_j^{i+1} - \left(\frac{B}{\rho}\right)_j^i\right)}{\Delta x}$$

$$+\theta v_j^{i+1}\frac{\theta_1\left(\left(\frac{B}{\rho}\right)_j^{i+1} - \left(\frac{B}{\rho}\right)_{j-1}^{i+1}\right) + (1-\theta_1)\left(\left(\frac{B}{\rho}\right)_{j+1}^{i+1} - \left(\frac{B}{\rho}\right)_j^{i+1}\right)}{2\Delta y}$$

$$+(1-\theta)v_j^i\frac{\theta_1\left(\left(\frac{B}{\rho}\right)_j^{i} - \left(\frac{B}{\rho}\right)_{j-1}^{i}\right) + (1-\theta_1)\left(\left(\frac{B}{\rho}\right)_{j+1}^{i} - \left(\frac{B}{\rho}\right)_j^{i}\right)}{2\Delta y} = 0 \qquad (83)$$

For a given i value, equations (79)-(83) comprise a system of 5×n algebraic equations with 5×n unknowns, namely, u_j^{i+1}, v_j^{i+1}, B_j^{i+1}, ρ_j^{i+1}, and p_j^{i+1}, where $j = 1,\ldots,n$. Boundary values at the magnetopause, i.e, at j=0, are required by the numerical procedure for all five quantities. At the grid point n+1, i.e., at the boundary between the numerical and the asymptotic box, boundary values are also required for B, ρ and p. Boundary value for v is not required. Note that B, ρ and p at both the magnetospheric boundary and the magnetopause boundary should be consistent with the relations (41) and relations similar to (41), respectively, as explained in chapter 2. The boundary condition on u at the grid point n+1 is a mixed condition, i.e., it contains both the value and the two first derivatives of the quantity, see equation (33). This equation is implemented numerically as follows [Smith, 1984]: equation

44

(33) is written at the grid point n+1, i.e., at $y = y_b$ as

$$u_{n+2} - 2u_{n+1} + u_n = \frac{(u_{n+1} - u_n)^2}{u_{n+1} - u_\infty} \quad \text{for all i} \tag{84}$$

Equation (79) is then written at the grid point n+1, and the value of u_{n+2} is substituted from (84). This results in one additional equation with one additional unknown quantity, namely u_{n+1}. Therefore, the final algebraic system consists of $(5 \times n)+1$ equations with $(5 \times n)+1$ unknowns. The method used to solve this non-linear system is described in the next section.

3.2 Newton's Method

Newton's (or Newton-Raphson's) method is one of the most powerful and well-known numerical methods for solving a root-finding problem $f(x) = 0$ [*Burden and Faires*, 1989]. To indroduce Newton's method, assume that the function f is twice continuously differentiable, and x_a is an approximation to the root, r, of $f(x) = 0$ such that $f'(x_a) \neq 0$, where f' is the derivative of f. One may then consider the Taylor expansion of $f(x)$ around the point x_a:

$$f(x) = f(x_a) + (x - x_a)f'(x_a) + \frac{(x - x_a)^2}{2}f''(q(x)) \tag{85}$$

where $q(x)$ lies between x and x_a. If x_a is a close approximation to r, the quadratic term can be neglected and equation (85), evaluated at $x = r$, gives

$$0 \approx f(x_a) + (r - x_a)f'(x_a) \tag{86}$$

Solving for r

$$r \approx x_a - \frac{f(x_a)}{f'(x_a)} \tag{87}$$

This sets the stage for an iteration procedure, in order to determine the root, r, that starts with an initial approximation x_0 and generates the sequence x_k, defined by

$$x_k = x_{k-1} - \frac{f(x_{k-1})}{f'(x_{k-1})} \tag{88}$$

Newton's method can be generalized to a system of m non-linear algebraic equations of the form $f_\kappa(x_l) = 0$, where $\kappa=1,\ldots,m$ and $l=1,\ldots,m$, or, in vector form $F(X) = 0$, where X is the vector that contains the unknowns. In the present application, $f_\kappa = 0$ represent the five equations of our problem, written in finite difference form at n grids in the y direction across the LLBL, at a particular x location, along with one equation at the boundary grid n+1; x_l represent all the variables, i.e., the unknown values of u, v, B, ρ and p at all n grid points, and u_{n+1}. Thus we have m = (5×n)+1 in the present application.

The functional iteration procedure evolves by first selecting X_0 and then iteratively generating

$$X_k = X_{k-1} - \frac{1}{J(X_{k-1})} F(X_{k-1}) \tag{89}$$

for $k > 0$. Here, $J(X) = \partial f_i / \partial x_j$ is the Jacobian of F, the detailed expression for which is given below. One can prove that the sequence generated by this iteration gives quadratic convergence to the solution, P, of $F(X) = 0$, provided that the initial guess, X_0, is a sufficiently close approximation to the actual solution [*Burden and Faires*, 1989]. In order to satisfy this condition, we take advantage of the slow evolution of the LLBL downstream by using the values of all variables in the previous step as an initial guess for a new step in the downstream direction.

In practice, explicit computation of $1/J(X)$ is avoided by performing the operation in a two-step manner. First, a vector $Y \equiv X_k - X_{k-1}$ is found which satisfies

$$J(X_{k-1})Y = -F(X_{k-1}) \tag{90}$$

46

After this has been accomplished, the new approximation, X_k, is obtained by adding Y to X_{k-1}.

The vector X_k contains the solution $([u_1, v_1, B_1, \rho_1, p_1, ..., u_n, v_n, B_n, \rho_n, p_n, u_{n+1}]_k)^T$ after each iteration step, k. The vector $F(X)$ contains the left-hand side of the $(5 \times n) + 1$ finite difference equations described earlier. The Jacobian matrix $J(X)$ is of the form

$$J = \begin{bmatrix} \frac{\partial f_1}{\partial u_1} & \frac{\partial f_1}{\partial v_1} & \cdots & \frac{\partial f_1}{\partial u_{n+1}} \\ \frac{\partial f_2}{\partial u_1} & \frac{\partial f_2}{\partial v_1} & \cdots & \frac{\partial f_2}{\partial u_{n+1}} \\ \vdots & \vdots & \vdots & \vdots \\ \frac{\partial f_{5n+1}}{\partial u_1} & \frac{\partial f_{5n+1}}{\partial v_1} & \cdots & \frac{\partial f_{5n+1}}{\partial u_{n+1}} \end{bmatrix} \tag{91}$$

Since all of the finite difference equations involve the variables at no more than three neighboring grid points in the y direction, it is possible to arrange the above matrix in a banded form with bandwidth equal to 15. Notice from equation (89) that, at every step of the iteration procedure, after the initial guess, X_0, both $J(X_{k-1})$ and $F(X_{k-1})$ are known, and therefore, a linear algebraic system has to be solved for X_k. This is done by an IMSL (Mathematical and Statistical Library) Library subroutine, that performs LU decomposition of the above matrix and includes partial pivoting.

REFERENCES

Anderson, D.A., J.C. Tannehill, and R.H. Pletcher (Eds.), *Computational Fluid Mechanics and Heat Transfer*, p. 329, McGraw-Hill, New York, 1984.

Burden, R.L., and J.D. Faires, *Numerical Analysis*, p. 536, PSW-KENT, Boston, Mass., 1989.

Smith, G.D., *Numerical Methods for Partial Differential Equations: Finite Difference Methods*, p. 29, Oxford Applied Mathematics and Computing Science Series, Clarendon Press, Oxford, 1984.
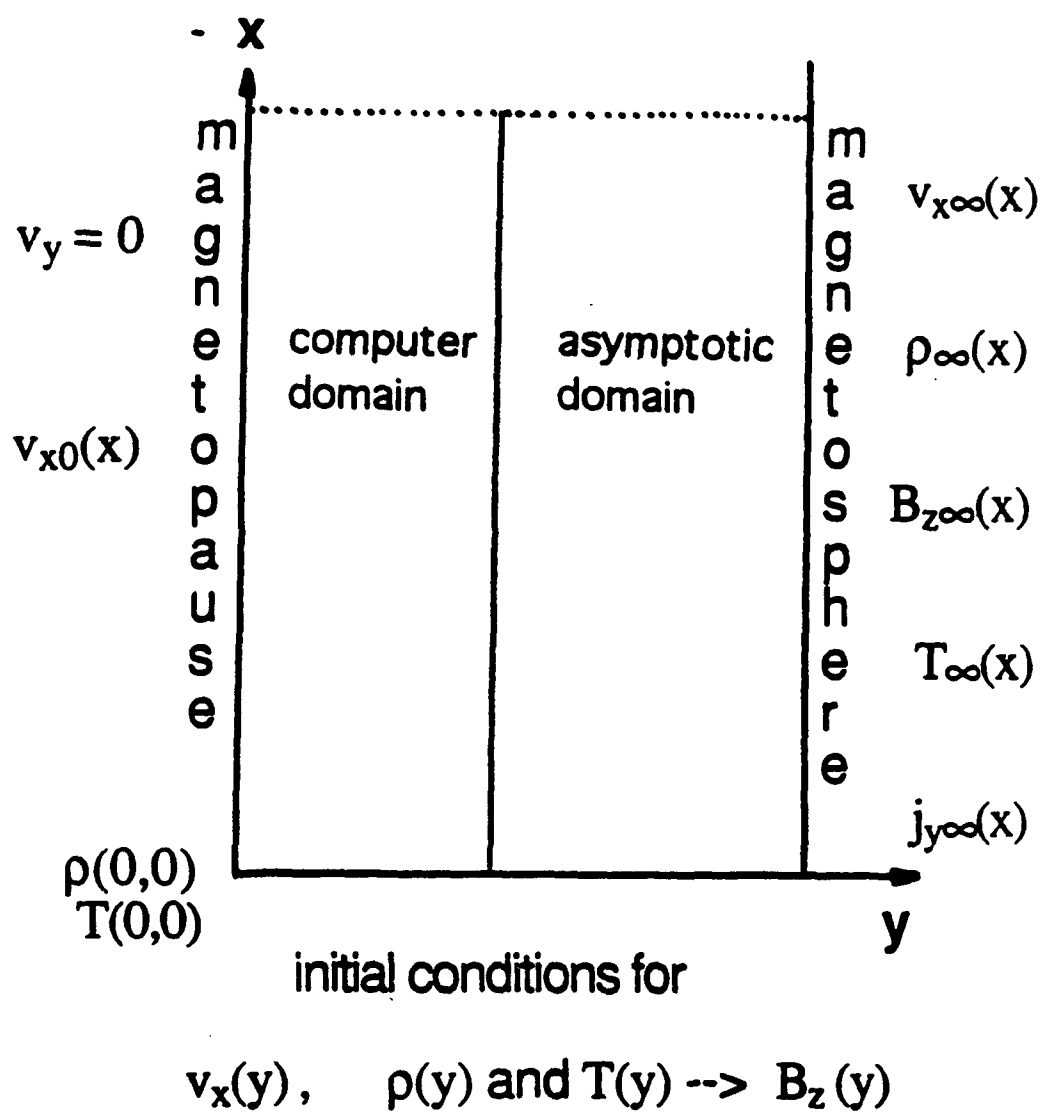
Fig. 7. A schematic of the computational domain and the asymptotic domain in the equatorial plane.

APPENDIX 4: BENCH MARK TESTS

The system of equations (15), (17), (18), (20) and (26) possesses certain self-similar solutions. In this Appendix, these solutions are derived and used as benchmarks for the numerical code described in Appendix 3.

We first examine the mass conservation law. The x and y components of the velocity, and the plasma density are assumed to have the following variation with x and y:

$$v_{x0} = x^m f(\eta), \quad v_{y0} = x^p g(\eta), \quad \rho_0 = x^q r(\eta), \quad \eta = \frac{y}{x^n} \tag{92}$$

Here, f, g, and r are functions of the independent variable η only, and m, p, q and n are exponents to be determined in such a way that all powers of x are cancelled in the system of equations mentioned above. A solution derived in this manner has the following property: one may obtain the solution at every x location from the solution at any other x location by (a) multiplying by x raised to the appropriate power and (b) rescaling the y axis so that the ratio y/x^n matches the similarity variable, η. By substituting (92) into the mass conservation law, equation (15), we get

$$(m + q)fr - n\eta(fr)' + (gr)' = 0 \tag{93}$$

The differentiation, denoted by the prime, is with respect to the only remaining independent variable, namely, η. The requirement that the powers of x cancel results in the following condition for the exponents:

$$m - 1 = p - n \tag{94}$$

To derive an ordinary differential equation from the x-momentum equation, we assume that the total pressure in the equatorial plane, $P_\infty(x)$, has the following

variation:

$$P_\infty(x) = x^{2m+q}C_p \tag{95}$$

where C_p is a constant, independent of both x and η. From the y-momentum equation, (17), it then follows that

$$p_0 = x^{2m+q}\pi(\eta), \quad B_{x0} = x^{m+q/2}b(\eta) \tag{96}$$

and the y-momentum equation takes the form

$$\pi + \frac{b^2}{2\mu_0} = C_p \tag{97}$$

Furthermore, we assume that the conductivity, σ, the current, j_y and the viscosity, η_0 have the following variation:

$$\sigma = x^\beta \Sigma(\eta), \quad j_y = x^s J(\eta), \quad \eta_0 = x^a M(\eta) \tag{98}$$

With the above assumptions, the x-momentum equation, (26), becomes

$$mrf^2 - n\eta rff' + rgf' = -(2m+q)C_p - \Sigma b^2 f$$
$$+ \left(\Sigma_\infty f_\infty b_\infty + J_\infty + \frac{1}{\mu_0}(m + \frac{q}{2})b_\infty \right) b + M'f' + Mf'' \tag{99}$$

The requirements on the exponents are:

$$2m + q - 1 = 3m + q + \beta = s + m + q/2 = a - 2n + m \tag{100}$$

from which we get

$$\beta = -1 - m, \quad s = m + \frac{q}{2} - 1, \quad a = m + 2n + q - 1 \tag{101}$$

Similarly, the isentropic law, equation (18), becomes

$$(2m + q - \gamma q)f\frac{\pi}{r^\gamma} - n\eta f\left(\frac{\pi}{r^\gamma}\right)' + g\left(\frac{\pi}{r^\gamma}\right)' = 0 \tag{102}$$

and the induction law, equation (20), becomes

$$(m - \frac{q}{2})f\frac{b}{r} - n\eta f \left(\frac{b}{r}\right)' + g \left(\frac{b}{r}\right)' = 0 \tag{103}$$

No further restrictions on the exponents are imposed by the latter two equations.

The system (93), (97), (99), (102), and (103) consists of five ordinary differential equations for f, g, r, π and b, with respect to the only independent variable, η; it can be integrated subject to five boundary conditions (one equation is of second order and one is algebraic). It contains seven exponents, namely, m, n, p, q, β, s and a, which are constrained by the four conditions (94) and (101), so that three exponents can be specified.

If the total pressure in the magnetosphere is a function of x, the x variation of ρ_0, p_0 and B_{x0} is given by (92) and (96). The solution that was used for benchmarking of the numerical code in the computational box is of this form. The exponents were chosen as follows: n was chosen to be zero, which represents a "constant thickness" boundary layer; in this case $\eta = y$ and no scaling in the y direction is needed in order to relate the solutions at different x locations; m was chosen equal to 1, and q was chosen equal to 2 so that the magnetopause boundary is a stream line with $g(0) = 0$. With $n = 0$, $m = 1$, and $q = 2$ it follows from (94) and (101) that $p = 0$, $\beta = -2$, $s = 1$, and $a = 2$. One can see that with those parameters, equations (97), (102), and (103) require solutions for π, r, and b that are independent of η. The five variables then take the form

$$v_{x0} = xf(y), \quad v_{y0} = g(y), \quad \rho_0 = x^2 C_r, \quad p_0 = x^4 C_\pi \quad B_{x0} = x^2 C_b \tag{104}$$

Notice from (98) that the conductivity, the current flowing into the magnetosphere, and the viscosity are functions of x. The viscosity function, M, was chosen to be independent of y. The resulting system of equations was solved subject to the following

52

boundary conditions: $f(0) = -180$ km/sec, $f(\infty) = 0$, $g(0) = 0$, $B_{x0}(0,y) = 44$ nT, and $p_0(0,y) = 0.62$ nPa.

The solution was obtained by integrating (93) and (99); an IMSL (Mathematical and Statistical Library) Ordinary Differential Equation solver routine was used for that purpose. This solution was then used as the initial step in the code described in Appendix 3, at $x = -10\ R_E$. Boundary conditions and other parameters were chosen according to the requirements for the self-similar solution described above. Figure 8 shows the profiles, obtained by the numerical code, of v_{x0}, v_{y0}, B_{x0}, p_0, and ρ_0, versus y in the computational box, at two different x locations, namely, after $3\ R_E$ and after $6\ R_E$ from the beginning of the calculation. At each location, the profile from the independent integration of the ODE's, scaled to the appropriate x location is superimposed. The difference between the two solutions is of the order of one part in 10^4 and is indistinguishable in the plots.

It should be noted that this case is not a complete benchmark of the code because ρ_0, p_0 and B_{x0} were chosen to be functions of x only: those variables are constant with y. However, it can be argued that this is not a major restriction because (a) the pressure balance in the y direction, which is explicitly incorporated in the code, is accurately satisfied at every step in the $-x$ direction, and (b) the validity of the finite difference form for the convective terms in the induction law (the isentropic law is expressed similarly), when B_{x0} is non-constant with y, has been verified separately.

It is emphasized that in this benchmark test, an explicit boundary condition on the value of v_{x0} at the magnetospheric boundary was used in the numerical code, instead of the mixed boundary condition derived by matching the solution at the computational box with an asymptotic solution that extends into the magnetosphere. This serves the purpose of verifying the finite difference representation of the equations

53

described in Appendix 3. It was found that, when a computational solution is matched to an asymptotic solution at $y = y_b$, the overall accuracy of the code is somehow influenced by the choice of the boundary condition applied at $y = y_b$. The method we chose was to require a solution that would guarantee continuous first and second derivatives of the velocity component v_{x0} at $y = y_b$ (in addition to continuity of v_{x0} itself), so that the first derivative of the current at the top of the boundary layer is also continuous, as explained in Appendix 1. The boundary condition that was implemented is given by equation (33) and the solution in the asymptotic box is given by (29), where $a(x)$ has been slightly adjusted from the value given by (30) to allow for a continuous second derivative of v_{x0}. For the benchmark test of the entire code, including the asymptotic box, a self-similar solution with constant total pressure along the equatorial LLBL was chosen, as described below.

If the total pressure in the magnetosphere, P_∞, is assumed to be independent of x, then the density, the plasma pressure, and the z component of the magnetic field should also be independent of both x and y in order to satisfy equations (17), (18), and (20). The mass conservation law, which is then of the form $\nabla \cdot v = 0$, i.e., it represents an incompressible solution, becomes

$$mf - n\eta f' + g' = 0 \tag{105}$$

and the x-momentum equation becomes

$$C_r(mf^2 - n\eta ff' + gf') = -\Sigma C_b^2 f + (\Sigma_\infty f_\infty C_b + J_\infty)C_b + M'f' + Mf'' \tag{106}$$

Here, C_r and C_b denote the constant values of ρ_0 and B_{x0}. The relation (94) for the exponents is still valid and the relation (100) becomes

$$2m - 1 = m + \beta = s = a - 2n + m \tag{107}$$

54

The solution of (105) and (106) that was used for benchmarking has an asymptotic behavior as $y \to \infty$ such that $j_{y\infty} = 0$, $v_{x\infty} = 0$. Also, the values m=1, n=0 were used. Under those assumptions the solution to (105) and (106) can be found analytically; it is given by

$$f = Ae^{-cy}, \quad g = \frac{A}{c}(e^{-cy} - 1) \tag{108}$$

where A is given by the boundary condition on f at $y = 0$ and c satisfies the relation

$$A = \Sigma \frac{C_b^2}{C_r} + \frac{M}{C_r}c^2 \tag{109}$$

Figure 9 shows the profiles of v_{x0} and v_{y0} versus y, at a distance of 10 R_E downstream from the beginning of the calculation. The computational box ends at the location where $v_{x0} = -3$ km/s. As in Figure 8, two profiles have been superimposed, one from the numerical code and the other from the independent ODE calculation. The difference between the two results is of the order of one part in 10^2.

4.1 Self-Similar Solutions of the Extended Model

The extended model described in Appendix 2, that includes field-aligned potential drops in the coupling region, possesses self-similar solutions as well.

In the following, v_{x0}, v_{y0}, B_{x0}, ρ_0, p_0, and η_0 are assumed to have the functional behavior described earlier in this Appendix. Furthermore,

$$B_{x1} = x^e d(\eta), \quad j_{\parallel_i} = x^c J_\parallel(\eta), \quad B_i = x^{b_i} B_i(\eta), \quad \frac{dx_i}{dx} = x^{x_i} dx(\eta),$$

$$\Sigma_p = x^\sigma \Sigma(\eta), \quad H_0 = x^h H_\eta(\eta), \quad B_{y1} = x^t b_y(\eta), \quad v_{z1} = x^v z(\eta) \tag{110}$$

With the above assumptions the x-momentum equation, (16), becomes

$$mrf^2 - n\eta rff' + rgf' = -(2m + q)C_p + \frac{1}{H\mu_0}bd + M'f' + Mf'' \tag{111}$$

55

where the requirements on the exponents are

$$2m + q - 1 = m + \frac{q}{2} + e = m - 2n + a \tag{112}$$

The y-momentum equation remains as in (97), and the isentropic law remains as in (102). The requirements on the exponents from this law are again

$$m - 1 = p - n \tag{113}$$

The induction law, equation (19), becomes

$$(2m + \frac{q}{2})bf - n\eta(bf)' + (bg)' = 0 \tag{114}$$

while equation (67) becomes

$$J_{\parallel} = \Sigma\left(\frac{B_i}{b}dx\right)^2\left(\frac{1}{\kappa}J_{\parallel}'' + (fb)'\right) + \frac{B_i}{b}dx\left(\Sigma\frac{B_i}{b}dx\right)'\left(\frac{1}{\kappa}J_{\parallel}' + fb\right) \tag{115}$$

The requirements on the exponents are

$$\sigma + 2b_1 + 2x_1 = 2m + 2n + q, \quad c = 2m + n + q/2 \tag{116}$$

The current continuity, equation (63), becomes

$$\frac{1}{\mu_0 H}(dH_\eta)' = -\frac{J_{\parallel}b}{B_i} \tag{117}$$

along with with the requirement

$$h - n + e = c - b_1 + m + q/2 \tag{118}$$

The mass conservation law, equation (47), gives

$$(q + h + m)rH_\eta f - (n\eta - 1)(rH_\eta f)' = 0 \tag{119}$$

and the z-momentum equation, (50), becomes

$$2\mu_0(\pi_\infty - \pi) = (d\frac{H_\eta}{H})^2 \tag{120}$$

56

along with the requirement

$$e + h = m + q/2 \tag{121}$$

Equation (46) becomes

$$-f(hH_\eta - n\eta H'_\eta) - gH'_\eta + \frac{zH_\eta}{H} = 0 \tag{122}$$

along with the requirement

$$m - 1 = p - n = v. \tag{123}$$

Finally, the magnetic flux conservation law, equation (52), becomes

$$ed - n\eta d' + b'_y = 0 \tag{124}$$

along with the requirement

$$t - n = e - 1. \tag{125}$$

The algebraic system (112), (113), (116), (118), (121), (123), and (125) gives

$$e = m + q/2 - 1$$

$$a = m + 2n + q - 1$$

$$p = m + n - 1$$

$$c = 2m + n + q/2$$

$$b_1 = 2m + 2n + q/2$$

$$h = 1$$

$$\sigma + 2x_1 = -2m - 2n$$

$$v = m - 1$$

$$t = 2m + q/2 - 2 \tag{126}$$

The above nine relations constrain the thirteen parameters that are present in the system of ordinary differential equations derived in this section. Four of those parameters are free, and one, namely h, is required to have a fixed value. Note that this results in a somewhat unphysical variation with x of the height H_0; nevertheless, the solution can be used for the purpose of benchmarking.

4.2 Other Benchmarks

As already mentioned in Appendix 1, the system has been benchmarked against the one-dimensional solution (which is independent of x) derived by *Sonnerup* [1980], under the appropriate assumptions. First, the solution, which is given by equation (42), was used as an upstream velocity profile: it was found to remain unchanged, for as long a distance downstream as desired. Second, a different initial profile was imposed and it was found that, with increasing $|x|$, the system eventually relaxed to Sonnerup's solution, with $v_y \equiv 0$, as required.

REFERENCES

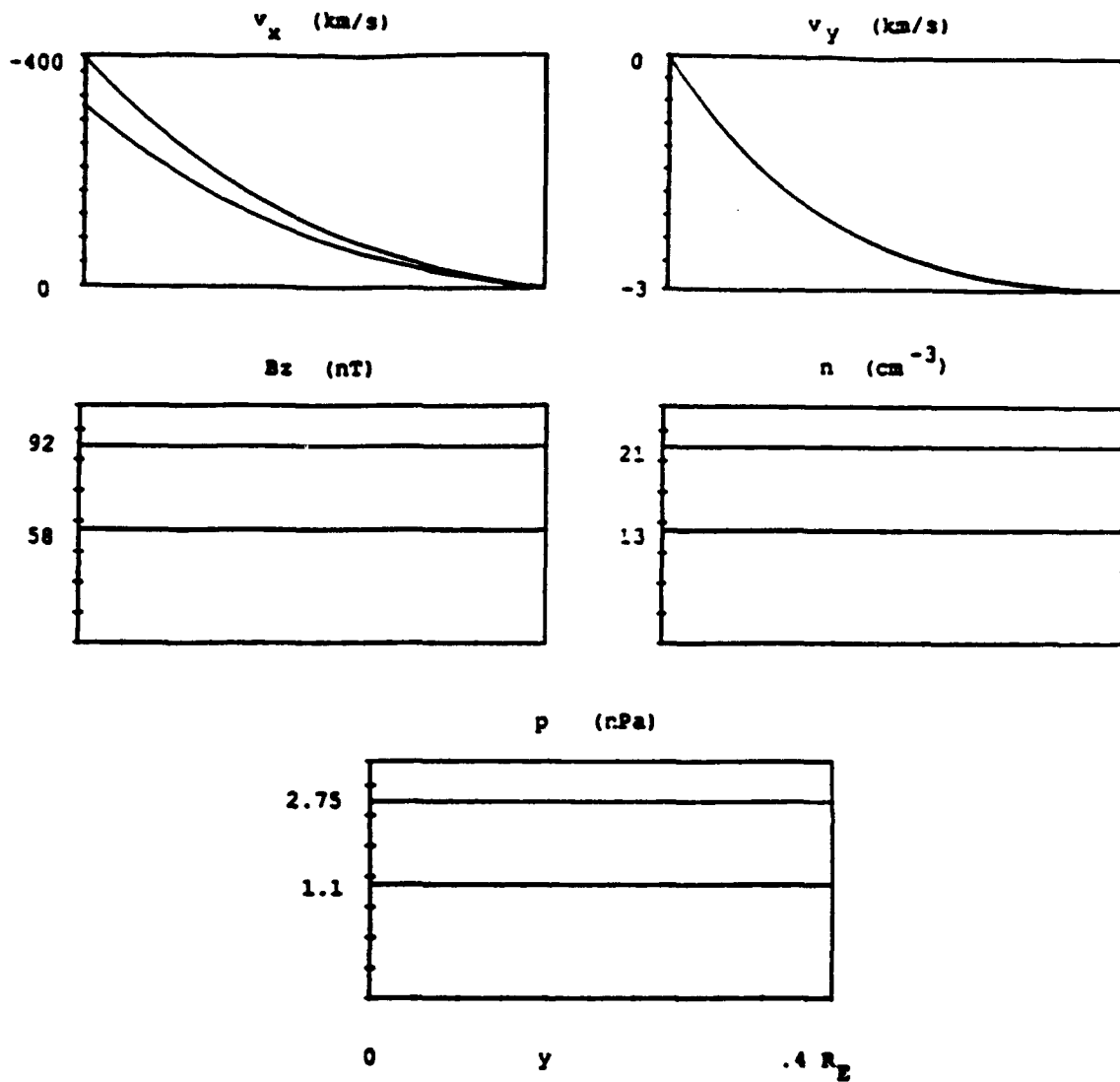Sonnerup, B.U.Ö., Theory of the low-latitude boundary layer, *J. Geophys. Res.*, *85*, 2017, 1980.

Fig. 8. Self-similar benchmark solution: plotted are profiles of v_{x0}, v_{y0} (top two panels), ρ_0, B_{x0} (middle two panels), and p_0 (bottom panel), versus y, after a flow distance of 3 R_E and 6 R_E from the upstream location. Each profile is calculated from the numerical code and from an ODE solver independently, and the two solutions are superimposed.
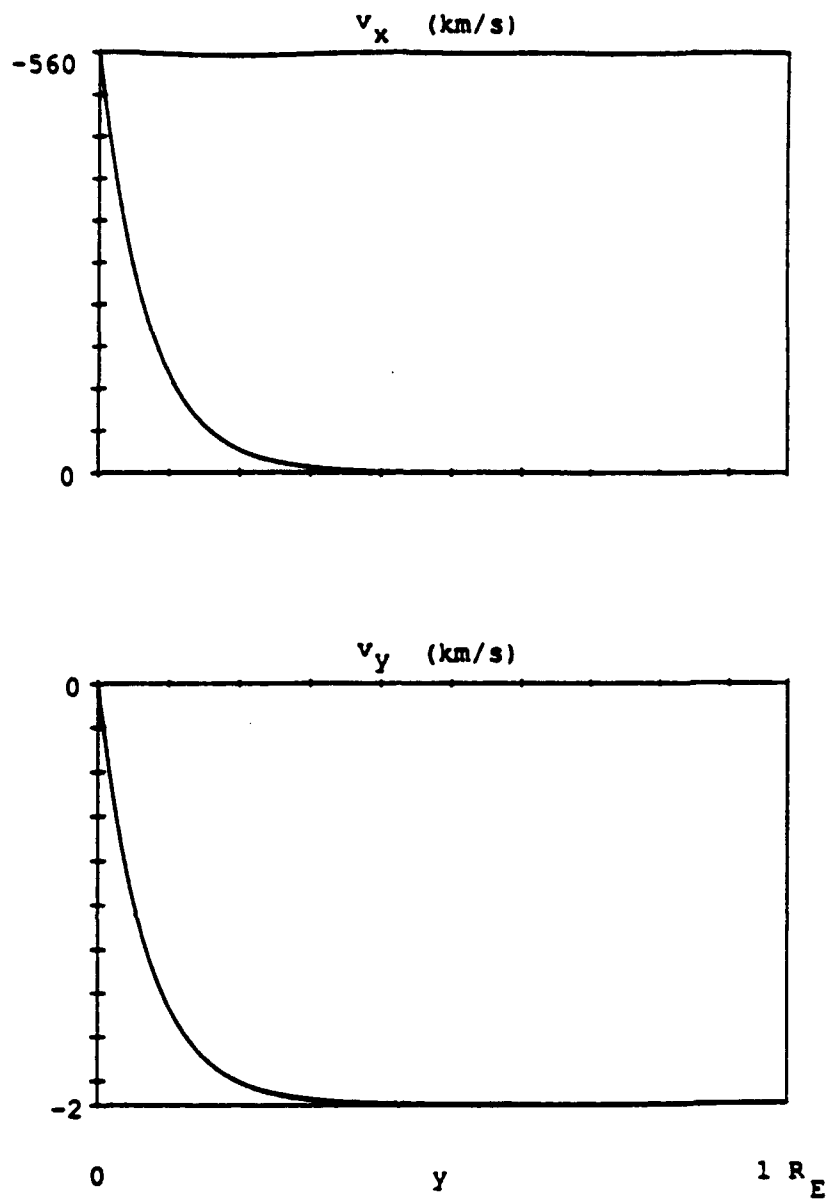
Fig. 9. Incompressible self-similar solution. The two panels show the profiles of v_{x0} and v_{y0}, respectively, versus y, at flow distance of 10 R_E from the beginning of the calculation; B_{x0}, ρ_0, and p_0 are constant. The solutions given by the numerical code and by independent integration of the ODE are superimposed. The computational box ends at 0.3 R_E, and an asymptotic solution is pasted to the computational solution at that location.

Force-Free Boundary Layer Model for Mapping Field-Aligned Currents

K. Vatan[1], W. Lotko, and B. U. O, Sonnerup

Thayer School of Engineering, Dartmouth College, Hanover, NH

ABSTRACT

A mathematical model for a force-free boundary layer (FFBL) has been developed to calculate the deflection of the earth's magnetic field due to quasi-steady field-aligned currents. The model may be used to determine the magnetic field structure and mapping between the equatorial magnetosphere and the ionosphere. The geometrical volume of interest extends between two magnetic flux surfaces, with a low altitude boundary representing the ionosphere and a high altitude boundary representing the interface with a model for field-aligned current generation. The mathematical formulation is general and may be implemented numerically for any magnetic geometry for which locally orthogonal coordinates can be defined. A numerical implementation of the model and its application to dayside region 1 currents are described. The illustrative application in dipole magnetic geometry suggests that typically observed dayside region 1 currents produce a maximum (upper limit) azimuthal deflection of dipole field lines of about 26°.

---

[1] Now at Hewlett-Packard Company, Workstation Division, Chelmsford, Massachusetts.

1. INTRODUCTION

The description of magnetic field-aligned currents (FAC) presents a difficult problem to the magnetospheric modeler because the closure paths of the currents are determined fundamentally by the local plasma and fluid behavior. In the framework of one-fluid magnetohydrodynamics (MHD), FAC closure can be effected by plasma polarization (finite inertia), plasma diamagnetism (finite thermal energy), and plasma electrical conductivity (finite collision time). The last effect dominates in the ionosphere while the first two are important in the equatorial magnetosphere. In the intermediate altitude region, between the ionosphere and the equatorial magnetosphere, the transverse elements of the plasma conductivity tensor, the ratio of plasma pressure to magnetic pressure, and the Alfvén Mach number are all small. Therefore, the electrical currents that flow in the intermediate altitude region are force-free to a good approximation and remain field-aligned until reaching the ionosphere or the equatorial magnetospheric region where they are diverted into perpendicular currents.

The purpose of this paper is to describe a new technique for calculating quasi-steady field-aligned currents in the intermediate altitude region, and the magnetic deflections produced by them, when the currents flow in a relatively thin, but finite thickness, layer. *Stern* [1993] has recently described a technique for calculating the perturbing effects of field-aligned currents on the magnetic field in regions outside the field-aligned current layer, i.e., in regions where the field-aligned current is zero. The magnetic field is evaluated by *Stern* assuming that the FAC flows along the unperturbed magnetic field lines in a zero thickness (δ-function) sheet or shell. When the current layer has a finite thickness, the FAC must flow along magnetic field lines that are determined by solving for the FAC path and the magnetic field lines simultaneously. Therefore, the model described in this paper effectively resolves the δ-function sheet currents assumed by *Stern*. Because the currents are assumed to be entirely field-aligned in the thin layer of interest here, we refer to the model as a force-free boundary layer (FFBL).

The utility of the FFBL model described here is twofold. It can be used to map FACs outward from the ionosphere where statistical synoptic data on their spatial distributions are available. The model may also be used, in modular form, to connect a high altitude magnetospheric dynamo region to its ionospheric load. For example, we envision (though have not yet accomplished) connecting the FFBL model with the low-latitude boundary layer model developed recently by *Drakou et al.* [1994]. Other applications for connection to nightside or cusp region dynamos are also possible.

In this brief report, the basic assumptions and mathematical formulation of the FFBL model are described, along with a particular numerical implementation. Use of the basic technique is illustrated by mapping the dayside region 1 currents [*Iijima and Potemra*, 1976] outward from the ionosphere in an (oversimplified) approximation where the magnetic field outside the FFBL remains dipolar.

For reference, the field outside the FFBL is identified in this paper as the *exterior field*. The exterior field occupies regions that are both closer to and further from earth than the FFBL. We assume throughout the paper that a locally orthogonal, 'magnetic' coordinate system exists, in which one of the coordinates lies along the exterior magnetic field, a second is normal to the FFBL surface (also a magnetic flux surface), and the third completes the orthogonal set. In fact, one can always identify a system of locally orthogonal unit vectors at any point on a magnetic flux surface (e.g., the Frenet-Serret set or the LMN set often used in

magnetopause studies) for the purposes of resolving field vectors into locally orthogonal components and performing vector algebra on them. However, representation of vector differential operators requires specification of the transformation equations that relate appropriate magnetic flux coordinates to Cartesian coordinates and which determine the metric tensor for the transformation. Transformations that remain locally orthogonal in the magnetic flux coordinates are known to exist for plane fields and axisymmetric fields, of which the dipole field is a familiar example, but locally orthogonal transformations can be difficult, if not impossible, to find for realistic magnetic field configurations. As a consequence, we are currently in the process of generalizing the FFBL formulation described here and expect in a future paper to report on a FFBL model based on non-axisymmetric, non-orthogonal magnetic flux coordinates.

2. MODEL

2.1 Force-Free Condition

In the region of interest, the ratio of plasma pressure to magnetic pressure, is assumed to be much smaller than one, as is the ratio of plasma kinetic energy density to magnetic pressure. Therefore the Lorentz force term dominates the pressure gradient and inertial terms in the MHD equation of motion. The momentum equation then reduces to the so-called force-free condition [e.g., Priest, 1982] in terms of the plasma current density j and the magnetic field B:

$$j \times B = 0. \tag{1}$$

From the steady-state Ampere's law,

$$\mu_0 j = \nabla \times B \tag{2}$$

where μ_0 is the permeability of free-space. The force-free condition can be alternatively expressed as

$$\mu_0 j = \alpha B \tag{3}$$

where $\alpha(r)$ is a scalar function of the spatial coordinates. Combining (2) and (3) gives

$$\nabla \times B = \alpha B. \tag{4}$$

The divergence of (4), together with $\nabla \cdot B = 0$, shows that $\alpha(r)$ is constant along magnetic field lines:

$$B \cdot \nabla \alpha = 0. \tag{5}$$

2.2 Geometrical Domain

After implementing the approximations described in Section 2.3 below, a solution to (4) and (5) will be developed in a general curvilinear coordinate system with the proviso that the coordinates be locally orthogonal. The curvilinear coordinates are as follows: x_1 is the generalized 'azimuthal' coordinate; x_2 is the flux surface label and decreases in value when going

63

from inner flus surfaces to outer flus surfaces; x_3 varies along the exterior magnetic field. The unit vectors $\hat{x}_1$, $\hat{x}_2$ and $\hat{x}_3$ form a mutually orthogonal set. As mentioned above, the term 'exterior' is used to indicate the magnetic field outside and at the edge of the FFBL where the FAC is zero. In general, the exterior field is also influenced by the force-free current; these effects can be modeled in the region outside the force-free boundary magnetic by calculating the magnetic field perturbations produced by a zero thickness, force-free current sheet (or shell), i.e., a δ-function current sheet. This current sheet can then be resolved into a finite width, force-free current layer using the procedures described below. The geometrical region of interest is therefore a thin, but finite thickness layer where the force-free current is nonzero.

This geometrical volume is illustrated in Figure 1. It extends between two magnetic flux surfaces (to which the exterior field is everywhere tangential), with a low altitude boundary representing the ionosphere and a high altitude boundary representing the interface with a model for field-aligned current diversion or generation in the magnetosphere. The inner and outer magnetic shells correspond, respectively, to the maximum and minimum values of the coordinate x_2. For applications of the model to portions of the dayside magnetospheric boundary layer region on closed field lines, the outer magnetic shell might be taken as the magnetopause surface and its projection along field lines from the equatorial plane to the ionosphere. Although the numerical calculations described later in this paper are based on dipole magnetic geometry, the mathematical formulation is general and may be implemented numerically for any magnetic geometry for which locally orthogonal coordinates can be defined.

2.3 Boundary Layer Approximation

The method of solution to (4) and (5) makes use of a narrow-channel or boundary-layer approximation for which spatial changes across the thin layer in the x_2 direction occur on a scale length δ that is much less than the scale length L for changes in the x_1 direction or the scale length H in the x_3 direction. The x_1 and x_3 coordinates vary on surfaces that are tangential to the thin layer. The boundary layer approximation implies that

$$\partial/\partial x_1 \sim 1/L, \qquad \partial/\partial x_2 \sim 1/\delta, \qquad \partial/\partial x_3 \sim 1/H \tag{6}$$

where $\delta \ll L \sim H$. Assigning a characteristic value B_0 for the field components B_1 and B_3 in the $\hat{x}_1$ and $\hat{x}_3$ directions, the solenoidal condition $\nabla \cdot \mathbf{B} = 0$ implies the following scaling relations:

$$B_1 \sim B_3 \sim B_0; \qquad B_2 \sim \frac{\delta}{L} B_0 \ll B_0. \tag{7}$$

B_2 is the component of $\mathbf{B}$ in the x_2 direction.

Expressing the curl in Ampere's law in a locally orthogonal coordinate system with metric scale factors, $h_i = |\partial \mathbf{r}/\partial x_i|$, provides the following three equations:

$$j_1 = \frac{1}{\mu_0 h_2 h_3} \left[\frac{\partial(h_3 B_3)}{\partial x_2} - \frac{\partial(h_2 B_2)}{\partial x_3} \right] \tag{8}$$

$$j_2 = \frac{1}{\mu_0 h_1 h_3} \left[\frac{\partial(h_1 B_1)}{\partial x_3} - \frac{\partial(h_3 B_3)}{\partial x_1} \right] \tag{9}$$

$$j_3 = \frac{1}{\mu_0 h_1 h_2} \left[\frac{\partial(h_2 B_2)}{\partial x_1} - \frac{\partial(h_1 B_1)}{\partial x_2} \right]. \tag{10}$$

Using the boundary layer scaling relations defined by (6) and (7), and neglecting terms of $O(\delta^2/L^2)$ in Ampere's law, equations (8) and (10) become:

$$j_1 \approx \frac{1}{\mu_0 h_2 h_3} \frac{\partial(h_3 B_3)}{\partial x_2}, \tag{11}$$

$$j_3 \approx \frac{1}{\mu_0 h_1 h_2} \frac{\partial(h_1 B_1)}{\partial x_2}. \tag{12}$$

Comparison of the second equation (9) of Ampere's law with first (8) and third (10) equations shows that

$$\frac{j_2}{j_1} \sim \frac{j_2}{j_3} \sim \frac{\delta}{L} \ll 1. \tag{13}$$

The current flow normal to the boundary layer is therefore small.

Combining (11) and (12), and using the force-free condition, $\mu_0 \mathbf{j} = \alpha \mathbf{B}$, yields the following equation for B_3:

$$\frac{1}{h_1 h_2 \alpha} \frac{\partial}{\partial x_2} \left[\frac{h_1}{h_2 h_3 \alpha} \frac{\partial(h_3 B_3)}{\partial x_2} \right] + B_3 = 0. \tag{14}$$

An analogous equation can be derived for B_1. We now further assume the layer is sufficiently thin so that the metric scale factors h_1 and h_3 are very nearly constant on the scale size for variations in $\mathbf{B}$ across the layer: $|\partial_2 \ln h_{1,3}| \ll |\partial_2 \ln B_{1,3}|$. With this approximation (14) becomes

$$\frac{1}{\alpha h_2} \frac{\partial}{\partial x_2} \left[\frac{1}{\alpha h_2} \frac{\partial B_3}{\partial x_2} \right] + B_3 = 0 \tag{15}$$

2.4 Boundary Layer Solution

To solve (15) a new variable, $d\tau = \alpha h_2 dx_2$, is defined. Equation (15) then becomes

$$\partial_\tau^2 B_3(\tau) + B_3(\tau) = 0, \tag{16}$$

and B_1 is determined from its solution as

$$B_1(\tau) = \frac{\partial B_3(\tau)}{\partial \tau}. \tag{17}$$

The general solution, with explicit dependence on x_1, x_2, and x_3 retained, is

$$B_1 = B_\infty(x_1, x_3) \cos[\psi(x_1, x_3) + \tau(x_1, x_2, x_3)] \tag{18}$$

$$B_3 = B_\infty(x_1, x_3) \sin[\psi(x_1, x_3) + \tau(x_1, x_2, x_3)] \tag{19}$$

where

$$B_\infty(x_1, x_3) = \sqrt{B_1^2(x_1, x_{2\infty}, x_3) + B_3^2(x_1, x_{2\infty}, x_3)} \tag{20}$$

$$\psi(x_1, x_3) = \arctan[B_3(x_1, x_{2\infty}, x_3)/B_1(x_1, x_{2\infty}, x_3)] \tag{21}$$

$$\tau(x_1, x_2, x_3) = \int_{x_2}^{x_{2\infty}} \alpha(x_1, x_2', x_3) h_2(x_1, x_2', x_3) dx_2' \tag{22}$$

65

The constants of integration, B_∞ and ψ, are determined by boundary conditions on B_1 and B_3 on a reference flux surface identified as $x_2 = x_{2\infty}$. The x_2' dependence in the metric scale factor h_2 appearing inside the integral in (22) has been formally retained, although no accuracy is actually gained by including this dependence. The approximation used in going from equation (14) to (15), in fact, allows one to treat h_2 as constant across the layer so that it is equally correct to set $h_2(x_1, x_2', x_3) \approx h_2(x_1, x_{2\infty}, x_3)$ in (22) and to take h_2 outside the integral.

B_2 is obtained by substituting B_1 and B_3 from (18)-(22) in $\nabla \cdot \mathbf{B} = 0$. After integration with respect to x_2, and using $B_2(x_1, x_{2\infty}, x_3) = 0$, which must be true if $x_2 = x_{2\infty}$ is a flux surface, we find

$$B_2 = \frac{1}{h_1 h_3} \int_{x_2}^{x_{2\infty}} \left[\frac{\partial(h_2 h_3 B_1)}{\partial x_1} + \frac{\partial(h_1 h_2 B_3)}{\partial x_3} \right] dx_2' \tag{23}$$

Note that the metric scale factors may vary as rapidly (or slowly) as $\mathbf{B}$ in the $\mathbf{\hat{x}}_1$ and $\mathbf{\hat{x}}_3$ directions, so they may not be passed through the derivatives in the integrand in (23). It is also noted that $h_{1,2,3}$ are in general functions of x_1, x_2, and x_3. However, as discussed above, we gain no accuracy in retaining the x_2 dependence in the scale factors; they may be evaluated at $x_2' = x_{2\infty}$ and treated as constants in performing the integration over x_2'. The distribution of $\alpha(x_1, x_2, x_3)$ throughout the spatial region of interest is not known a priori except on some bounding surface, say $x_3 = x_3^{(0)}$ where $x_3^{(0)}$ is a constant value of the coordinate x_3. The volume distribution of α can be determined self-consistently along with the magnetic field by simultaneously solving (5) and (18)-(23).

2.5 Boundary Conditions

The formulation of the force-free boundary layer model given above is general and may be used when (i) the region of interest can be characterized by the force-free condition (1) and (ii) the field-aligned current into the region flows in a thin layer so that the boundary layer approximations (6) and (7) are appropriate. Given these constraints, a unique solution to the set of equations (5) and (18)-(23) requires two boundary conditions:

(A) specification of the magnetic field $\mathbf{B}(x_1, x_{2\infty}, x_3)$ on a reference magnetic flux surface $x_2 = x_{2\infty}$, and

(B) specification of $\alpha(x_1, x_2, x_3^{(0)}) = \mu_0 j / B$ on a bounding surface, $x_3 = x_3^{(0)}$, normal to the magnetic field (a 'magnetic normal surface').

Technically, a unique solution also requires specifying the partial derivative $\partial(h_1 h_2 B_3) / \partial x_3$ in (23) on the bounding surface $x_3 = x_3^{(0)}$. We have found in practice, however, that the value of this derivative on the bounding surface has little influence on the accuracy of the boundary layer solution (cf. discussion in Sec. 2.6).

For applications to the magnetosphere, we will take the reference magnetic flux surface to be located at the inner edge of the force-free boundary layer. In dipole coordinates, this surface would correspond to the innermost L-shell of the FFBL. While the magnetic field earthward of the reference flux surface is presumed to be known, this internal field, in general, depends on the currents that flow in the FFBL. Because the FFBL is a thin layer, its influence on the internal field could be calculated, approximately, in the limit where the FFBL

66

is represented as a zero thickness (δ-function) shell. An internal field model, including the perturbing magnetic field due field-aligned currents, approximated as δ-function current sheets, has been discussed by *Stern* [1993]. The internal field, calculated in this way, then provides boundary condition (A) stated above; the δ-function, field-aligned current shell can be resolved using the FFBL formulation. If better accuracy is desired, an iterative process must be used. In the illustrative application described in Sec. 4, we do not attempt to construct a fully self-consistent magnetic field model. Instead the basic procedure for obtaining FFBL solutions is illustrated using the familiar dipole field model to specify boundary condition (A) and to represent the locally orthogonal curvilinear coordinate system required in the formulation.

Specification of boundary condition (B) requires either a model for the generation of the field-aligned currents or synoptic observations of the perturbed and background magnetic field on a magnetic 'normal' surface, on which **j**, **B**, and therefore α can be inferred. Synoptic observations of the currents are available only at low altitudes, essentially within the ionosphere. For the latter case, the FFBL model, coupled with an appropriate internal magnetic field model, can be used to follow the observed low altitude currents to their points of origin in the outer magnetosphere. Alternatively, coupling the FFBL model to a model for current generation, for example, the low-latitude boundary layer and region 1 current generation model developed by *Drakou et al.* [1994], would provide a means of locating the ionospheric signatures of the magnetospheric current generator.

2.6 Numerical Algorithm

The numerical algorithm used in our calculations assumes that the mapping between locally orthogonal curvilinear coordinates (x_1, x_2, x_3) and a geometrical coordinate system, for example, Cartesian (x, y, z) or spherical polar (r, θ, ϕ) coordinates, is known. In addition, the metric scale factors h_1, h_2, h_3 for the curvilinear system are assumed to be known. The boundary conditions stated above must also be supplied. Although the surfaces on which the boundary conditions apply may be quite complicated in the physical/geometrical domain, these surfaces are simple planes in the rectangular computational domain spanned by the three curvilinear coordinates. The algorithm solves for $\alpha(x_1, x_2, x_3)$ and $\mathbf{B}(x_1, x_2, x_3)$ throughout the three-dimensional FFBL on successive computational planes, $x_3 = x_3^{(k)}$, where $k = 0, 1, 2, \ldots$. Special measures must be taken to start the algorithm on the first plane.

On the first plane, where $\alpha(x_1, x_2, x_3^{(0)})$ is known from boundary condition (B), we use (18)-(22) to calculate B_1 and B_3 at grid points $(x_1^{(i)}, x_2^{(j)})$ where (i, j) are integers corresponding to grid locations for coordinates x_1 and x_2, respectively. To calculate B_2 we need to evaluate the partial derivatives and integral in (23). Initially, however, we have no information on the variation of **B** in the x_3 direction, which is required to perform the derivative $\partial(h_1 h_2 B_3)/\partial x_3$. To start the algorithm, we simply set $B_2 = 0$ on the starting plane. Because $B_{1,3} \gg B_2$ in the boundary layer approximation, the particular choice for B_2 on the first plane does not significantly influence the magnetic field mapping; we have found from experience with other starting procedures that the accuracy of the resulting magnetic field mapping differs from the one used here by terms of the order of those neglected in the boundary layer approximation.

Our particular numerical method for the rest of the domain proceeds as follows:

- Using (22), the metric scale factor h_2, and the trapezoidal rule of integration, $\tau(x_1, x_2, x_3^{(k)})$ is calculated at every grid point on the current x_3 plane, i.e. the $x_3 = x_3^{(k)}$ plane. Using (18)-(22), B_1 and B_3, are then calculated at these grid points.

- To calculate the B_2 component, we first calculate $\partial(h_2 h_3 B_1)/\partial x_1$ using central differencing and $\partial(h_1 h_2 B_3)/\partial x_3$ using forward differencing. Then using the trapezoidal rule, we integrate (23) to obtain B_2 at grid points on the $x_3^{(k)}$ plane.

- The next plane, the $x_3 = x_3^{(k+1)}$ plane, is chosen so that the linear projection along **B** from any node in the $x_3^{(k)}$ plane to a point in the $x_3^{(k+1)}$ plane stays within a small pre-specified distance ε of the node in the current $x_3^{(k)}$ plane.

- Using the property of force-free field lines, i.e. α is constant along the field lines, we can now determine values of α at non-grid locations in the $x_3 = x_3^{(k+1)}$ plane by following the linearly projected field lines from nodes in the $x_3 = x_3(k)$ plane. We now interpolate these now nonuniformly spaced values of α onto $(x_1^{(i)}, x_2^{(j)})$ grid points in the $x_3^{(k+1)}$ plane. To do this, α is first interpolated onto an x_2 line using a simple 2 point interpolation. Then a cubic spline interpolation scheme is used to interpolate α onto the grid points.

- Having calculated α on all grid points, the procedure is repeated until the final x_3 surface of interest is reached.

2.7 Numerical Accuracy

The accuracy of the numerical model was tested using a benchmark based on a simple analytical model of polar line currents feeding an axisymmetric, δ-function current sheet lying on a magnetic dipole L-shell [Vatan, 1993]. Because the polar line currents are chosen to flow into the south pole and out of the north pole, it can be shown that the internal dipole field remains exactly dipolar so that an exact analytic solution can be derived for the purpose of verifying the numerical algorithm. The quantity that was compared is the deflection angle, i.e., the azimuthal deviation from 'orange segment' mapping between two surfaces that are locally normal to the magnetic field. The accuracy of the above numerical procedures was found to depend on the following factors:

- *Boundary layer thickness.* Since the model is based on a boundary layer approximation, the metric scale factors should not vary significantly across the layer. From the benchmark results, it was determined that the variation in dipole scale factors across a 2 R_E layer (referenced to the equatorial plane), and straddling $L = 10$, could be as large as 30% with a corresponding variation in the deflection angle of 9% or less.

- *Linear projection of magnetic vectors.* The maximum (linearly) projected distance between adjacent magnetic normal grid surfaces is controlled by preselected tolerance factor ε. Arbitrarily small errors can be achieved by decr. the tolerance factor which decreases this distance. Continuous field line tracing would be realized in the limit where the tolerance factor approaches zero.

- *Discretization.* The error in the deflection angle is very sensitive to changes in the grid size in the x_3 direction (distance between magnetic normal surfaces), which, in turn, is controlled by the above mentioned tolerance factor ε. The grid size in the x_1 and x_2

68

directions ideally should be much smaller that the gradient scale lengths of the initial α(r) distribution.

- *Differencing and integration schemes.* The particular choice of differencing and integration schemes for solving the force-free boundary layer equations seems to have a minimal effect on the accuracy of the calculated deflection angle. For example, for the α distributions considered in the benchmark study, there was very little change in the results when the accuracy of the integration scheme was improved.

3. APPLICATION TO DAYSIDE REGION 1 CURRENTS

Application of the numerical algorithm described in the previous section is illustrated by considering a simple model for dayside field-aligned currents observed at low altitudes. These currents will be mapped outward to the magnetospheric equatorial plane under the assumption that the currents remain approximately force-free over a substantial length along the magnetic field. For the purpose of illustration and simplicity, a dipole model is used to specify boundary condition (A) in Sec. 2.5, and to represent a locally orthogonal coordinate system based on the magnetic geometry. The familiar dipole coordinates are specified in terms of the spherical polar coordinates (r, θ, ϕ): $x_1 = \phi$, the ordinary azimuth angle in the x–y plane; $x_2 = v = \sin^2\theta / r$, which is constant along a dipole field line and increases when going to lower L-shells (note that the L-shell is defined as $L = r_{eq} / R_E$ where r_{eq} is the radial distance to the point where the field line crosses the dipole equatorial plane); and $x_3 = \mu = \cos\theta / r^2$, which varies along a dipole field line and is constant along a magnetic potential orthogonal to a dipole field line. The metric scale factors for dipole geometry are

$$h_v = \frac{r^2}{\sin\theta}(1 + 3\cos^2\theta)^{-\frac{1}{2}} \qquad h_\phi = r\sin\theta \qquad h_\mu = h_v h_\phi = \frac{M}{B}$$

M is the earth's magnetic dipole moment, and B is the field strength.

According to *Iijima and Potemra* [1976], large-scale field-aligned currents are a statistically permanent feature of the high latitude ionosphere. These currents are concentrated in two adjacent annuli surrounding the geomagnetic pole. The higher latitude annulus is referred to as the region 1 current system; the lower latitude annulus is called the region 2 current system. The region 1 currents flow into the ionosphere in the morning sector and away from the ionosphere in the evening sector; the region 2 currents flow in the opposite direction at any given local time. The areas near local noon and midnight are not so simply classified and may be strongly time-dependent. We consider here the dayside region 1 current system at magnetic local times (MLT) between dawn and dusk, excluding the region from 1100-1300 MLT. Fig. 2 shows the MLT distribution of currents reported by *Iijimi and Potemra* [1978]. The upper panel shows the statistical distribution during relatively active periods of geomagnetic activity; the lower panel is for quieter periods.

The statistical local time dependence (i.e. the ϕ dependence) in the postnoon sector in Fig. 2 ahs been fitted to a simple polynomial function. The polynomial fit for both strongly and weakly disturbed periods, as well as selected data points from Fig. 2, are shown in Fig. 3. The corresponding curves for the prenoon sector shown in Fig. 3 are mirror reflections of those in the postnoon sector. (We do not mean to imply that the data in Fig. 2 are also mirror symmetric about noon!) The figure includes fitted points between 1100-1300 MLT, but these

currents near noon are not actually considered in the calculations described below. The region 1 field-aligned currents flow in opposite directions on either side of noon (as indicated in Fig. 2) whereas Fig. 3 plots only the magnitude of the current.

For the variation in field-aligned current in the ϑ direction, we model typical current profiles (actually magnetic deflections), examples of which can be found in the paper by *Iijima and Potemra* [1976] and in many other papers describing low altitude magnetic field data. Because satellite trajectories are rarely, if ever, exactly parallel to the ϑ direction, we do not actually have precise information on the v variation of the currents at low altitudes. As a consequence, we use the data only as a guide to generate a current profile in v that captures the basic features of the variation. The current variation in v was modeled by one-half period of a sine function that is zero at both edges of the region 1 current annulus and maximum midway though it. The width in v of the annulus is chosen to correspond to 1° in dipole magnetic latitude.

The product of the current profiles in v and ϕ defines our model for the field-aligned current at the ionosphere. The function $\alpha(\phi, v)$ on the ionospheric 'surface' (taken to be, with a small error, a constant μ surface near $1\,R_E$ geocentric) is constructed by multiplying the field-aligned current model by μ_0 (permeability of free space) and dividing the product by the dipole magnetic intensity at the earth's surface at the appropriate magnetic latitude. This α function is given to the algorithm described in Sec. 2 as input at the ionosphere, and the mapping of selected points on the ionospheric 'surface' to the magnetospheric equatorial plane due to this current is calculated. Note that we are not physically connecting the FFBL to its magnetospheric dynamo. The magnetic deflection inferred from the force-free mapping of the currents all the way to the magnetospheric equator should therefore be regarded only as an upper limit.

Magnetic field maps at the equatorial plane for weakly disturbed periods and strongly disturbed periods are shown in Fig. 4 and 5, respectively. The layer thickness is chosen to be 1° in dipole magnetic latitude, and the inner shell has been placed at the magnetic L-shell, $L = 10$, which locates the outer shell at $L=11.14$. These maps are displayed in a format similar to that use by *Fairfield* [1991] and are constructed by identifying at the ionosphere (actually at the earth's surface) ten different meridians of MLT from 0700-1100 and 1300-1700 in one hour steps. (Only five of the mapped meridians in Fig. 4 and 5 are distinct due to the assumed symmetry about 1200 MLT.) Force-free field lines intersecting each selected MLT meridian at 1 R_E are followed outward until they intersect the dipole equatorial plane. In this way, the set of points defining a MLT meridian at the earth's surface is mapped along field lines to the equatorial plane. The figures show the ten mapped MLT meridians between $L = 10$ and $L = 11.14$. Had the field remained purely dipolar in the FFBL, the mapped meridians would appear as segments of radial spokes, rather than curved lines, emanating from the origin at the indicated MLTs. Note that a nonlinear scale has been used to magnify the FFBL region between $10 \le L \le 11.14$.

In the morning sector, the force-free current is positive and into the ionosphere, and therefore, the deflection of the field is toward dawn; in the evening sector, the current is negative and away from the ionosphere, and the deflection is toward dusk. For a specific example, consider in Fig. 4 the curve labeled 0700 in the equatorial plane, which has been mapped through the layer from 1 R_E altitude. The mapped meridian in the equatorial plane lies further away from local noon than an 0700 MLT radial spoke would lie, at all mapped points, except on the inner L-shell where boundary condition (A) of Sec. 2.5 requires exact dipole mapping.

4. CONCLUSIONS

Given a distribution of the ratio of the field-aligned current to magnetic field on a surface whose normal is locally parallel **B** (a magnetic normal surface), the force-free boundary layer model and algorithm described here may be used to calculate magnetic field deformations due to force-free currents that flow in thin boundary layer regions. The model may also be used to determine the magnetic field mapping between magnetic normal surfaces in such regions. This model is general and can be applied in any locally orthogonal coordinate system, defined in terms of the exterior magnetic field (exterior means in the region where the force-free currents are zero, i.e., outside the FFBL).

An illustrative application of the model in dipole geometry to the statistical distribution of region 1 field-aligned currents suggests that the average dayside region 1 currents observed during geomagnetically active periods produce a maximum azimuthal deflection of the magnetic field of 26° when a magnetic field line is followed from the ionosphere to its equatorial crossing point. The corresponding deflection during weakly disturbed periods is about 21°. The maximum deflections occur on field lines where the field-aligned current density observed at low altitudes maximizes. These estimates of the deflection angle should be regarded only as upper limits, however, because the field-aligned current is not actually force-free along the entire length of the field line from the ionosphere to equatorial plane. To put these estimates in perspective, the T87 geomagnetic field model [*Tsyganenko*, 1987] exhibits a deflection angle of about 10° for a field line that passes through 1000 MLT and 75° invariant latitude in the ionosphere [*Fairfield*, 1991]. Although the T87 model does include some effects of field-aligned currents, these effects are introduced through an empirical polynomial fitting function in the model, so it is not known how much of the deflection is actually due to dayside region 1 currents or other magnetic deformations caused, for example, by the Chapman-Ferraro currents.

In considering future applications of this model, two improvements are suggested:

- Finding coordinate transformations that generate *locally orthogonal*, magnetic flux coordinates based on the exterior magnetic geometry may not be practical for realistic magnetospheric magnetic fields; the transformations may not even exist in general, especially for nonaxisymmetric magnetic fields. Formulation of the FFBL model in terms of nonorthogonal magnetic flux coordinates would allow grafting a FFBL model for field-aligned currents onto more realistic magnetic field models such as the semiempirical T87 model, semianalytical models [*Voigt*, 1981; *Hilmer and Voigt*, 1993; *Schulz and McNab*, 1987], or gridded numerical models [*Toffoletto et al.*, 1994]. Applications using a more realistic field model would allow examination of the effects of a magnetic minimum region near the magnetic cusps where the magnetic deformations due to field-aligned currents are likely to be large. We are currently in the process of implementing the FFBL model in a representation based on nonaxisymmetric, nonorthogonal magnetic flux coordinates.

- Although the force-free boundary layer model provides a well-defined procedure for mapping field-aligned currents and field lines between magnetic normal surfaces, it does not properly model the dynamo region in the outer magnetosphere. A better understanding of the field line mapping, for example, between the low-latitude boundary layer and the ionosphere, the magnetotail and the ionosphere, or the cusp region and the ionosphere will require coupling the force-free boundary layer model to appropriate physical

dynamo models. A boundary layer model for the generation of the region 1 currents, based on one-fluid magnetohydrodynamics, has been developed by *Drakou et al.* [1994], and it is expected that the two models will be coupled in the near future.

REFERENCES

Drakou, E., B. U. O. Sonnerup, and W. Lotko, Self-consistent steady-state model of the low-latitude boundary layer, *J. Geophys. Res.*, *99*, 2351, 1994.

Fairfield, D. H., An evaluation of the Tsyganenko magnetic field model, *J. Geophys. Res.*, *96*, 1481, 1991.

Hilmer, R. V. and G. -H. Voigt, A magnetospheric magnetic field model with flexible current systems driven by independent physical parameters, submitted to *J. Geophys. Res.*, 1993.

Iijima, T. and T. A. Potemra, The amplitude distribution of field-aligned currents at northern high latitudes observed by Triad, *J. Geophys. Res.*, *81*, 13, 1976.

Iijima, T. and T. A. Potemra, Large-scale characteristics of field-aligned currents associated with substorms, *J. Geophys. Res.*, *83*, 599, 1978.

Priest, E. R., *Solar Magnetohydrodynamics*, D. Reidel Publishing, Dordrecht, Holland, p. 133, 1982.

Schulz, M. and M. C. McNab, Source-surface model of the magnetosphere, *Geophys. Res. Lett.*, *14*, 182, 1987.

Stern, D. P., A simple model of Birkeland currents, *J. Geophys. Res.*, *98*, 5691, 1993.

Toffoletto, F.R., R. V. Hilmer, T. W. Hill, G. -H. Voigt, Solution of the Chapmann-Ferraro problem with an arbitrary magnetopause, submitted to *Geophys. Res. Lett.*, 1994.

Tsyganenko, N. A., Global quantitative models of the geomagnetic field in the cislunar magnetosphere for different disturbance levels, *Planet. Space Sci.*, *35*, 1347, 1987.

Vatan, K., Force-free boundary layer model for mapping field-aligned currents, M.S. Thesis, Thayer School of Engineering, Dartmouth College, Hanover, NH, 1993.

Voigt, G.-H., A mathematical magnetospheric model with independent physical parameters, *Planet. Space Sci.*, *29*, 1, 1981.
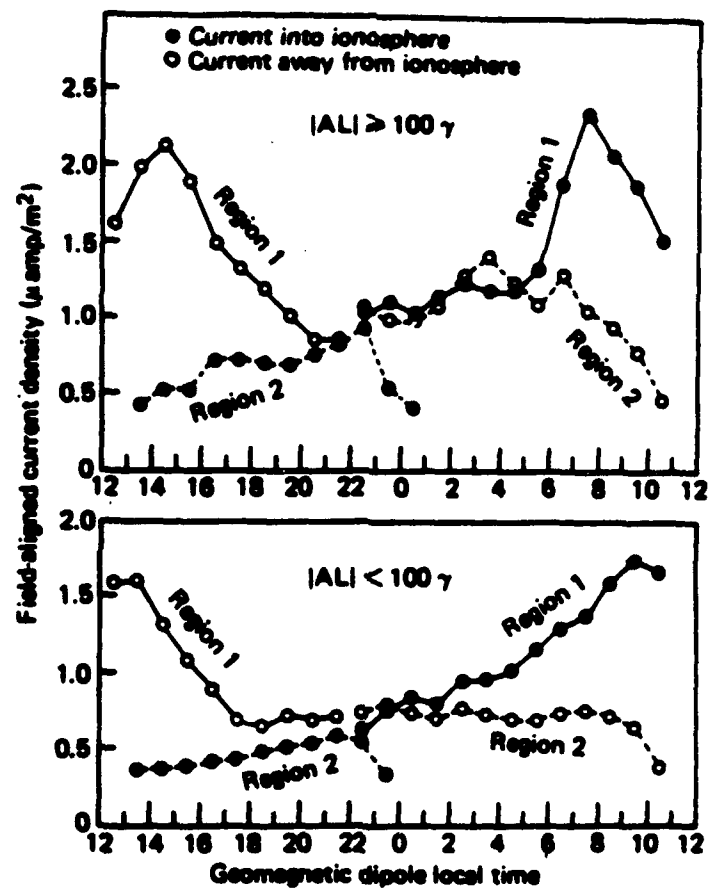
K. Vatan, Hewlett-Packard Company, Workstation Division, 300 Apollo Drive, Chelmsford, MA 01824
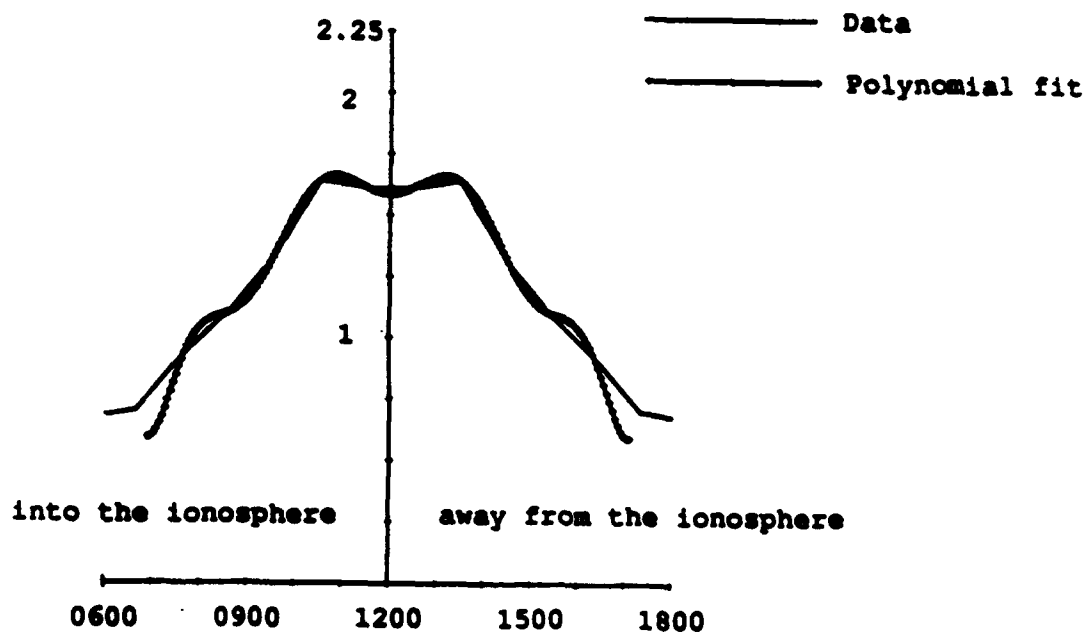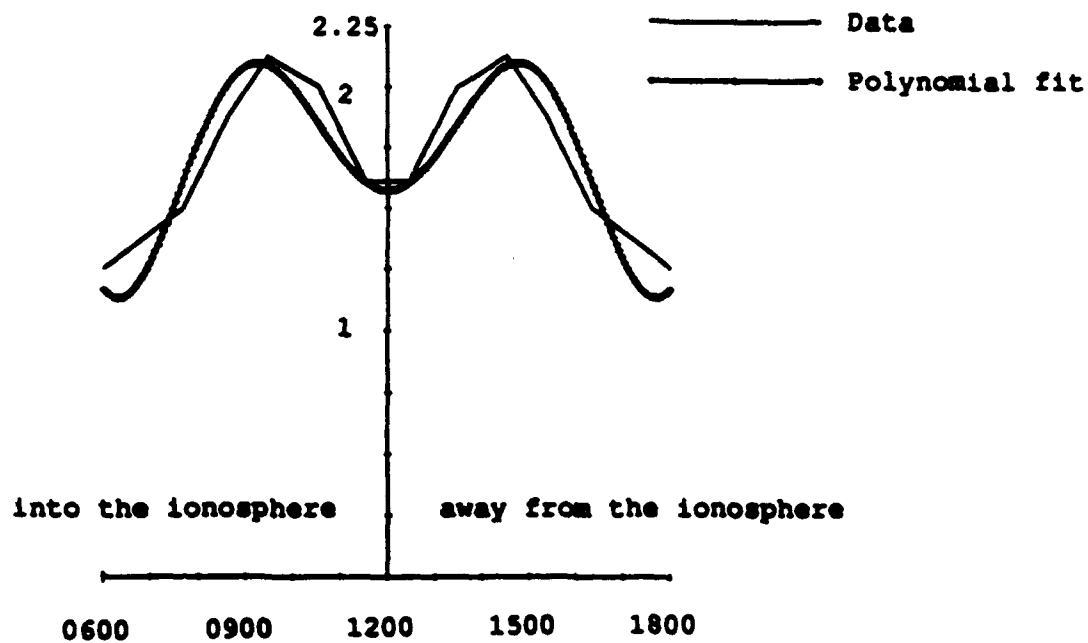
W. Lotko and B. U. O. Sonnerup, Thayer School of Engineering, Dartmouth College, Hanover, NH 03755
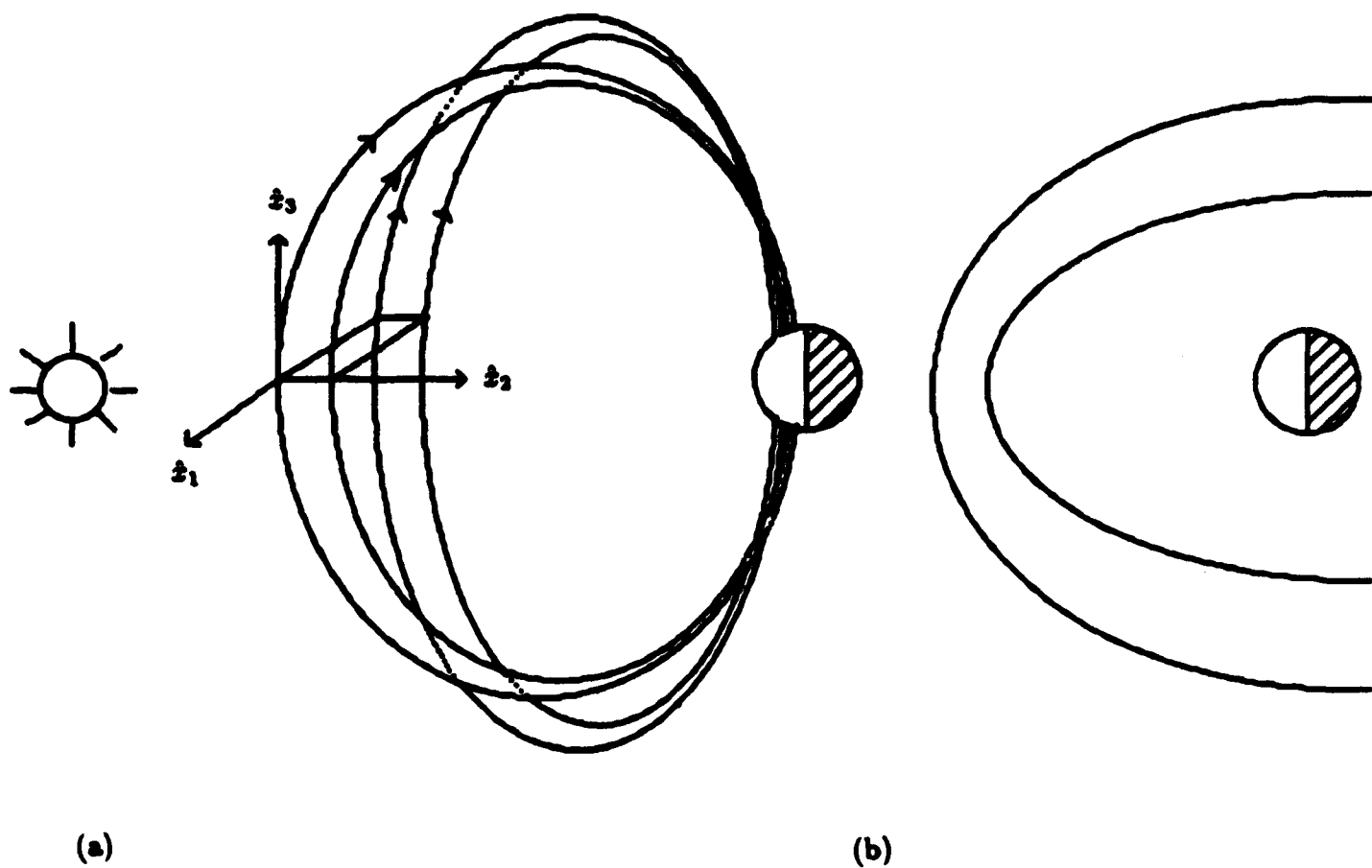
**Figure 1.** Geometrical domain: (a) noon-midnight projection and (b) equatorial plane projection.

Figure 2. Statistical pattern of observed current densities during (a) active periods and (b) weakly disturbed periods from Iijima and Potemra [1978].

Figure 3. Polynomial fit to average 'Region 1' current density versus magnetic local time for (a) active periods and (b) weakly disturbed periods.
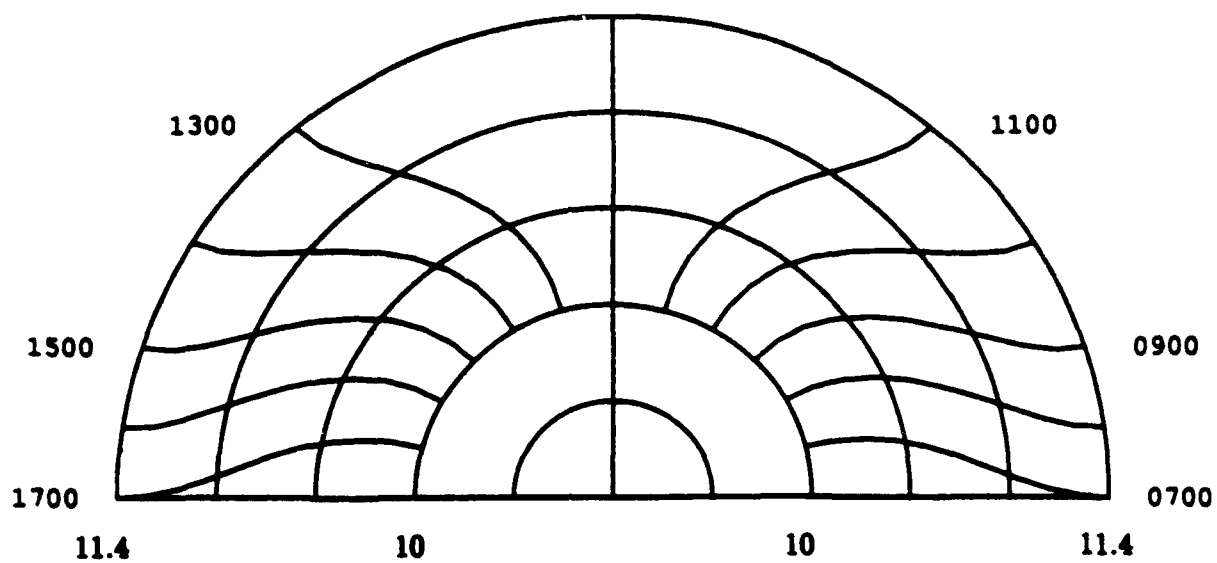
Figure 4. Magnetic field map for the α distribution chosen to model active periods.
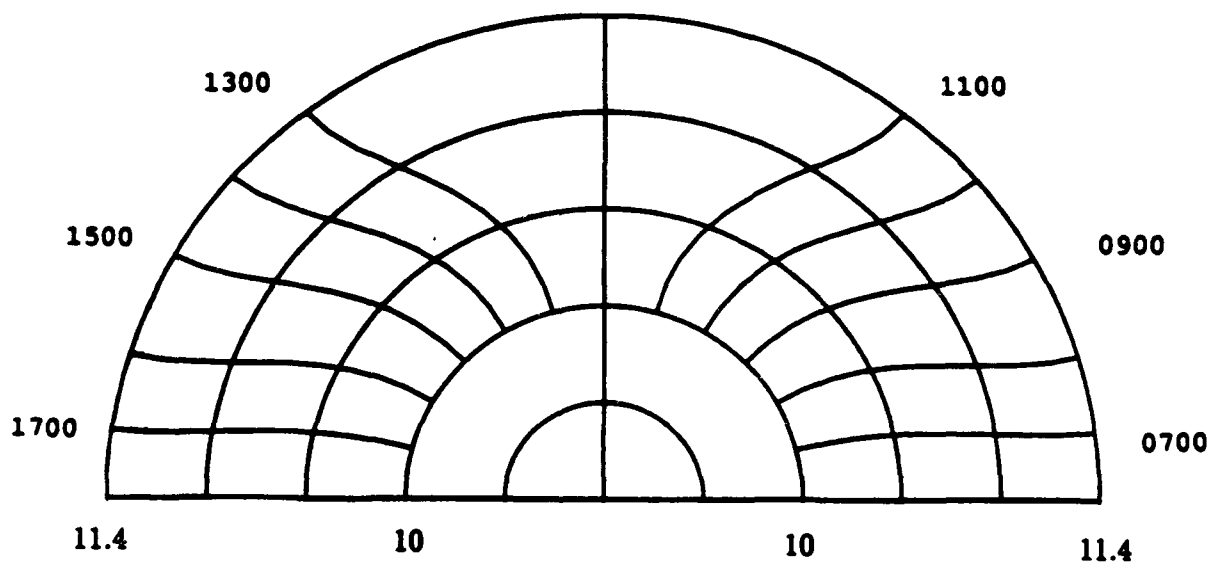
Figure 5. Magnetic field map for the α distribution chosen to model weakly disturbed periods.

APPENDIX 6:

Dynamics of Shear Velocity Layer with Bent Magnetic Field Lines

V. L. Galinsky   and   B. U. Ö. Sonnerup

Thayer School of Engineering, Dartmouth College

8000 Cummings Hall, Hanover, NH 03755-8000

Abstract. A fully three–dimensional, magnetohydrodynamic simulation of velocity–sheared plasma flow in an ambient transverse magnetic field with bent magnetic field lines has been performed. "Ionospheric–like" boundary conditions have been used for closing field–aligned currents, the two ionospheres being represented by conducting plates with constant resistivity. We have found a significant difference in the development of the Kelvin-Helmholtz instability, compared to the standard plane 2D case with a uniform transverse magnetic field: the growth rate of the instability drops significantly as bending increases. It seems likely that, under conditions representative of the Earth's low latitude boundary layer (LLBL), the Kelvin–Helmholtz instability can be suppressed completely by the magnetic field–line tension if bending of the magnetic field lines is sufficiently strong. We have also found that a combination of the tearing mode instability and the Kelvin–Helmholtz instability leads to the formation of localized 3D current/vortex tubes, the ionospheric foot prints of which can be considered as possible models of the auroral bright spots observed by the Viking satellite. Quantitative comparison of our results with satellite observations of velocity–sheared plasma flow in the LLBL and its ionospheric foot print indicates good agreement with the chosen model parameters.

77

Introduction

The interaction of the supersonic solar-wind flow with the Earth's magnetosphere creates interfaces or narrow layers where either a gradual or an abrupt transition in plasma and magnetic field properties occurs from interplanetary values to those of the magnetosphere. Several theoretical steady-state models of one of these regions, namely the magnetospheric low latitude boundary layer (LLBL) on closed field lines, have been discussed in the literature [*Sonnerup*, 1980; *Lotko et al.*, 1987; *Phan et al.*, 1989; *Drakou et al.*, 1994]. The steady-state nature of these models may impose restrictions on their applicability: in particular, shear flows are subject to the Kelvin-Helmholtz (KH) instability so that the question of the stability of the LLBL needs to be addressed. Most results of linear stability analyses of velocity shear layers are valid only when the unperturbed magnetic field lines are straight, and therefore, are not directly applicable to the above models where the geometry is more complex, having parabolic field lines with different curvature in different parts of the layer. Qualitatively, such geometries should have stability properties intermediate between the two cases of magnetic field perpendicular and parallel to the plane of the unperturbed shear layer. In the perpendicular case, instability occurs for $k\delta < 2$, k being the wave number and δ the shear width; in the parallel case, the wave modes are stable for velocity jumps less than twice the Alfvén speed [*e.g.*, *Miura and Pritchett*, 1982].

Processes taking place in the LLBL are also very important for understanding of the physics of mass, momentum and energy transfer from the solar wind to the magnetosphere. Three possible mechanisms have been proposed, namely "viscous like" interaction, magnetic field reconnection and impulsive plasma penetration. The discovery of flux transfer events (FTEs) increased the interest in the second mechanism and stimulated development of new reconnection models. Later a combination of viscous interaction and reconnection has been proposed as an explation of FTE formation [*La Belle-Hamer et al.*, 1988; *Belmont and Chanteur*, 1989].

In this paper, we investigate the influence of magnetic field–line bending on the stability of a velocity shear layer by use of full three-dimensional MHD simulations with ionospheric–like current closure boundary conditions. Several examples of unstable as well as nearly stable configurations will be shown and the parameter range where the KH mode is strongly suppressed by the magnetic field–line bending will be identified. The formation of localized current/vortex tubes, which provides a possible explanation of FTE–like signatures, will also be shown. Although there are several restrictions on the applicability of this model, we believe it can be used as a first step in understanding the properties of the KH instability in a magnetic-field geometry that is more realistic for the LLBL, than the simple straight–field line model.

Basic Equations and Model

The starting point is the fully three-dimensional, dissipative, compressible magnetohydrodynamic (MHD) equations, written in dimensionless form:

$$\frac{\partial \rho}{\partial t} = -\boldsymbol{\nabla} \cdot (\rho \mathbf{v})$$

$$\frac{\partial \mathbf{v}}{\partial t} = -(\mathbf{v} \cdot \boldsymbol{\nabla})\mathbf{v} - \frac{1}{\gamma M^2 \rho}\boldsymbol{\nabla} P + \frac{1}{M_a^2 \rho}(\boldsymbol{\nabla} \times \mathbf{B}) \times \mathbf{B} + \frac{1}{R}\boldsymbol{\nabla}^2 \mathbf{v}$$

$$\frac{\partial \mathbf{B}}{\partial t} = \boldsymbol{\nabla} \times (\mathbf{v} \times \mathbf{B}) + \frac{1}{R_m}\boldsymbol{\nabla}^2 \mathbf{B} \qquad (1)$$

$$\frac{\partial P}{\partial t} = -(\mathbf{v} \cdot \boldsymbol{\nabla})P - \gamma P \boldsymbol{\nabla} \cdot \mathbf{v}$$

$$\boldsymbol{\nabla} \cdot \mathbf{B} = 0$$

where $\mathbf{v}(x,y,z,t) = (v_x, v_y, v_z)$ is the flow velocity; $\mathbf{B}(x,y,z,t) = (B_x, B_y, B_z)$ is the magnetic field; R is the Reynolds number; R_m is the magnetic Reynolds number; M is the sonic Mach number; and M_a is the Alfvén Mach number. All lengths are normalized by a characteristic perpendicular half width of the shear flow, $a = \delta/2$; the velocity by the velocity jump, V_0; the magnetic field by the background magnetic field, B_0. The sonic and Alfvén Mach numbers are defined as $M_a = V_0/v_s$ and $M_a = V_0/v_a$, where

$v_s = (\gamma P_0/\rho_0)^{1/2}$ and $v_a = B_0/(4\pi\rho_0)^{1/2}$ are the sound speed and the Alfvén speed, respectively; the Reynolds number is defined as $R = aV_0/\nu$ and the magnetic Reynolds number as $R_m = 4\pi aV_0/(\eta c^2)$. The pressure, P, and density, ρ, are normalized by their values away from the shear layer. Resistive and viscous dissipation terms in the energy equation are neglected.

The initial configuration used in this study is a velocity shear layer in a nonuniform magnetic field, the nonuniformity being created by electic currents that connect the plasma in the layer to two conducting plates which serve to represent the northern and southern ionospheres. A sketch of the configuration is shown in Figure 1. The quantitative expressions describing the initial field and plasma flow are:

$$\mathbf{v}(x,y,z,0) = \frac{V_0}{2} \tanh(\frac{y}{a}) \, \hat{x}, \; B_x(x,y,z,0) = -\alpha \, z \, \tanh(\frac{y}{a}),$$

$$B_y(x,y,z,0) = 0, \; B_z(x,y,z,0) = \mathbf{B}_0, \; \rho(x,y,z,0) = \rho_0, \tag{2}$$

$$P(x,y,z,0) + \frac{B^2(x,y,z,0)}{8\pi} = \text{const.}$$

The main drawback of this configuration is that it is not a strict equilibrium. The $\hat{x}$ component of the $\mathbf{j} \times \mathbf{B}$ force is not balanced by any other force and therefore will result in a gradual slowing down of the flow and an associated decrease in the velocity jump across the layer.

In the present study, the simulation domain is a rectangular box with periodic boundary conditions in the flow direction ($\hat{x}$). The boundary conditions in the direction across the layer ($\hat{y}$) are simply "free-slip" ones. We use mirror and "free-slip" boundary conditions in the equatorial plane ($z = 0$) for all variables and in the upper plane for the velocity components. In order to write boundary conditions for the B_x and B_y components of the magnetic field at the upper or lower edge, we assume that our configuration is confined between two parallel resistive plates at $z = \pm L_z$. Using Ohm's law and current continuity conditions at the top of our box, it is easy to obtain equations for the B_x and B_y components on the upper plane at $z = L_z$. In dimensionless form

these equations are

$$\nabla_{\perp}^2\left(B_x - \frac{\eta\Sigma}{a}\frac{\partial B_x}{\partial z}\right) = -R_\Sigma\frac{\partial}{\partial y}\left[\frac{\partial}{\partial y}(v_x B_z) - \frac{\partial}{\partial x}(v_y B_z)\right] + \frac{\eta\Sigma}{a}\frac{\partial^3 B_z}{\partial x\partial^2 z}$$

$$\nabla_{\perp}^2\left(B_y - \frac{\eta\Sigma}{a}\frac{\partial B_y}{\partial z}\right) = R_\Sigma\frac{\partial}{\partial x}\left[\frac{\partial}{\partial y}(v_x B_z) - \frac{\partial}{\partial x}(v_y B_z)\right] + \frac{\eta\Sigma}{a}\frac{\partial^3 B_z}{\partial y\partial^2 z} \qquad (3)$$

where $\nabla_{\perp}^2 = \partial^2/\partial x^2 + \partial^2/\partial y^2$ and R_Σ is equal to $R_m\eta\Sigma/a$.

Finally, a boundary condition for the pressure can be determined from the absence of a normal component of velocity on the upper plane.

For space discretization the Fourier pseudo-spectral representation was used in the x direction and the Chebyshev tau method in the y and z directions. We solved the nonlinear equations using an iteration scheme and a time splitting alternating direction implicit (ADI) method, modified for use with Fourier and Chebyshev spectral discretizations.

Simulation Results

In order to allow the KH instability to develop, a perturbation was imposed on the initial configuration (2). The wavelength of this perturbed mode is equal to the entire length of the system in the $\hat{x}$ direction and has been chosen to be the wavelength of the fastest growing mode (FGM). Since we do not intend to address the question of the inverse cascade, i.e., the formation of structures with longer wavelengths than those predicted by linear theory [*Belmont and Chanteur*, 1989], we choose the system length to be equal to the FGM wavelength: for all our simulation runs the value $k_x a = 0.45$, and hence $L_x \simeq 14a$, was used. The amplitude of the initial perturbation of the $\hat{y}$ component of the velocity $|v_y|$ was equal to $0.01V_0$. We also used $L_y = L_z = 20a$, $R = 1000$, $R_m = 100$, $M = 0.77$ and $M_a = 1.0$ for all runs.

Figure 1a shows the temporal evolution of the maximum of the $\hat{y}$ component of the flow velocity $|v_y|$, normalized by V_0, for three different values of R_Σ, namely 0.1, 0.2 and 0.4, as well as for the purely two–dimensional transverse case of the KH instability which

81

corresponds to $R_\Sigma = 0$. One can see that for all four Reynolds numbers the velocity perturbation initially grows linearly and then saturates at some level. The linear growth rate decreases significantly with increasing magnetic Reynolds number R_Σ. The level of the nonlinear saturation is almost the same for $R_\Sigma = 0.1$ as for the transverse case, $R_\Sigma = 0$, but for $R_\Sigma = 0.4$ this level is much lower.

Figure 2 shows streamlines and current distribution, at the end of our simulation, for the case of strong bending of the magnetic field lines ($R_\Sigma = 0.4$). The term strong bending is used only in a relative sense; the maximum amplitude of the component of the magnetic field parallel to the flow ($\hat{x}$) is approximately 20% of the perpendicular ($\hat{z}$) component. The KH instability is almost suppressed in this configuration, the level of nonlinear saturation being only 2.5 times higher than the level of the initial perturbation ($0.025 V_0$). The current sheet is only slightly disturbed and no localized current structures are formed. We may compensate for the decrease of the velocity jump across the layer during the simulation, which in this case is rather big ($\Delta V_{x0}/\Delta V_x = 6$), by normalizing the amplitude of the perturbed $\hat{y}$ component of the velocity by the magnitude of this jump. At the end of the simulation, this normalized velocity component is approximately 0.15, which should be compared to a value of 0.33 for the transverse case, $R_\Sigma = 0$, where no decay of the velocity jump occurs.

In light of this result, it seems likely that strong bending of the magnetic field lines can suppress or at least significantly slow down the KH instability. Therefore, previous two–dimensional analyses of the stability of the LLBL [*Miura and Pritchett*, 1982] and MHD simulations of that layer [*Miura*, 1992; *Wei and Lee*, 1993], all of which were carried out in the equatorial plane and using straight magnetic field lines, may be strictly valid only in a limited region not too far from the subsolar stagnation point, where field–line bending is not strong enough to prevent the KH instability. But as the plasma flow proceeds toward the tail, the curvature of the magnetic field lines increases and one cannot neglect their tension any more.

Figures 3 and 4 show current lines in the system for $R_\Sigma = 0.2$ and $R_\Sigma = 0.1$, respectively. The current distribution is more complicated than in the previous case. The perturbations introduced by the KH instability on the initially uniform current sheet are so strong that they result in its destruction and in the creation of localized vortex/current tubes. This process looks similar to magnetic island formation in association with the tearing mode instability of a two dimensional current sheet. Our simulations show the formation of localized 3D current structures aligned with the magnetic field. However, the processes taking place near the upper and lower ends of these tubes and the existence of the inverse cascade in the system are probably important for understanding the long–time development of these tubes.

In order to make geophysical estimates from our simulations, the upper conducting plate must be given properties that mimic the ionoshere. A relationship between the conductivity of the plate and the effective height–integrated conductivity, Σ_{pi}, of the ionosphere, based on the conservation of magnetic flux and field–aligned current, was given by *Sonnerup* [1980]. Using our dimensionless parameter $R_\Sigma = R_m \eta \Sigma/a$ it can be written as:

$$\Sigma_{pi} = \frac{c^2}{4\pi V_0} \frac{1}{k} \frac{B}{B_i} \left(\frac{dx}{dx_i}\right)^2 R_\Sigma \tag{4}$$

The total field-aligned current in the ionosphere, averaged over one period in the $\hat{x}$ direction, is given by

$$< I_{\parallel i} >= \frac{c}{4\pi} \frac{dx}{dx_i} \left(< B_x > \Big|_{\substack{y=0 \\ z=L_z}} - < B_x > \Big|_{\substack{y=L_y \\ z=L_z}} \right) \tag{5}$$

where the subscript i denotes ionospheric quantities and $[dx/dx_i]$ is the mapping factor for distances in the main flow direction. Using typical values for the magnetospheric parameters [*e.g.*, *Sonnerup*, 1980], $B = 3 \times 10^{-8}t$, $B_i = 5 \times 10^{-5}t$, $V_0 = 200$km/s, $dx/dx_i = 51.3$ and taking the coupling factor $k = 1$, one can estimate the values of Σ_{pi} and $< I_{\parallel i} >$ as $6.3R_\Sigma$ mho and $1.2R_\Sigma$ A/m respectively. With $R_\Sigma = 0.1 - 0.4$ these values are roughly consistent with observed values of 2-3 mho and 0.15 A/m.

It should be noted that many satellite observations have shown the presence of spatially periodic bright spots in the postnoon auroral region. Their dimensions usually range approximately from 50 to 200 km and their separation is about 100–500 km [*e.g., Lui et al.*, 1989]. Recently *Wei and Lee* [1993] suggested that these spots can represent ionospheric signatures of vortices created in the LLBL by the KH instability. The formation of vortex/current tubes in our simulations indicates that regions of large field–aligned current density and vorticity, with dimensions comparable to observed values, will occur in the ionosphere representing the footprints of these tubes.

Conclusion

The real plasma flow and magnetic field configuration in the magnetopause–boundary layer region is significantly different from, and far more complicated than, the one we use here. In particular, our use of conducting plates to represent the ionosphere ignores Alfvén–wave transit time effects. Nevertheless, our model can be used for at least a qualitative assessment of the role and nature of the Kelvin–Helmholtz instability in the LLBL and other internal magnetospheric shear layers with current closure in the ionosphere.

The following main conclusions can be drawn from our simulations:

1. Magnetic field–line bending leads to a significant decrease of the growth rate of the Kelvin–Helmholtz instability. The value of this decrease depends on the amount of field–line bending and, hence, on the conductivity of the auroral ionosphere to which the shear layer is magnetically coupled.

2. It seems likely that sufficiently strong bending of the magnetic field lines, corresponding in our case to the magnetic Reynolds number (based on an equivalent ionospheric conductivity) $R_\Sigma \geq 0.4$, can slow down the development of the Kelvin–Helmholtz instability or suppress it altogether.

3. A combination of the tearing mode instability and the Kelvin–Helmholtz instability

leads to a formation of localized three–dimensional vortex/current tubes. A projection of these structures into the ionosphere produces regions of enhanced field–aligned current density and vorticity which may represent auroral bright spots observed by for example the Viking satellite [*Lui et al.*, 1989].

4. We have also carried out simulations with a velocity profile more representative of the LLBL, namely $\mathbf{v}_x = \frac{1}{2}V_0(1 - \tanh(\frac{y}{a}))$, the result being an even stronger suppression of the KH instability, presumably caused by the presence of field–line curvature at the point of inflection of the velocity profile.

References

Belmont, G., and G. Chanteur, Advances in magnetopause Kelvin-Helmholtz instability studies, *Physica Scripta, 40*, 124, 1989.

Drakou, E., B. U. Ö Sonnerup, and W. Lotko, Self–consistent steady–state model of the low–latitude boundary layer, *J. Geophys. Res., 99*, 2351, 1994

La Belle-Hamer, A. L., Z. F. Fu, and L. C. Lee, A mechanism for patchy reconnection at the dayside magnetopause, *Geophys. Res. Lett., 15*, 152, 1988.

Lotko, W., B. U. Ö. Sonnerup, and R. L. Lysak, Nonsteady boundary layer flow including ionospheric drag and parallel electric field, *J. Geophys. Res., 92*, 8635, 1987.

Lui, A. T. Y., D. Venkatesan, and J. S. Murphree, Auroral bright spots on dayside oval, *J. Geophys. Res., 94*, 5515, 1989.

Miura, A., and P. L. Pritchett, Nonlocal stability analysis of the MHD Kelvin-Helmholtz instability in a compressible plasma, *J. Geophys. Res., 87*, 7431, 1982.

Miura, A., Kelvin-Helmholtz instability at the magnetospheric boundary: dependence on the magnetosheath sonic Mach number, *J. Geophys. Res., 97*, 10665, 1992.

Phan, T. D., B. U. Ö. Sonnerup, and W. Lotko, Self-Consistent model of the low-latitude boundary layer, *J. Geophys. Res., 94*, 1281, 1989.

Sonnerup, B. U. Ö, Theory of the Low-Latitude Boundary Layer, *J. Geophys. Res., 85*, 2017, 1980.

Wei, C. Q., and L. C. Lee, Coupling of magnetopause–boundary layer to the polar ionosphere, *J. Geophys. Res., 98*, 5707, 1993.
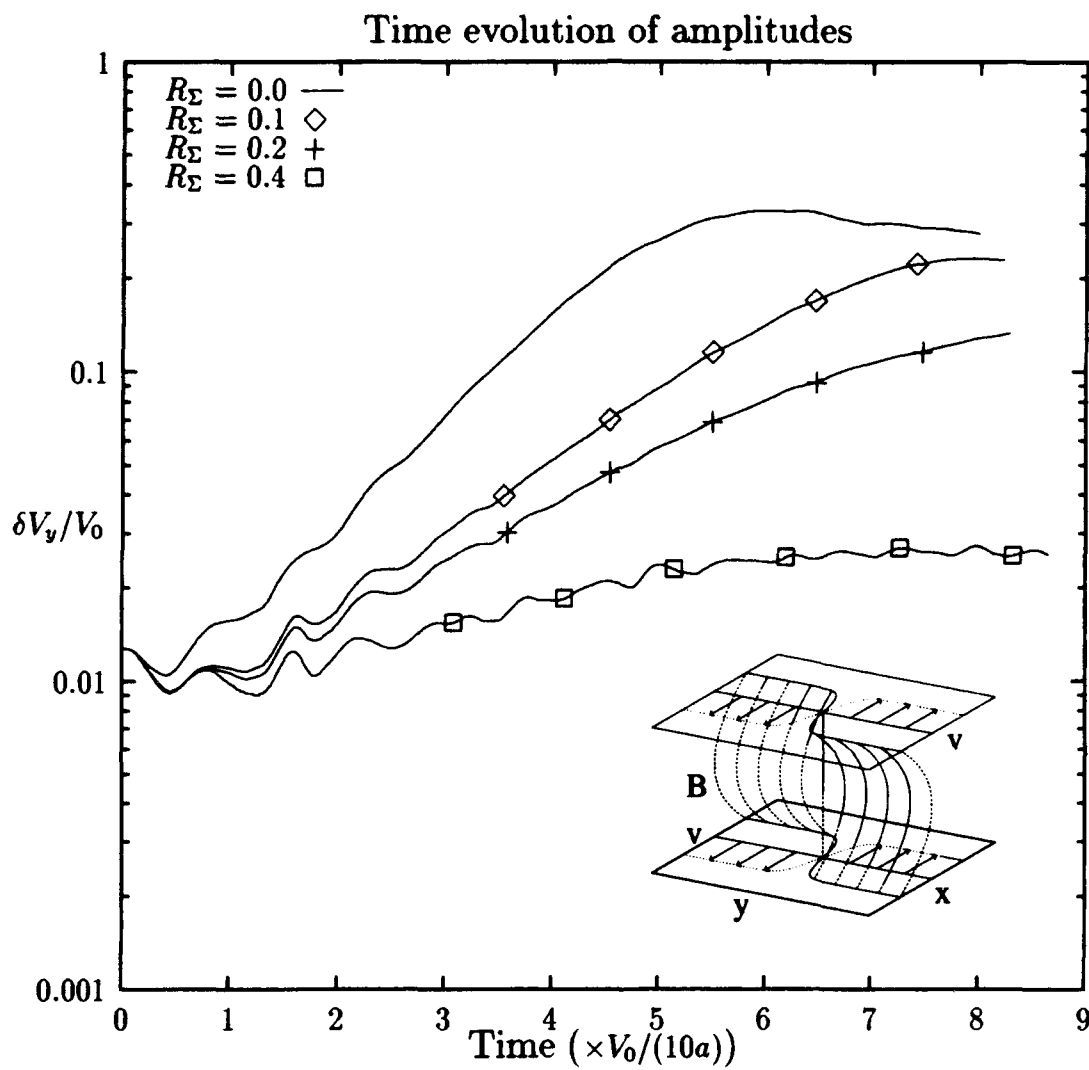
Figure 1. Temporal evolution of $|v_y|$. Insert: sketch of plasma flow and magnetic field configuration confined between two conducting plates
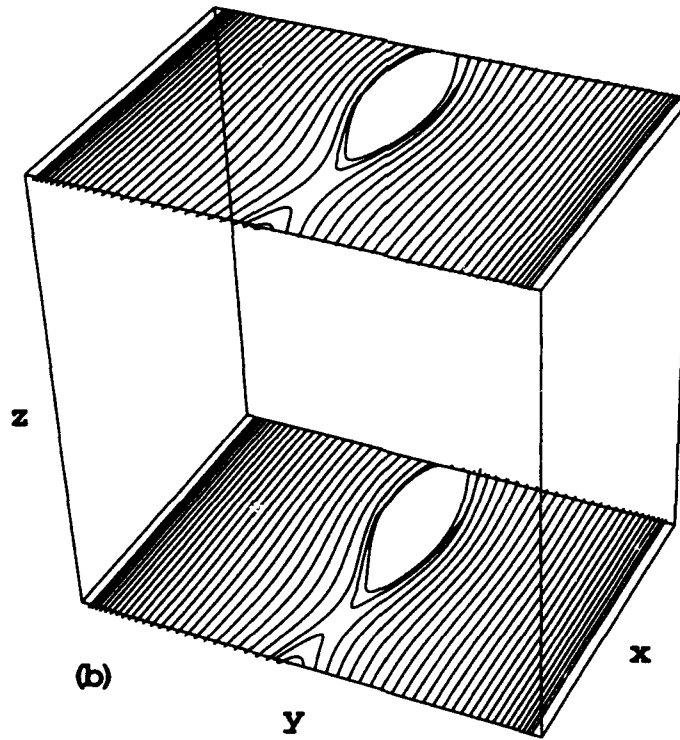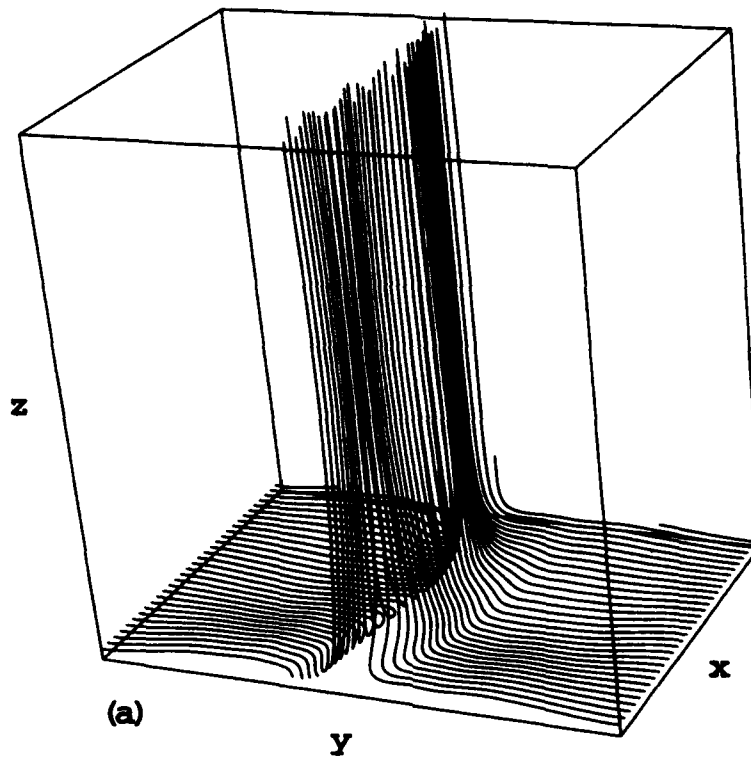
Figure 2. Current lines (a) and streamlines (b) at the end of the simulation, $t = 86a/V_0$, for $R_\Sigma = 0.4$.

88
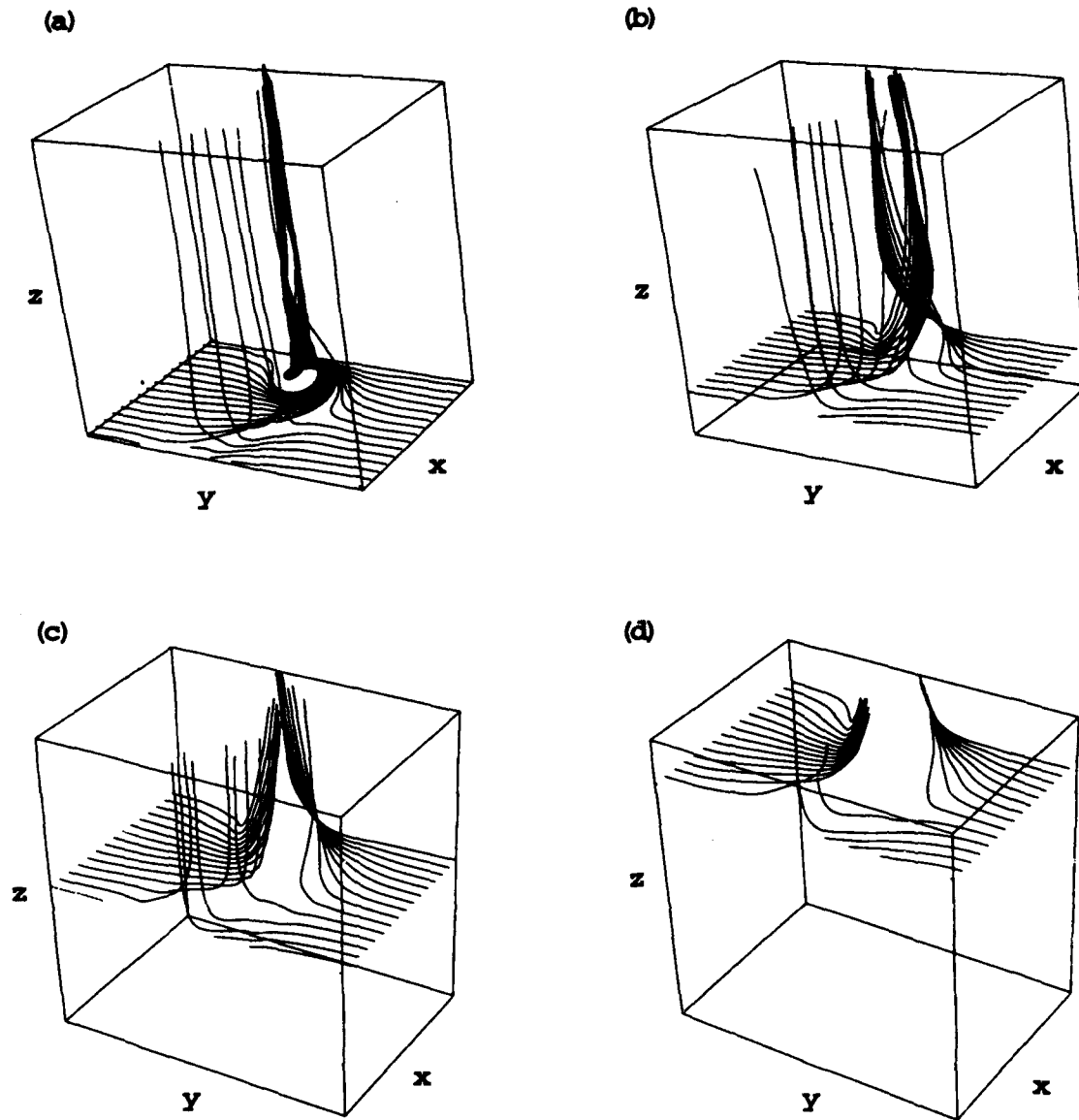
Figure 3. Current lines entering the slab at four different planes for $R_\Sigma = 0.2$ at the end of the simulation ($t = 83a/V_0$): (a) $z = 0.02L_z$; (b) $z = L_z/4$; (c) $z = L_z/2$; and (d) $z = 3L_z/4$.
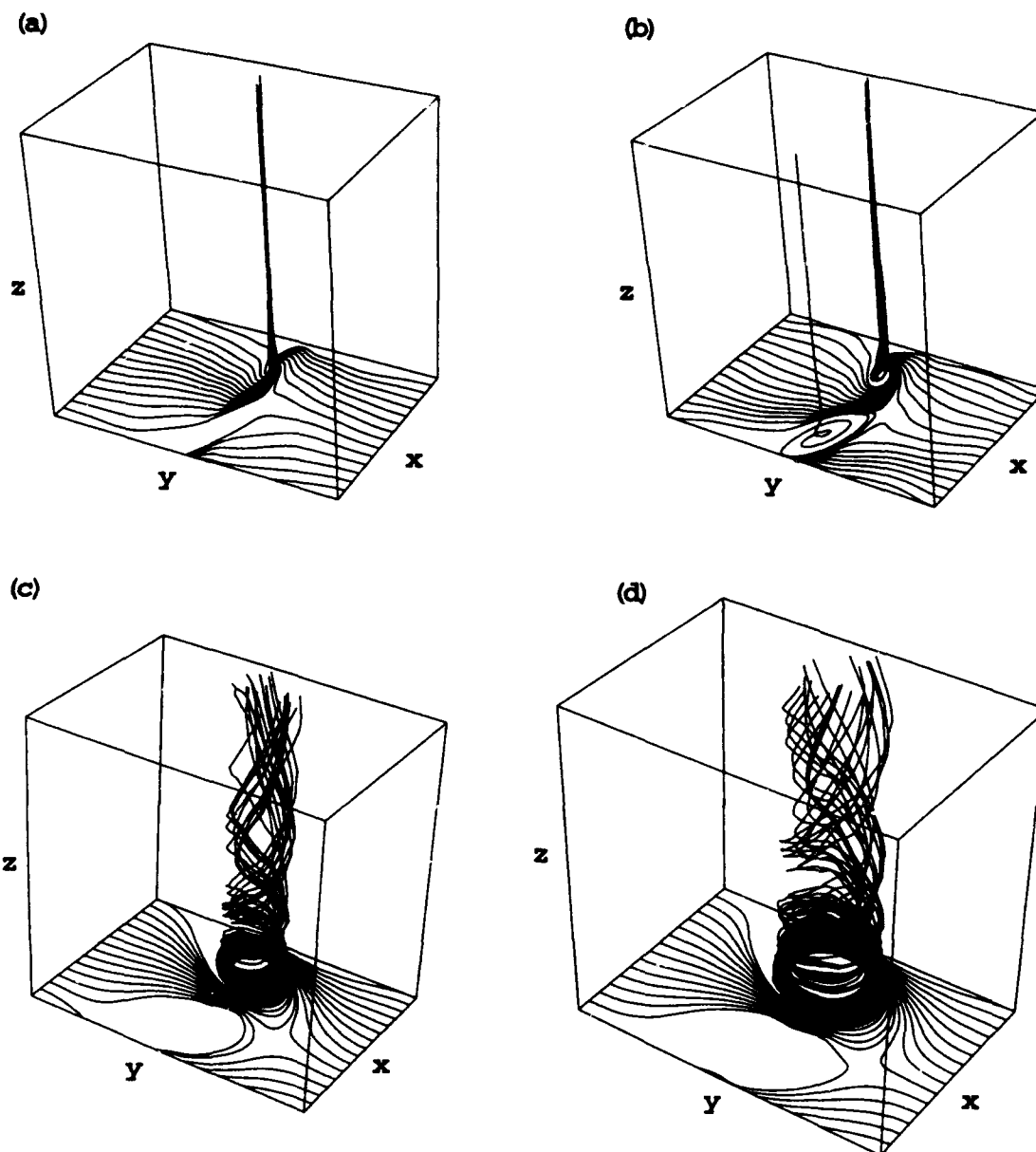
Figure 4. Current lines for $R_\Sigma = 0.1$, plotted at four different times: (a) $t = 20a/V_0$; (b) $t = 40a/V_0$; (c) $t = 60a/V_0$; and (d) $t = 82a/V_0$.

Resistive tearing-mode instability in a current sheet with equilibrium viscous stagnation-point flow

By T. D. PHAN* AND B. U. Ö. SONNERUP

Thayer School of Engineering, Dartmouth College, Hanover, New Hampshire 03755, U.S.A.

An analysis is presented of linear stability against tearing modes of a current sheet formed between two oppositely magnetized plasmas forced towards each other in two-dimensional steady stagnation-point flow. The velocity vector in this flow is confined to planes perpendicular to the reversing component of the magnetic field. The unperturbed state is an exact resistive and viscous equilibrium in which the resistive diffusion outwards from the current sheet is exactly balanced by the inward motion associated with the stagnation-point flow. Thus the behaviour of the tearing mode can be examined even when the resistive diffusion time is comparable to or smaller than the growth time of the instability. The linear ordinary differential equation describing the mode structure is integrated numerically. For large Lundquist number S and viscous Reynolds number Re the Furth–Killeen–Rosenbluth scaling of the growth rate is recovered with excellent accuracy. The influence of the stagnation-point flow on the tearing mode is as follows: (i) long-wavelength perturbations are stabilized so that the unstable regime falls between a short-wavelength and a long-wavelength marginal state; (ii) for sufficiently low Lundquist number $(S < 12\cdot25)$ the current sheet is completely stable to tearing-mode perturbations; (iii) the presence of high viscosity reduces the growth rate of the tearing instability. This effect is more important at small wavelength. Finally, application of the results from this study to the problem of solar-wind plasma flow past the earth's magnetosphere is briefly discussed.

1. Introduction

Magnetic reconnection is thought to be an important process for the conversion of magnetic field energy into kinetic and thermal energy in cosmic as well as laboratory plasmas (for reviews see e.g. Vasyliunas 1975; Sonnerup 1979; Forbes & Priest 1987). Reconnection is initiated in thin current sheets as a result of the tearing mode (Furth, Killeen & Rosenbluth 1963; Laval, Pellat & Vuillemin 1966; Wesson 1966; Cross & Van Hoven 1971; Lee & Fu 1986), in which magnetic islands, produced by non-steady reconnection, grow ultimately to large amplitudes. But current sheets observed in space plasmas, for example in association with solar flares or at the earth's magnetopause, sometimes remain stable for time periods far exceeding the growth time associated with the tearing mode. Among the effects that may influence tearing modes in a

* Now at Max-Planck-Institut für Extraterrestrische Physik, 8046 Garching, Germany.

substantial way are flows across the current sheet (Dobrott, Prager & Taylor 1977; Killeen & Shestakov 1978) and flows along it (Bulanov, Syrovatsky & Sakai 1978; Einaudi & Rubini 1986, 1989; Chen & Morrison 1990; Ofman, Chen & Morrison 1991). However, a weakness of all previous analyses based on resistive MHD is that the unperturbed state was not an exact solution of the resistive MHD equations. Left alone, the unperturbed current sheet would spread out with increasing time. Most of the previous studies of the resistive tearing mode neglected this resistive diffusion effect; thus the results reported are valid only in the limit where the diffusion time is much longer than the growth time of the instability. In this limit the Lundquist number $S = t_D/t_A$ is much greater than unity, where t_A is the Alfvén transit time across the current layer and t_D is the resistive diffusion time of the current sheet. The Lundquist number of current sheets in magnetic reconnection configurations, however, may sometimes be of order unity (Lee & Fu (1986) gave $2 < S < 100$). The studies of the tearing mode in this regime have been limited and not entirely satisfactory: Lee & Fu (1986) investigated the tearing mode in the low-S regime without taking into account the resistive decay of the unperturbed current sheet. For a Harris-type current sheet ($B \propto \tanh x$), they found that the growth rate obtained by assuming uniform conductivity and neglecting the resistive decay is essentially the same as that obtained with a spatially varying conductivity of the form $\sigma \propto \mathrm{sech}^2 x$, which allows the unperturbed state to remain time-independent. However, this kind of conductivity profile, with $|\sigma| \to 0$ as $|x| \to \infty$, is usually not relevant to the problem of magnetic reconnection. In order to investigate the tearing mode in the low S-regime in a satisfactory way, one would need to either perform a stability analysis of a non-equilibrium current sheet, taking into account the resistive spreading of the sheet in a self-consistent manner, or perform such an analysis on a sheet in which the resistive diffusion is counterbalanced by an incoming plasma flow. Dobrott *et al.* (1977) recognized the importance of resistive decay of the unperturbed current sheet. However, although their inclusion of an uniform 'diffusion velocity' to describe the spreading of the layer may give an indication of the effect of diffusion on the tearing mode, it is in fact inconsistent with the magnetic induction equation. In the present paper we perform a linear tearing-mode stability analysis of one member of the family of exact resistive current-sheet equilibria found by Sonnerup & Priest (1975) for the case of two oppositely magnetized plasmas pushed towards each other in two-dimensional stagnation-point flow. The equilibrium structure and thickness of the unperturbed current sheet is such that the resistive diffusion outwards from the sheet is exactly balanced by the inward motion associated with the stagnation-point flow. The latter is two-dimensional, with the flow confined to planes perpendicular to the reversing component of the magnetic field. This equilibrium allows us to examine the tearing mode over the entire range of parameter values.

The paper is organized as follows. In §2 the basic equations and the relevant properties of the equilibrium configuration are reviewed. In §3 we develop the linear perturbation equations and, by appropriate assumptions concerning the nature of the perturbations, reduce them to a form suitable for the subsequent analysis. In §4 the method of solution is described. In §5 numerical solutions of the linearized equations are presented. In particular, the dependence of the growth rate of the tearing mode on the Lundquist number, i.e. the magnetic

Reynolds number based on the Alfvén speed, on the viscous Reynolds number and on the wavelength of the perturbation is examined. Examples of the eigenmode structure are also shown. Finally, a discussion of the results is given in §6.

2. Basic equations and the equilibrium state

The analysis is based on the equations of the incompressible one-fluid resistive and viscous magnetohydrodynamics, namely

$$\nabla . \mathbf{v} = 0, \tag{1}$$

$$\rho \frac{\partial \mathbf{v}}{\partial t} + \rho (\mathbf{v} . \nabla \mathbf{v}) = -\nabla p + \frac{1}{\mu_0} (\nabla \times \mathbf{B}) \times \mathbf{B} + \eta \nabla^2 \mathbf{v}, \tag{2}$$

$$-\frac{\partial \mathbf{B}}{\partial t} + \nabla \times (\mathbf{v} \times \mathbf{B}) + \frac{\nabla^2 \mathbf{B}}{\mu_0 \sigma} = 0, \tag{3}$$

$$\nabla . \mathbf{B} = 0, \tag{4}$$

where $\mathbf{B}$, $\mathbf{v}$, ρ and p are the magnetic field, plasma velocity, density and pressure respectively. η is the dynamic viscosity and σ is the electrical conductivity, both of which are assumed uniform and constant.

Steady-state exact solutions to this system of equations, for symmetric and asymmetric MHD stagnation-point flows in two and/or three dimensions, have been given by Sonnerup & Priest (1975), Besser, Biernat & Rijnbeek (1990) and Phan & Sonnerup (1990). These solutions represent generalizations of the initial work by Parker (1973) on resistive current layers in the presence of two-dimensional stagnation-point flow. The general form of Sonnerup and Priest's (1975) solutions is

$$\mathbf{v}_0 = -c_1 x\hat{\mathbf{x}} + c_2 y\hat{\mathbf{y}} + c_3 z\hat{\mathbf{z}}, \tag{5}$$

$$\mathbf{B}_0 = B_{0y}(x)\,\hat{\mathbf{y}} + B_{0z}(x)\,\hat{\mathbf{z}}, \tag{6}$$

where the positive constants c_1, c_2 and c_3 are related by

$$c_1 = c_2 + c_3$$

to ensure that the flow is divergence-free. It should be noted that the equilibrium flow, described by (5), is irrotational. Consequently, the viscous force on the flow is zero. However, in the perturbed state the flow becomes rotational, and the effect of viscosity may be important.

An early attempt to study the behaviour of the tearing mode in general three-dimensional stagnation-point flow and field configurations of the type given by (5) and (6) was made by Sonnerup & Sakai (1981). They used an analytical approach in which the island stretching caused by the accelerating unperturbed plasma motion along the current sheet was treated by use of a method introduced by Bulanov *et al.* (1978). However, the analysis of Sakai & Sonnerup remained unsatisfactory in some aspects and was never completed. They did not consider the special case $c_2 = 0$, which is much simpler than the general case on account of the absence of island stretching. It is this special case that will be studied here. For $c_2 = 0$ the flow is two-dimensional and confined to the (x, z)-plane, i.e.

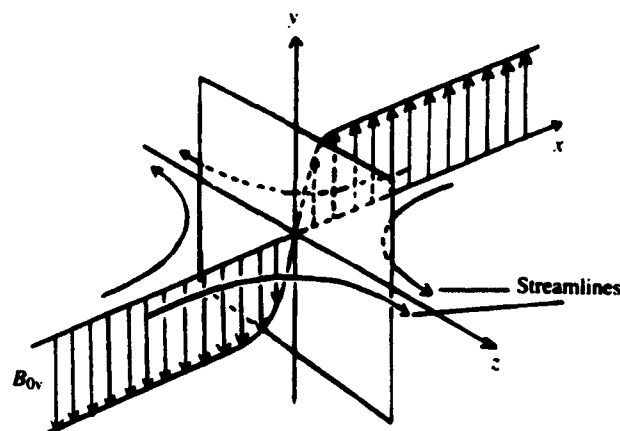$$\mathbf{v}_0 = c_1(-x\hat{\mathbf{x}} + z\hat{\mathbf{z}}), \tag{7}$$

FIGURE 1. Equilibrium plasma flow and geometry of reversing magnetic field
component B_{0y}.

and the magnetic field components B_{0y} and B_{0z} obey

$$\frac{1}{\mu_0 \sigma}\frac{d^2 B_{0y}}{dx^2} + c_1 x \frac{dB_{0y}}{dx} = 0, \tag{8}$$

$$\frac{1}{\mu_0 \sigma}\frac{d^2 B_{0z}}{dx^2} + c_1 x \frac{dB_{0z}}{dx} + c_1 B_{0z} = 0. \tag{9}$$

Also the pressure is obtained from a Bernoulli-type equation

$$p = p_0 - \tfrac{1}{2}c_1^2 \rho(x^2 + z^2) - \frac{B_{0y}^2 + B_{0z}^2}{2\mu_0}, \tag{10}$$

where p_0 is a constant of integration.

The resistive current-sheet structure described by (8) and (9) has a characteristic width of the order of the resistive length

$$a = (\mu_0 \sigma c_1)^{-\frac{1}{2}}, \tag{11}$$

which is obtained by equating the convective flow speed $c_1 a$ to the diffusion speed $(\mu_0 \sigma a)^{-1}$. A basic property of the current sheet obtained from (8) and (9) is that the smaller the flow rate, i.e. the smaller the value of c_1, the thicker will be the current sheet. The odd and even solutions of (8) and (9) can be combined in various ways in order to produce the behaviour of B_{0y} and B_{0z} in the sheet. For our purpose it will suffice to use only the odd solution for B_{0y}, which was shown by Sonnerup & Priest (1975) to be

$$B_{0y} = B_{\max} \operatorname{erf}[(\tfrac{1}{2}\mu_0 \sigma c_1)^{\frac{1}{2}} x], \tag{12}$$

where $\pm B_{\max}$ is the magnetic field at $x = \pm \infty$. The analysis will be valid for all B_{0z} satisfying (9). The general solution for B_{0z} has been shown by Sonnerup & Priest (1975) to be

$$B_{0z} = B_{0z}(0) I(x) + \frac{dB_{0z}}{dx}(0) I(x) \int_0^x \frac{d\xi}{I(\xi)}, \tag{13}$$

where $\qquad\qquad I(\xi) = \exp(-\tfrac{1}{2}c_1 \mu_0 \sigma \xi^2).$

The resulting equilibrium plasma flow and B_{0y}, the antiparallel part of the magnetic field, are shown in figure 1. The even and odd solutions of (13) are shown in figure 8. Note that these B_{0z} solutions vanish as $|x| \to \infty$.

3. Linear perturbations

Returning to (1)–(3), we now introduce small perturbations $\mathbf{v}_1$ and $\mathbf{B}_1$ in the velocity and magnetic field so that

$$\mathbf{v} = \mathbf{v}_0 + \mathbf{v}_1(x, y, t),$$

$$\mathbf{B} = \mathbf{B}_0 + \mathbf{B}_1(x, y, t).$$

Note that these perturbations are taken to be independent of the co-ordinate z. Thus the wave vector of the tearing mode is assumed to be along the y axis.

Equation (1) is satisfied identically by writing

$$\mathbf{v}_1 = \nabla\psi \times \hat{z} + \hat{z} v_{1z}(x, y, t), \tag{14}$$

where ψ is the stream function for the x and y components of $\mathbf{v}_1$.

The pressure may be eliminated from the problem by taking the curl of (2), the result being

$$\frac{\partial \Omega}{\partial t} - \nabla \times (\mathbf{v} \times \Omega) = \frac{1}{\mu_0 \rho} \nabla \times [(\nabla \times \mathbf{B}) \times \mathbf{B}] + \frac{\eta}{\rho} \nabla^2 \Omega, \tag{15}$$

where Ω is the vorticity, i.e.

$$\Omega \equiv \nabla \times \mathbf{v} = \nabla \times \mathbf{v}_1 = \nabla v_{1z} \times \hat{z} - \hat{z} \nabla^2 \psi. \tag{16}$$

The last two equalities in (16) follow from the fact that $\nabla \times \mathbf{v}_0 = 0$ and from (14) respectively.

We now examine the z component of the vorticity equation (15), and the x component of the induction equation (3). The linearized versions of these equations are

$$\left(\frac{\partial}{\partial t} - c_1 - c_1 x \frac{\partial}{\partial x} - \frac{\eta}{\rho} \nabla^2\right) \nabla^2 \psi = \frac{B_{0y}}{\mu_0 \rho}\left(\nabla^2 - \frac{1}{B_{0y}} \frac{d^2 B_{0y}}{dx^2}\right) B_{1x} \tag{17}$$

and

$$\left(\frac{\partial}{\partial t} + c_1 - c_1 x \frac{\partial}{\partial x} - \frac{1}{\mu_0 \sigma} \nabla^2\right) B_{1x} = B_{0y} \frac{\partial^2 \psi}{\partial y^2} \tag{18}$$

respectively. It should be noted that the only perturbation quantities contained in the above equations are ψ and B_{1x}. Thus we see that it will suffice to analyse these two equations to determine the evolution of the perturbations. Once ψ and B_{1x} are known, the perturbed quantities v_{1z} and B_{1z} may subsequently be obtained from the z components of (2) and (3), namely

$$\left(\frac{\partial}{\partial t} + c_1 - c_1 x \frac{\partial}{\partial x} - \frac{\eta}{\rho} \nabla^2\right) v_{1z} = \frac{1}{\mu_0 \rho}\left(B_{0y} \frac{\partial B_{1z}}{\partial y} + B_{1x} \frac{dB_{0z}}{dx}\right) \tag{19}$$

$$\left(\frac{\partial}{\partial t} - c_1 - c_1 x \frac{\partial}{\partial x} - \frac{1}{\mu_0 \sigma} \nabla^2\right) B_{1z} = B_{0y} \frac{\partial v_{1z}}{\partial y} - \frac{\partial \psi}{\partial y} \frac{dB_{0z}}{dx}. \tag{20}$$

It should be noted that B_{0z} does not enter into (17) and (18); thus it does not play a role in driving the instability. It does, however, entrain v_{1z} and B_{1z} via (19) and (20). For $B_{0z} = 0$ the appropriate solutions of these latter equations are $v_{1z} = 0$ and $B_{1z} = 0$.

Solutions to (17)–(20) are now sought in the form

$$
\begin{Bmatrix} \psi \\ B_{1x} \\ v_{1x} \\ B_{1z} \end{Bmatrix} = \begin{Bmatrix} \psi(x) \\ B_{1x}(x) \\ v_{1x}(x) \\ B_{1z}(x) \end{Bmatrix} \exp{(iky + \gamma t)}, \tag{21}
$$

where k and γ are the wavenumber and growth rate respectively. Substitution of these expressions into (17)–(20) gives

$$
\left[\gamma - c_1 - c_1 x \frac{d}{dx} - \frac{\eta}{\rho} \left(\frac{d^2}{dx^2} - k^2 \right) \right] \left(\frac{d^2}{dx^2} - k^2 \right) \psi = \frac{B_{0y}}{\mu_0 \rho} \left(\frac{d^2}{dx^2} - k^2 - \frac{1}{B_{0y}} \frac{d^2 B_{0y}}{dx^2} \right) B_{1x}, \tag{22}
$$

$$
\left[\gamma + c_1 - c_1 x \frac{d}{dx} - \frac{1}{\mu_0 \rho} \left(\frac{d^2}{dx^2} - k^2 \right) \right] B_{1x} = -B_{0y} k^2 \psi, \tag{23}
$$

$$
\left[\gamma + c_1 - c_1 x \frac{d}{dx} - \frac{\eta}{\rho} \left(\frac{d^2}{dx^2} - k^2 \right) \right] v_{1z} = \frac{1}{\mu_0 \rho} \left(ik B_{0y} B_{1z} + B_{1x} \frac{dB_{0z}}{dx} \right), \tag{24}
$$

$$
\left[\gamma - c_1 - c_1 x \frac{d}{dx} - \frac{1}{\mu_0 \sigma} \left(\frac{d^2}{dx^2} - k^2 \right) \right] B_{1z} = ik \left(B_{0y} v_{1z} - \psi \frac{dB_{0z}}{dx} \right). \tag{25}
$$

We now non-dimensionalize (22)–(25) by introducing the following dimensionless variables:

$$
x^* = \frac{x}{a}, \quad k^* = ka, \quad \gamma^* = \frac{\gamma}{c_1},
$$

$$
B_{0y}^* = \frac{B_{0y}}{B_{max}}, \quad B_{0z}^* = \frac{B_{0z}}{B_{max}},
$$

$$
\psi^* = \frac{\psi}{v_A a}, \quad v_{1z}^* = \frac{v_{1z}}{v_A},
$$

$$
B_{1x}^* = \frac{B_{1x}}{B_{max}}, \quad B_{1z}^* = \frac{iB_{1z}}{B_{max}},
$$

$$
S = \mu_0 \sigma a v_A = \frac{v_A}{c_1 a} = v_A \left(\frac{\mu_0 \sigma}{c_1} \right)^{\frac{1}{2}},
$$

$$
Re = \frac{c_1 a^2 \rho}{\eta} = \frac{\rho}{\mu_0 \sigma \eta},
$$

$$
v_A = \frac{B_{max}}{(\mu_0 \rho)^{\frac{1}{2}}}.
$$

Here a is the resistive length given by (11), v_A is the Alfvén speed based on the maximum magnetic field B_{max}, and $c_1 a$ is the characteristic diffusion speed. Thus the quantity S, known as the Lundquist number, is the magnetic Reynolds number $\mu_0 \sigma a v_A$ based on the Alfvén speed and the diffusion length. It should also be noted that $S = 1/M_A$, where M_A is the Alfvén Mach number

at the edges of the current sheet (i.e. at $x = \pm a$). The quantity Re is the viscous Reynolds number based on the characteristic diffusion speed and the diffusion length. Finally, the renormalization of B_{1z} is such that it is phase-shifted by $90°$ relative to the other perturbed quantities.

Substitution of the above expressions into (22)–(25) gives

$$\left[\gamma^* - 1 - x^* \frac{d}{dx^*} - \frac{1}{Re}\left(\frac{d^2}{dx^{*2}} - k^{*2}\right)\right]\left(\frac{d^2}{dx^{*2}} - k^{*2}\right)\psi^*$$

$$= SB_{0y}^*\left(\frac{d^2}{dx^{*2}} - k^{*2} - \frac{1}{B_{0y}^*}\frac{d^2 B_{0y}^*}{dx^{*2}}\right)B_{1x}^*, \quad (26)$$

$$\left(\gamma^* + 1 - x^* \frac{d}{dx^*} - \frac{d^2}{dx^{*2}} + k^{*2}\right)B_{1x}^* = -SB_{0y}^* k^{*2}\psi^*, \quad (27)$$

$$\left[\gamma^* + 1 - x^* \frac{d}{dx^*} - \frac{1}{Re}\left(\frac{d^2}{dx^{*2}} - k^{*2}\right)\right]v_{1z}^* = S\left(kB_{0y}^* B_{1z}^* + B_{1x}^* \frac{dB_{0z}^*}{dx^*}\right), \quad (28)$$

$$\left(\gamma^* - 1 - x^* \frac{d}{dx^*} - \frac{d^2}{dx^{*2}} + k^{*2}\right)B_{1z}^* = -Sk^*\left(B_{0y}^* v_{1z}^* - \psi^* \frac{dB_{0z}^*}{dx}\right), \quad (29)$$

while the equilibrium magnetic field profiles, given by (12) and (13), become

$$B_{0y}^* = \mathrm{erf}(2^{-\frac{1}{2}}x^*), \quad (30)$$

$$B_{0z}^* = B_{0z}^*(0)\exp\left(-\tfrac{1}{2}x^{*2}\right) + \frac{dB_{0z}^*}{dx^*}(0)\exp\left(-\tfrac{1}{2}x^{*2}\right)\int_0^{x^*} d\xi \exp\left(\tfrac{1}{2}\xi^2\right). \quad (31)$$

The coupled equations (26)–(29) describe all small-amplitude MHD wave modes of the current sheet that have their propagation vector along the y direction. We shall examine only the tearing mode, for which the amplitudes $B_{1x}^*(x^*)$ and $\psi^*(x^*)$ are respectively even and odd functions of x^*, and for which these quantities decay rapidly with increasing distance $|x^*|$ from the centre of the current sheet. The parities of v_{1z} and B_{1z}, on the other hand, depend on B_{0z}. In particular, B_{1z} has the same parity as B_{0z}, whereas v_{1z} has the opposite parity. The perturbed quantities v_{1z} and B_{1z} are also required to vanish at large distance. The procedure for solving (26)–(29) is as follows. Equations (26) and (27) are not coupled to the other equations, and may be solved for γ^*, $B_{1x}^*(x^*)$ and $\gamma^*(x^*)$ first. Solutions for $v_{1z}^*(x^*)$ and $B_{1z}^*(x^*)$ are subsequently obtained from (28) and (29).

In this paper we determine the largest real growth rates of the tearing mode by a trial-and-error method of solution. In the case analysed by Furth *et al.* (1963) it was determined that no overstable tearing modes occur. Although the eigenvalue we find is purely real and agrees with the results of Furth *et al.* for large S, we have not found a way to prove rigorously that the eigenvalue with the largest real part is purely real. The existence of overstable modes therefore remains an open question in the case investigated here.

4. Method of solution

In contrast with the standard boundary-layer approach (Furth *et al.* 1963), which involves matching of solutions from an outer and an inner region, we solve (26)–(29) directly over the entire region. This approach allows us to

investigate the entire range of Lundquist number S, in particular values of S of order unity. Since only the odd solutions for $\psi^*(x^*)$ and the even solutions for $B_{1x}^*(x^*)$ are sought, the equations need only be solved over half of the range of x^*, for example for $x^* \geqslant 0$. The following boundary conditions are imposed when solving (26) and (27):

$$\left.\begin{array}{ll} \psi^* = \psi^{*''} = 0, & B_{1x}^* = 1 \quad \text{at} \quad x^* = 0, \\ \psi^* = \psi^{*''} = B_{1x}^* \to 0 & \text{as} \quad x^* \to \infty. \end{array}\right\} \tag{32}$$

The growth rate γ^* is then determined by requiring the solution for $B_{1x}^*(x^*)$ to be an even function of x^*; that is, $B_{1x}^{*'}(x^* = 0) = 0$. The method for obtaining the eigenvalue γ^* is as follows: we start with a trial value of γ^*; the value of $B_{1x}^{*'}(x^* = 0)$ is then obtained by solving (26) and (27). In general, $B_{1x}^{*'}(x^* = 0)$ does not vanish. The value of γ^* is subsequently adjusted until $B_{1x}^{*'}(x^* = 0)$ becomes zero. The resulting γ^*, ψ^* and B_{1x}^* are then the eigenvalue and eigenfunctions of the tearing mode. The method is somewhat similar to that used by Wesson (1966).

Once γ^*, $B_{1x}^*(x^*)$ and $\psi^*(x^*)$ have been determined, one can then proceed to obtain solutions for $v_{1z}^*(x^*)$ and $B_{1z}^*(x^*)$ from (28) and (29), for a given $B_{0z}^*(x^*)$ satisfying (9), subject to the condition that these perturbed quantities vanish as $|x^*| \to \infty$. The magnitudes of $v_{1z}^*(x^*)$ and $B_{1z}^*(x^*)$ are then determined uniquely by the solutions for ψ^*, B_{1x}^*, γ^* and B_{0z}^*.

The coupled ordinary differential equations (26)–(29) are solved using a finite-difference method with variable mesh size. A large number of computational meshes are concentrated near $x^* = 0$, where the solutions of ψ^*; B_{1x}^*, v_{1z}^* and B_{1z}^* display their steepest gradients. In the actual calculation the outer boundary x_∞ is located at large but finite distance from the origin. The choice of x_∞ is such that its location does not affect the resulting γ^*.

5. Results

The growth rate and the eigenmode structure described by $\psi^*(x^*)$, $B_{1x}^*(x^*)$, $v_{1z}^*(x^*)$ and $B_{1z}^*(x^*)$ depend on the parameters S, Re and k^*. Figure 2 displays the dependence of the normalized growth rate γ^* on the normalized wavenumber k^* for several values of the magnetic Reynolds number S and for large viscous Reynolds number ($Re = 10^5$). For each S there is a maximum growth rate γ_{max}^* and a corresponding wavenumber k_{max}^*. This maximum growth rate occurs at longer wavelength (smaller wavenumber) for larger S. For $S < S_{critical} \approx 12\cdot25$ the maximum growth rates are negative, i.e. all perturbations are damped. For $S > S_{critical}$ the unstable regime falls between a large-wavenumber k_{upper}^* (short-wavelength) marginal state ($\gamma^* = 0$) and a small-wavenumber k_{lower}^* (long-wavelength) marginal state. The dependence of k_{upper}^*, k_{lower}^*, and k_{max}^* on S is shown in figure 3. The existence of a long-wavelength marginal state may also be deduced by examining the governing equations in the limit $k^* = 0$. In this limit (27) becomes

$$\frac{d^2 B^*}{dx^{*2}} + x^* \frac{dB^*}{dx^*} - (\gamma^* + 1) B^* = 0. \tag{33}$$

This equation admits solutions that are even functions of x^* and that vanish as $|x^*| \to \infty$ if and only if $\gamma^* + 1$ is negative, i.e. only if $\gamma^* < -1$. Thus the
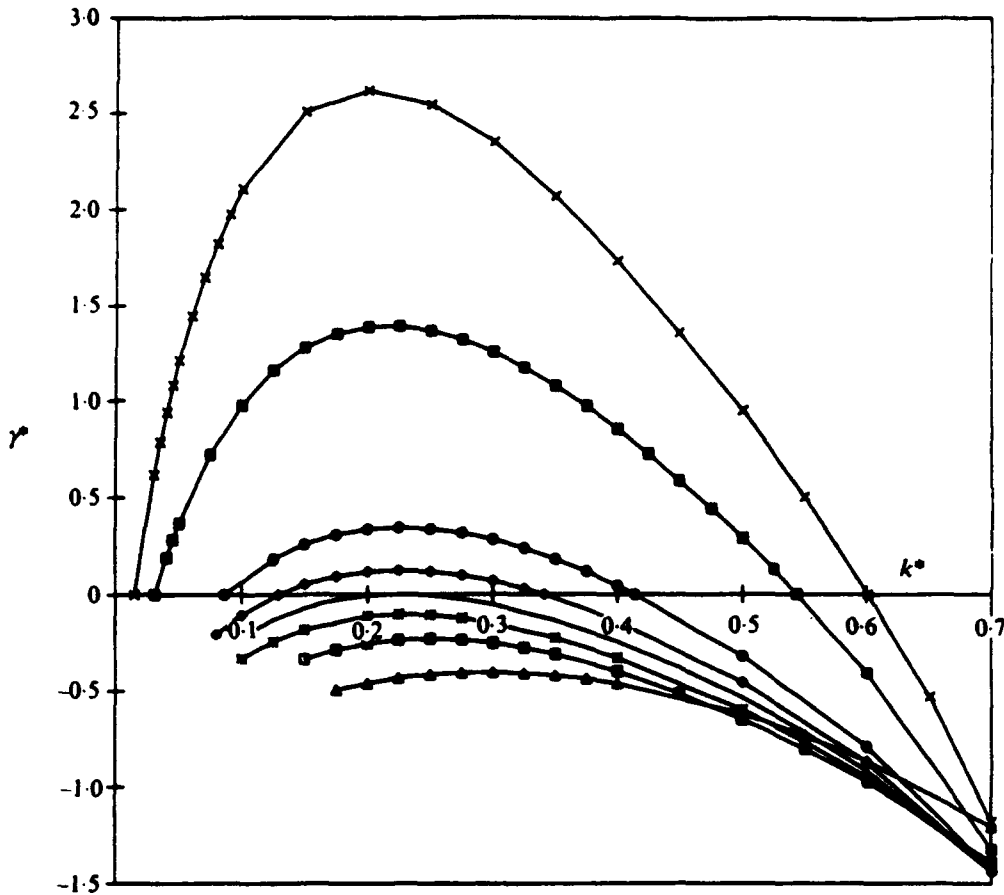
FIGURE 2. Normalized growth rate $\gamma^* = \gamma/c_1$ as a function of normalized wavenumber $k^* = ka$ for Lundquist numbers $S = 5$ ($\triangle$—$\triangle$), 7·5 ($\square$—$\square$), 10 ($\blacksquare$—$\blacksquare$), 12·25 (——), 15 ($\diamond$—$\diamond$), 20 ($\bigcirc$—$\bigcirc$), 50 ($\blacksquare$—$\blacksquare$) and 100 ($\times$—$\times$) and for viscous Reynolds number $Re = 10^5$. The growth rates are negative for $S < 12·25$.

configuration is stable for $k^* = 0$. Since (for sufficiently large S) it is unstable for some k^*, a marginal state must exist at long, but finite wavelength.

Figure 3 shows again that the unstable regime narrows as S decreases and converges to a point as S reaches $S_{critical}$. Below $S_{critical}$ the current sheet is stable to tearing-mode perturbations. For large S, k^*_{upper} and k^*_{lower} asymptotically approach 0·733 and zero respectively, while k^*_{max} obeys approximately the following relation:

$$k^*_{max} \approx 0·91 S^{-0.245} \quad (10^4 < S < 5 \times 10^5).\qquad(34)$$

It should be pointed out that the asymptotic value of k^*_{upper} may be obtained by performing standard boundary-layer analysis of the type first performed by Furth *et al.* (1963) for a hyperbolic tangent magnetic field profile. In that analysis the short-wavelength marginal state is found by setting $\Delta'_{outer}(k^*_{upper}) = 0$, where Δ'_{outer} is the jump in $B^{*-1} \partial B^*/\partial x^*$ of the outer solution across the singular layer. Our boundary-layer analysis for an error-function magnetic field profile gives $k^*_{upper} = 0·733$.

Figures 4(a, b) show the maximum growth rate γ^*_{max} as a function of S for $S \geqslant 100$ and $S \leqslant 100$ respectively. For large S the curve is almost a straight line on a log–log scale, and may be approximated by

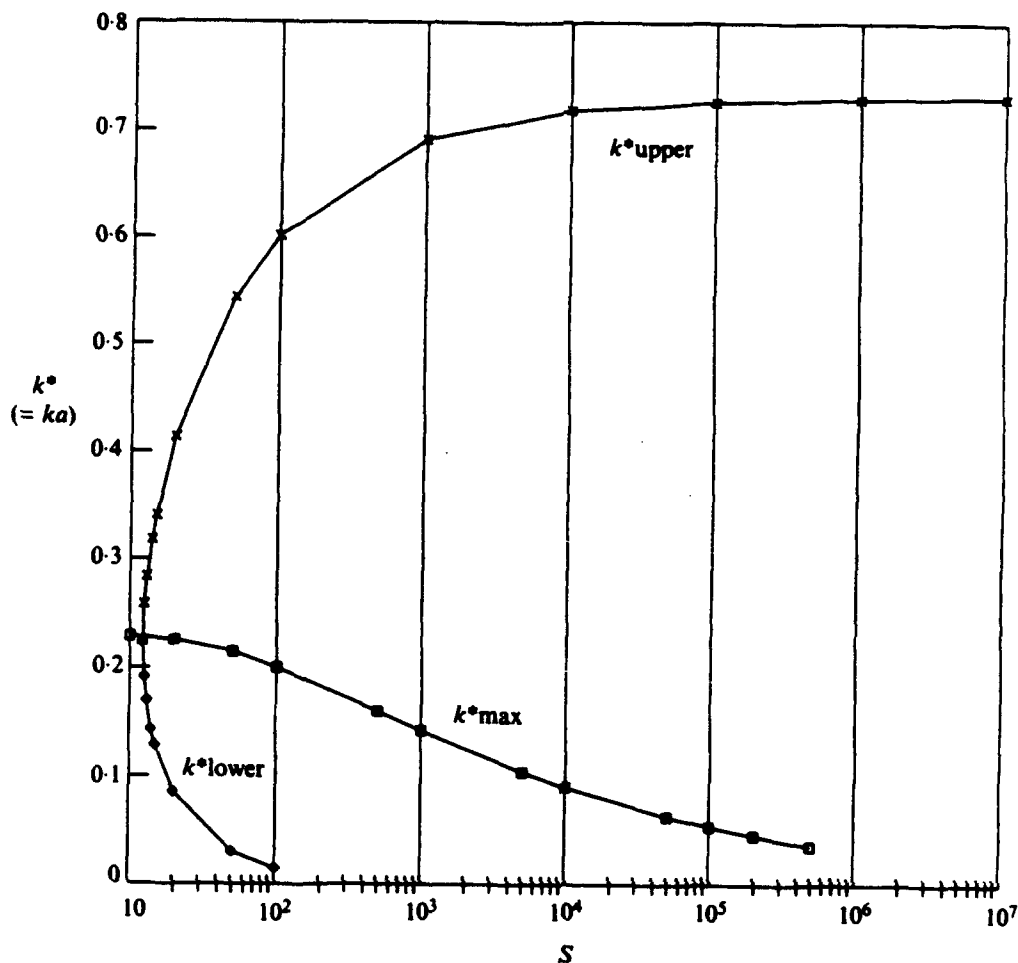$$\gamma^*_{max} \approx 0·39 S^{0.508} \quad (10^4 < S < 5 \times 10^5).\qquad(35)$$

FIGURE 3. Wavenumbers k^*_{max} of fastest growth, k^*_{upper} of short-wavelength marginal state and k^*_{lower} of long-wavelength marginal state as functions of Lundquist number $S = \mu_0 \sigma a v_A$ for viscous Reynolds number $Re = 10^5$. The unstable k^* regime narrows as S decreases. Below $S_{critical} \approx 12.25$ the current sheet is stable to tearing-mode perturbations. For $S > 10^4$ the k^*_{max} curve may be approximated by $k^*_{max} \approx 0.91 S^{-0.245}$.
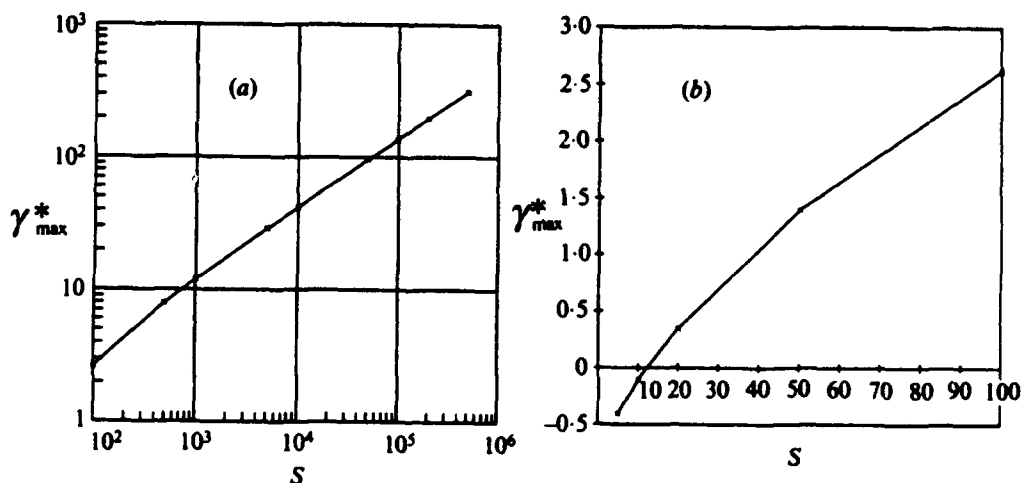

FIGURE 4. Maximum growth rate γ^*_{max} as a function of Lundquist number S for $Re = 10^5$ and $S \geqslant 100$ (a) and $S \leqslant 100$ (b). For $S > 10^4$ the curve may be approximated by $\gamma^*_{max} \approx 0.39 S^{0.508}$.
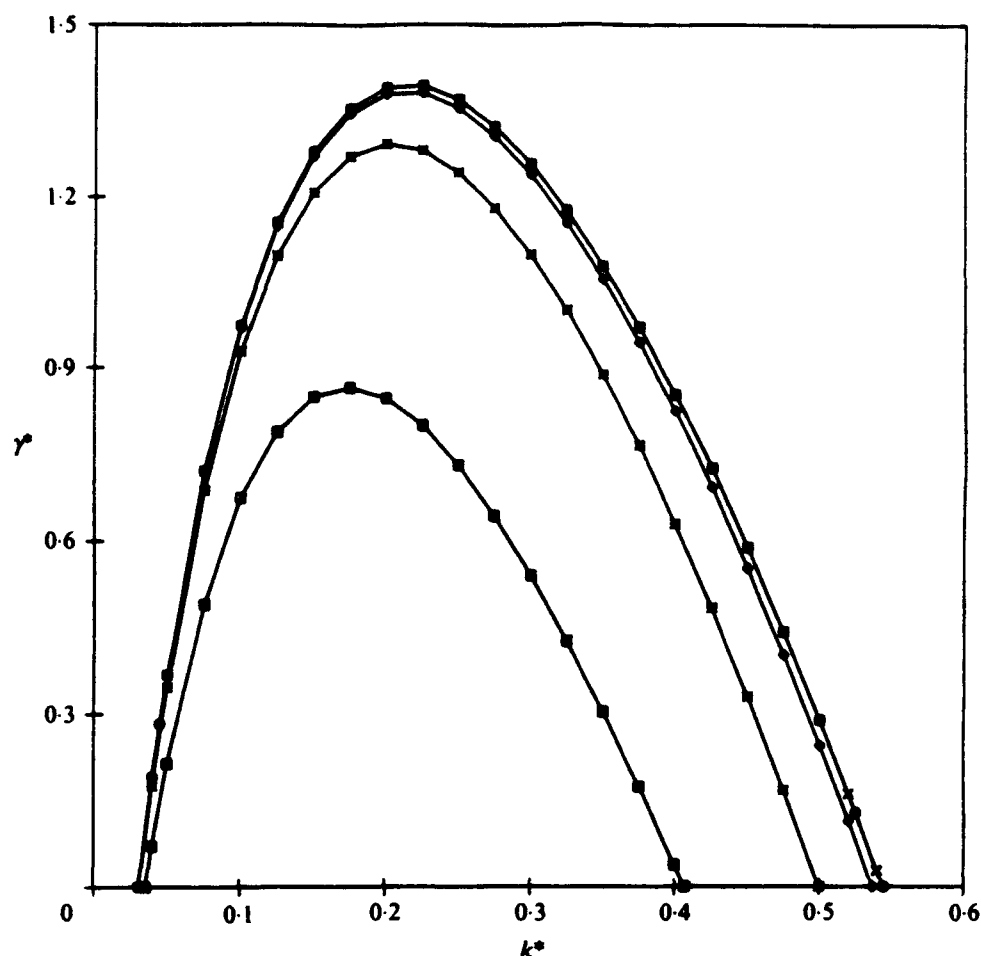
FIGURE 5. Normalized growth rate $\gamma^* = \gamma/c_1$ as a function of normalized wavenumber $k^* = ka$ for viscous Reynolds numbers $Re = 1$ ($\square$—$\square$), 10 ($\blacksquare$—$\blacksquare$), 100 ($\Diamond$—$\Diamond$), 10^4 ($\bigcirc$—$\bigcirc$) and 10^5 ($\times$—$\times$) and for Lundquist number $S = 50$.

The exponents in (34) and (35) are very close to the asymptotic values (as $S \to \infty$) of $\frac{1}{4}$ and $\frac{1}{2}$ respectively, obtained by Furth *et al.* (1963) in their study of the tearing mode without equilibrium flow, indicating that the effect of the equilibrium flow, other than that of determining the current-sheet width, is negligible when S is large. For small S, however, the relation between γ^*_{max} and S differs considerably from (35), and also does not agree with Lee & Fu's (1986) result for low S. In particular, those authors did not find a stable regime for low S.

The dependence of the growth rate on viscosity is illustrated in figures 5 and 6. Figure 5 shows the normalized growth rate γ^* as a function of the viscous Reynolds number Re for $S = 50$. It is seen that the viscosity has a stabilizing effect. This effect is more important at short wavelength (large k^*) and when the viscous Reynolds number Re is small ($Re < 100$). It should also be noted that the fastest-growing wavelength increases with increasing viscosity (decreasing Re). The stabilizing effect of the viscosity may also be seen in figure 6, where $S_{critical}$ is shown as a function of Re. It should be noted that $S_{critical}$ decreases with increasing Re. For $Re > 10^3$, $S_{critical}$ is close to its asymptotic value of 12·25.

In figures 7 (a, b) we show two examples of the eigenmode structure in terms

T. D. Phan and B. U. Ö. Sonnerup
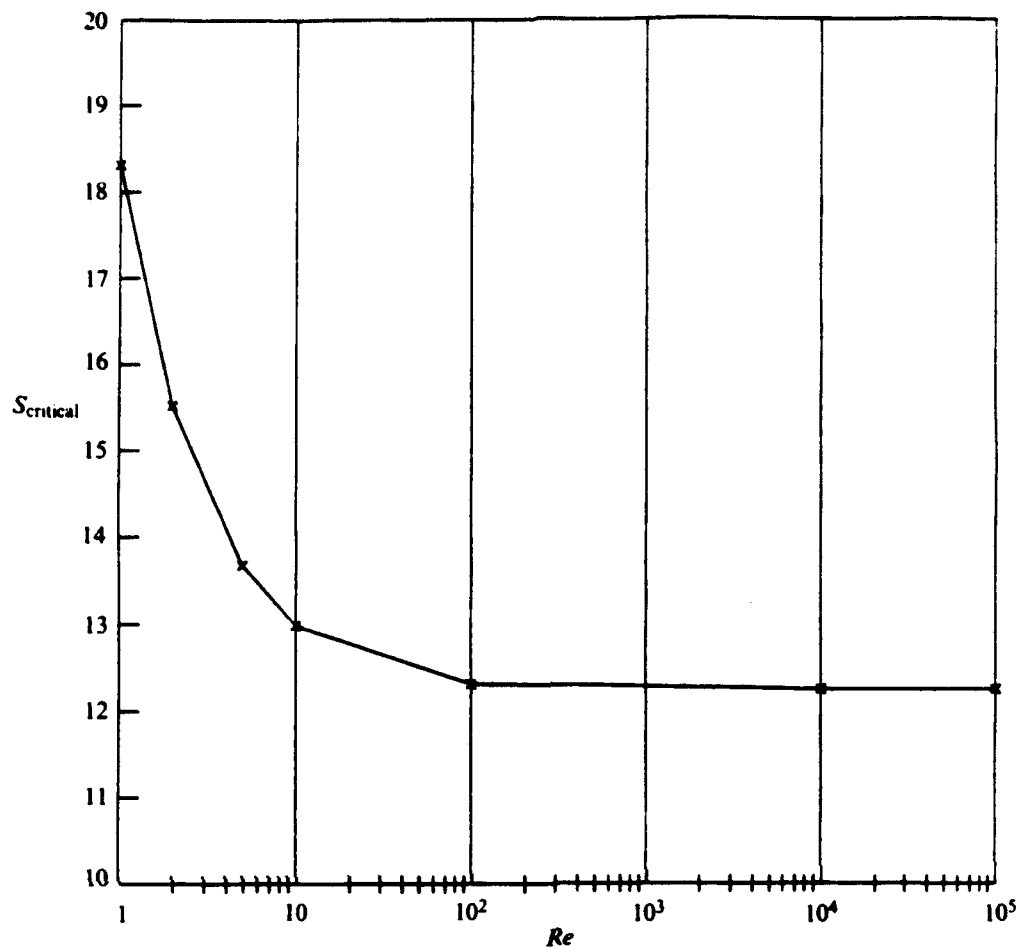
FIGURE 6. S_{critical} as a function of viscous Reynolds number Re.
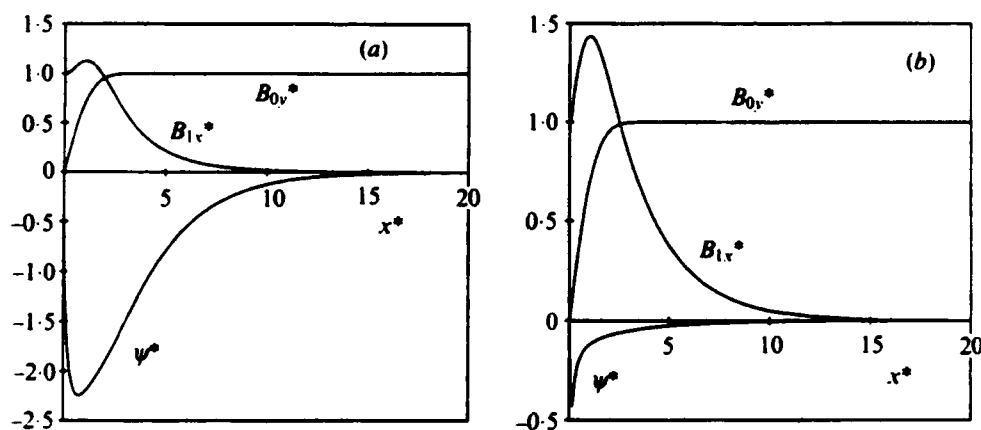
FIGURE 7. Equilibrium magnetic field $B_{0y}^*(x^*)$ and perturbed eigenmodes $\psi^*(x^*)$ and $B_{1x}^*(x^*)$ as functions of $x^* = x/a$ for $Re = 10^5$, $k^* = 0.4$, and (a) $S = 5$ and (b) $S = 1000$.

of $\psi^*(x^*)$ and $B_{1x}^*(x^*)$ for $S = 5$ and 1000 respectively, and for $Re = 10^5$ and $k^* = 0.4$, illustrating the difference in the behaviour of the eigenmodes depending on the S regime. In the $S = 1000$ case the shapes of the eigenmodes are similar to those obtained in previous studies of the tearing mode with high S, and where the effect of resistive decay of the current sheet is neglected (see e.g. Killeen & Shestakov 1978). In particular, an 'inner region' appears that is
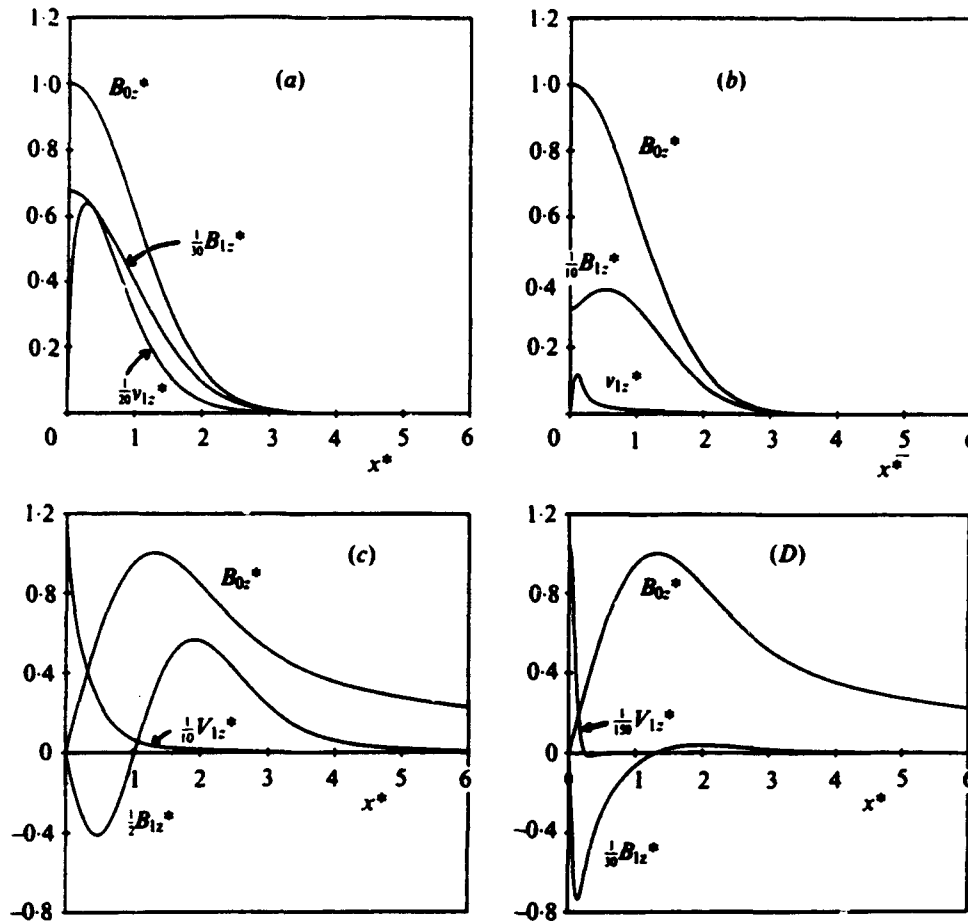
FIGURE 8. Equilibrium magnetic field $B_{0z}^*(x^*)$ and perturbed eigenmodes $v_{1z}^*(x^*)$ and $B_{1z}^*(x^*)$ as functions of $x^* = x/a$ for even (a, b) and odd (c, d) magnetic field B_{0z}^* for $S = 5$ (a, c) and $S = 1000$ (b, d). The viscous Reynolds number and wavenumber are $Re = 10^5$ and $k^* = 0.4$.

much thinner than the current-sheet width. In the $S = 5$ case, as expected, the 'inner region' is comparable to the resistive length. In this regime the results of the previous studies, which excluded the diffusion effect of the equilibrium magnetic field, are not valid. Note in particular that the tearing mode is damped for $S = 5$ even though the curve for $B_{1z}^*(x^*)$ displays the dimple at $x^* = 0$ normally associated with unstable behaviour. For convenient comparison of length scales the equilibrium magnetic field B_{0y}^* is also shown in figure 7.

Figures 8$(a-d)$ display the eigenmode structures in $v_{1z}^*(x^*)$ and $B_{1z}^*(x^*)$ for the same cases as in figure 7, and for a purely even (figures 8a, b) and a purely odd (figures 8c, d) equilibrium magnetic field B_{0z}. For an arbitrary B_{0z} satisfying (9) the resulting eigenmode structures in $v_{1z}^*(x^*)$ and $B_{1z}^*(x^*)$ are linear combinations of the even and odd eigenfunctions shown. Note that the even solutions of v_{1z}^* display large local curvature, for example $x^* = 0$ in figure 8(c). This behaviour is a direct consequence of the large Re value. Note also that the spatial scales are different in figures 7 and 8.

6. Discussion and conclusion

We have examined the linear stability of a current sheet against the tearing mode in the presence of equilibrium stagnation-point flow, the latter being confined to the plane perpendicular to the $\mathbf{k}$ vector of the tearing mode. The entire range of Lundquist numbers S and viscous Reynolds numbers Re, where $S = \mu_0 \sigma a v_A$ and $Re = c_1 a^2 \rho / \eta$, has been explored. Our main findings can be summarized as follows.

(i) Long-wavelength perturbations are stabilized by the stagnation-point flow so that the unstable regime, if it exists, falls between a short-wavelength and a long-wavelength marginal state.

(ii) For large S ($> 10^4$) the Furth _et al._ (1963) scaling of the growth rate, $\gamma_{max}^* \propto S^{\frac{1}{2}}$, and of the wavenumber at maximum growth rate, $k_{max}^* \propto S^{-\frac{1}{4}}$, are approximately recovered, indicating that the effect of the equilibrium flow, other than that of determining the current-sheet width, is small when S is large. In dimensional form the growth rate and the wavenumber can be expressed as $\gamma_{max} \propto v_A^{\frac{1}{2}} c_1^{\frac{1}{4}} \sigma^{\frac{1}{4}}$ and $k_{max} \propto v_A^{-\frac{1}{4}} c_1^{\frac{1}{4}} \sigma^{\frac{1}{4}}$ respectively. These relationships show that a faster flow (larger c_1) and/or a larger conductivity σ reduce the current-sheet width, and thereby enhance the growth rate of the instability, at the same time decreasing the wavelength at which maximum growth occurs.

(iii) For small S the stabilizing effect of the equilibrium flow is evident. When $S < S_{critical} \approx 12.25$, the current sheet is completely stable to all tearing-mode perturbations, a result not obtained in the absence of the equilibrium flow.

(iv) The viscosity has the effect of reducing the growth rate. This effect is more noticeable at short wavelengths and in flows with small viscous Reynolds number Re. As a result, $S_{critical}$ increases with smaller Re.

(v) The mode structure in the (x, y) plane and the growth rate of the instability remain unaffected by the presence of a non-zero magnetic field component $B_{0z}(x)$ satisfying (9). But when $B_{0z} \neq 0$ the mode structure includes perturbations in the field and flow components in the z direction.

The main difference between our study and previous investigations of the resistive tearing mode is that we have started from an exact equilibrium current-sheet configuration in which the resistive widening of the sheet is exactly counterbalanced by the stagnation-point flow. It is this feature of the unperturbed current layer that allows us to investigate the entire range of Lundquist numbers S, in particular values of S of order unity. Our results for low S differ significantly from those obtained by Lee & Fu (1986), who did not use an exact unperturbed equilibrium in their analysis.

It may be thought that the flow geometry studied in this paper has limited practical applications. However, it has been argued (Pudovkin & Semenov 1977 _a_, _b_; Sonnerup 1980) that, in the absence of reconnection, steady-state flow of a magnetized highly conducting plasma past a diamagnetic object will lead to the formation of a stagnation line rather than a stagnation point on the upstream face of the object. This stagnation line is aligned with the magnetic field embedded in the impinging plasma flow, so that the unperturbed flow configuration becomes similar to that examined here. One application may be the flow of solar-wind plasma past the earth's magnetosphere, where a stagnation line may be formed near the subsolar point of the magnetopause. To apply our results to the magnetopause, we must estimate the Lundquist

number based on the thickness of the magnetopause current layer. If we adopt the value of $(\mu_0 \sigma)^{-1} = 10^9$ s m^{-2} (see e.g. Sckopke *et al.* 1981) as an upper limit for the resistive diffusion coefficient, and use lower limits of 100 km for the thickness of the current layer and 100 km s^{-1} for the Alfvén speed just outside the current layer, we obtain a lower limit of $S \equiv \mu_0 \sigma a v_A \approx 10$. This value is consistent with Lee & Fu's (1986) estimate of $2 < S < 100$. The fact that in our study the current sheet is found to be stable for $S < 12\cdot25$ therefore suggests that the magnetopause current layer may at times be stable or only weakly unstable to tearing-mode perturbations.

REFERENCES

BESSER, B. P., BIERNAT, H. K. & RIJNBEEK, R. P. 1990 *Planet. Space Sci.* **38**, 411.

BULANOV, S. V., SYROVATSKY, S. I. & SAKAI, J. 1978 *JETP Lett.* **28**, 177.

CHEN, X. L. & MORRISON, P. J. 1990 *Phys. Fluids* B **2**, 495.

CROSS, M. A. & VAN HOVEN, G. 1971 *Phys. Rev.* A **4**, 2347.

DOBROTT, D., PRAGER, S. C. & TAYLOR, J. B. 1977 *Phys. Fluids* **20**, 1850.

EINAUDI, G. & RUBINI, F. 1986 *Phys. Fluids* **29**, 2563.

EINAUDI, G. & RUBINI, F. 1989 *Phys. Fluids* B **1**, 2224.

FORBES, T. G. & PRIEST, E. R. 1987 *Rev. Geophys.* **25**, 1583.

FURTH, H. P., KILLEEN, J. & ROSENBLUTH, M. N. 1963 *Phys. Fluids* **6**, 459.

KILLEEN, J. & SHESTAKOV, A. I. 1978 *Phys. Fluids* **21**, 1746.

LAVAL, G., PELLAT, R. & VUILLEMIN, M. 1966 *Proceedings of the Conference on Plasma Physics and Controlled Nuclear Fusion*, p. 259. International Atomic Energy Agency.

LEE, L. C. & FU, Z. F. 1986 *J. Geophys. Res.* **91**, 3311.

OFMAN, L., CHEN, X. L. & MORRISON, P. J. 1991 *Phys. Fluids* B **3**, 1364.

PARKER, E. N. 1973 *J. Plasma Phys.* **9**, 49.

PHAN, T. D. & SONNERUP, B. U. Ö. 1990 *J. Plasma Phys.* **44**, 525.

PUDOVKIN, M. I. & SEMENOV, V. S. 1977*a* *Ann. Geophys.* **33**, 423.

PUDOVKIN, M. I. & SEMENOV, V. S. 1977*b* *Ann. Geophys.* **33**, 429.

SCKOPKE, N., PASCHMANN, G., HAERENDEL, G., SONNERUP, B. U. Ö., BAME, S. J., FORBES, T. G., HONES, E. W. & RUSSELL, C. T. 1981 *J. Geophys. Res.* **86**, 2099.

SONNERUP, B. U. Ö. 1979 *Solar System Plasma Physics*, vol. III (ed. L. T. Lanzerotti, C. F. Kennel & E. N. Parker), p. 46. North-Holland.

SONNERUP, B. U. Ö. 1980 *Dynamics of the Magnetosphere* (ed. S. I. Akasofu), p. 77. Reidel.

SONNERUP, B. U. Ö. & PRIEST, E. R. 1975 *J. Plasma Phys.* **14**, 283.

SONNERUP, B. U. Ö. & SAKAI, J.-I. 1981 *EOS Trans. AGU* **62**, 353.

VASYLIUNAS, V. M. 1975 *Rev. Geophys. Space Phys.* **13**, 303.

WESSON, J. 1966 *Nucl. Fusion* **16**, 130.

MAGNETIC FIELD MAXIMA IN THE LOW LATITUDE BOUNDARY LAYER

B. Sonnerup[1] , G. Paschmann[2] , T.-D. Phan[2], and H. Lühr[3]

Abstract. The magnetic field often exhibits a maximum in the Earth's low-latitude boundary layer. We show examples of this behavior, using data from the AMPTE/IRM spacecraft, and argue that two fundamentally distinct causes exist for the excess field: (i) a depression, within the layer, of the population of medium-energy ions of magnetospheric origin; (ii) field curvature effects associated with undulations of the magnetopause itself.

1. Introduction

The frequent presence of a magnetic-field strength maximum near the magnetospheric edge of the magnetopause (MP) has been noted by Neugebauer et al. [1974], Sonnerup and Ledley [1979], and Hall et al. [1991]. Sometimes the region of field enhancement has an inner edge that coincides with the earthward edge of the low-latitude boundary layer (LLBL) and beyond which the field magnitude stays nearly constant at its magnetospheric level; sometimes the field decays from its maximum to its magnetospheric level in a more gradual manner, as one moves from the inner edge of the LLBL into the magnetosphere proper. We shall refer to these two pure classes of field behavior as Type I and Type II, respectively, although we stress that they represent an oversimplification: more commonly, a mixture of the two is seen. At first, the occurrence of field maxima seems paradoxical. After all, the region just earthward of the MP is usually occupied by the LLBL, a narrow region of dense magnetosheath-like plasma flowing along the MP more or less in the antisolar direction. One would expect the diamagnetic effect of this plasma to produce a field depression rather than a field enhancement within the LLBL, a feature that is in fact also seen when the LLBL density is high.

Neugebauer et al. [1974] did not discuss the LLBL but they suggested that the field maxima may be caused by loss of energetic magnetospheric particles, whose gyromotion carry them up to the MP where they escape to the magnetosheath. However, they lacked the instrumentation needed to check this hypothesis. Here, we use data from the AMPTE/IRM spacecraft to demonstrate that field enhancements of Type I are in fact colocated with the LLBL and that the densities of medium-energy magnetospheric ions (9<E<40 keV) and electrons (2<E<40 keV) are indeed depressed in them. Thus there is partial agreement with the Neugebauer et al. explanation: the excess magnetic pressure compensates for the defect in plasma pressure caused by the absence of energetic magnetospheric particles. However, in that explanation, electrons with their much smaller gyroradii should drop out

[1]Dartmouth College, Hanover, NH

[2]Max-Planck-Institut für extraterrestrische Physik, Garching

[3]Technische Universität, Braunschweig

very close to the MP rather than earthward of the inner edge of the LLBL, as we observe them to do. In Type II events, there is a gradual loss of high energy particles (40<E<400 keV) as the MP is approached but no significant loss of medium-energy particles in most of the field-enhancement region.

Using AMPTE/UKS data, Hall et al. [1991] found a minimum in total electron pressure precisely where the magnetic field overshoot occurs: they referred to this region as a "depletion layer" (we reserve this term for the region immediately outside the MP where plasma depletion and an associated field overshoot is sometimes seen). This minimum in electron pressure is a direct result of the coexistence of two electron populations in the LLBL: cool magnetosheath electrons decreasing in density with increasing distance inward from the MP; and hot (but far more tenuous) magnetospheric electrons, decreasing in density with increasing distance outward from the inner edge of the LLBL. We emphasize that the electrons usually only play a minor role in the overall pressure balance across the MP/LLBL: the major contributions to $P_{tot} = (P_\perp + B^2/2\mu_0)$ come from magnetosheath ions, medium-energy magnetospheric ions and the magnetic field. The important difference between Type I and Type II events is that P_{tot} is approximately constant from the magnetosheath through the MP/LLBL into the magnetosphere in Type I whereas a sometimes large maximum in P_{tot} occurs earthward of the MP in Type II. This maximum is caused by excess magnetic pressure.

2. Type I Event

Figure 1 shows a Type I crossing, i.e., a case where the magnetic field overshoot is confined to the LLBL. This inbound pass through the MP/LLBL region on July 3, 1985, took place on the dusk flank of the magnetosphere (1930h LT) near the equatorial plane (-6.9° GSE latitude) at a geocentric distance of 17 R_E. The motion of the MP relative to the spacecraft was complicated. We go through the event backwards, i.e., starting at the right-hand edge of the figure, at 1625 UT, where the spacecraft was in the magnetosphere, in a more or less uniform field of $B \cong 15$ nT ($P_B \cong 0.09$ nPa, panel 6), with total ion density, N_p, (E<40) keV, which is mainly low energy ions) as well as densities of medium-energy ions, N_{2p} (9<E<40 keV), and electrons, N_{2e} (2<E<40 keV), (panel 1) at their magnetospheric levels. The bulk speed, V_p, of the magnetospheric plasma was modest (panel 2), its temperatures, T_p and T_e, were high (panel 3). Going backwards in time, the first indication of the LLBL being approached occurred around 1621:50 UT where N_{2e} and T_e started to drop. At 1621:10 UT, the LLBL proper was entered: N_p increased abruptly, while T_p and T_e dropped equally abruptly to intermediate levels characterizing the LLBL. The medium-energy ion density, N_{2p}, dropped more gradually. The field magnitude, B, rose, also gradually at first, and then more rapidly until a plateau was reached at $B \cong 25$ nT ($P_B \cong 0.25$ nPa, panel 6). The MP encounter occurred at 1619:55 UT. Here B dropped abruptly to less than 5 nT ($P_B < 0.01$ nPa); simultaneously, the field direction changed (panels 4 and 5), T_p and T_e decreased while V_p and N_p both

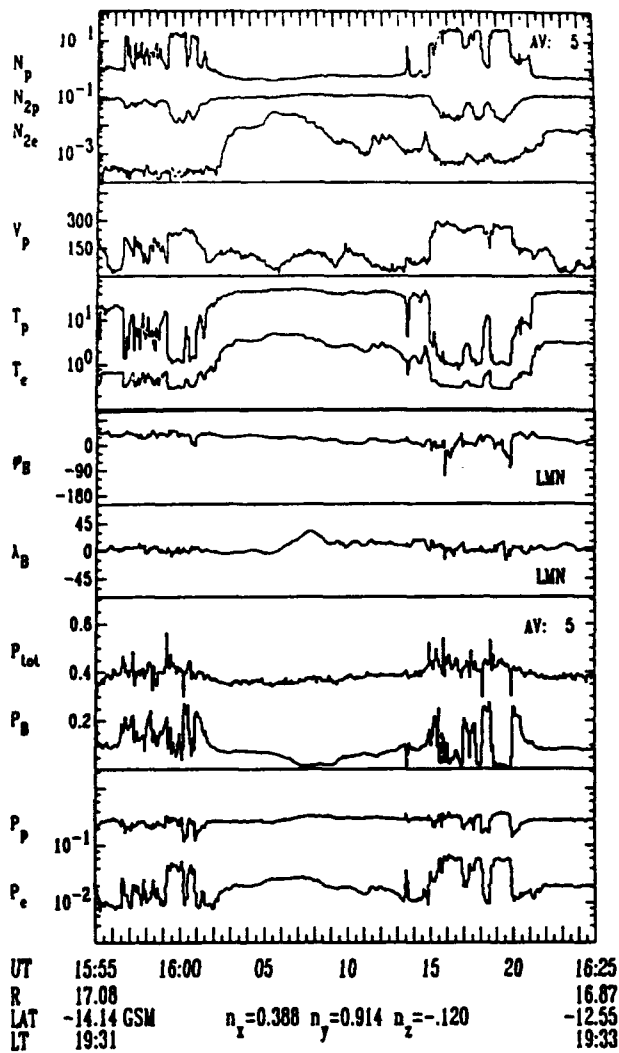**Fig. 1.** AMPTE/IRM data during inbound pass through the MP/LLBL region on July 3, 1985. Panel 1: proton number density, N_P (cm^{-3}; E<40 keV); medium-energy proton and electron number densities, N_{2p} (cm^{-3}; 9<E<40 keV) and N_{2e}(cm^{-3}; 2<E<40 keV). Panel 2: plasma bulk flow speed, V_p (km/s). Panel 3: proton and electron temperatures, T_p and T_e, (10^6°K; E<40K keV). Panels 4 and 5: magnetic field azimuth angle, φ_B, and elevation angle, λ_B, (degrees). Angles refer to boundary-normal coordinates, LMN, with λ = 0 in the MP tangent plane and $\lambda>0$ for an outward field; also, φ_B = 0 along +L and φ_B = 90° along +M. Panel 6: total perpendicular pressure $P_{tot} = P_p + P_e + P_B$ and magnetic pressure $P_B = B^2/2\mu_0$ (nPa). Panel 7: proton and electron perpendicular pressures, P_p and P_e, (nPa; E<40 keV).

increased abruptly to their values in the magnetosheath. Continuing backward in time, several additional full or partial MP crossings occurred: we do not discuss these in detail, except to note the similarity between the MP/LLBL encounter just discussed and that between 1600:50 and 1603:00 UT.

The most remarkable feature in Figure 1 is the approximate constancy, over a 30 minute period, of the total pressure, P_{tot}. (panel 6, upper curve), in spite of large temporal variations in the magnetic pressure (panel 6, lower curve). The large ion (E<40 keV) and electron (E<40 keV) perpendicular pressure variations, P_p and P_e, that compensate for the changes in magnetic pressure are shown explicitly in panel 7. Note the deep minimum in P_e during the LLBL

encounters (at ~1601 UT and ~1620 UT): this is the effect discussed by Hall et al. [1991]. But it is also seen that the dominant effect is the minimum in P_p in the LLBL: the electrons make only a minor contribution to the overall pressure balance. Also, the pressure contribution from high-energy particles (40<E<400 keV), measured by the SULEICA instrument onboard AMPTE/IRM, was negligible [L. Kistler, private communication]. The occasional spikes in the P_{tot} curve (panel 6) are believed to be the result of aliasing associated with different sampling of field and plasma.

In summary, items to note in this event are: (1) colocation of field enhancement region and LLBL; (2) gradually decreasing density of medium-energy ions moving outward from the inner edge of the LLBL; (3) dropout of medium-energy magnetospheric electrons at, or earthward of the inner edge of the LLBL, a dropout that is more pronounced than the decrease in medium-energy magnetospheric ion density; (4) near constancy of total pressure.

3. Type II Event

Figure 2 shows Type II behavior, i.e., magnetic field enhancement in the magnetosphere proper, for the outbound pass of AMPTE/IRM on October 8, 1985. This traversal of the LLBL/MP region occurred near local noon (1120 local time) at -10.8° GSE latitude and at a geocentric distance of about 11 R_E. At the left edge of the diagram (0850 UT), the spacecraft was in the magnetosphere, proceeding outward toward the LLBL. An early gradual drop in electron temperature preceded the LLBL proper but other plasma parameters remained nearly constant there. However, a gradual increase of field magnitude occurred, from 60 nT ($P_B \cong 1.43$ nPa) at 0853 UT to about 70 nT ($P_B \cong 1.95$ nPa) when the LLBL plasma was first encountered, at about 0857:10 UT. At this latter time, N_p started to increase rapidly, while N_{2e} dropped abruptly and N_{2p} more gradually to lower levels, characteristic of the LLBL. There was an associated abrupt drop in T_e whereas T_p decreased more gradually as N_p ramped up from the magnetospheric to the LLBL level. At the end of this ramp, around 0857:45 UT, the field magnitude dropped abruptly; there was little change in the azimuth angle, φ_B, but the elevation angle, λ_B, changed from essentially zero to about +20°.

One may ask whether the spacecraft entered the magnetosheath already at 0857:45 UT, in which case the LLBL would have been traversed in only about 30 seconds. For a low-shear MP the possibility of misinterpreting magnetosheath magnetic discontinuities as MP crossings must be kept in mind. However, in the present case there is evidence to indicate that the spacecraft remained in the LLBL for a long time, namely until about 0923:40 UT when a sudden and substantial change in field angle, φ_B, occurred: in the interval 0857:45-0923:40 UT, N_{2p} and N_{2e}, as well as T_p and T_e remained at levels intermediate between the magnetospheric and the magnetosheath levels, a feature that is commonly seen in the LLBL. Within 10 seconds after 0923:40 UT, N_{2p} and N_{2e} dropped from those intermediate levels to levels characteristic of the magnetosheath with the electron fluxes falling below the detection threshold; there were associated decreases in T_p and T_e as well as changes in the temperature anisotropies of the kind often seen at the MP. If, as we believe, the MP was traversed at 0923:40 UT, it was marked by a substantial velocity peak of nearly 400 km/s compared to a typical magnetosheath level of about 100 km/s and a magnetospheric level of 50 km/s. In fact, throughout a good part of what would then be the LLBL interval, from 0857:45 to 0923:40 UT, V_p exceeded the flow speed in the magnetosheath. Such a long-duration LLBL need not, and
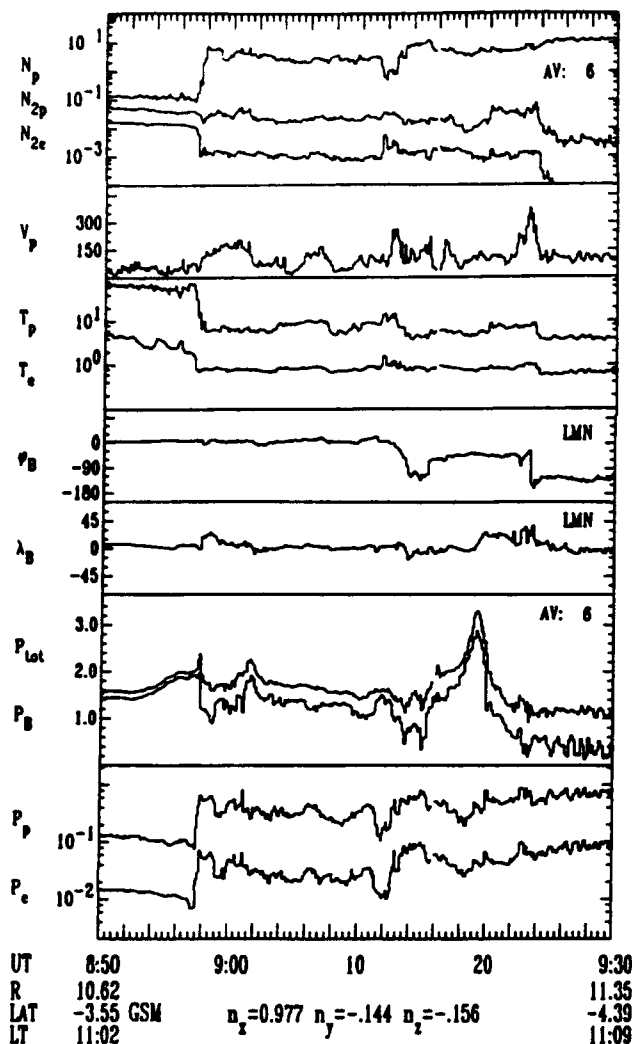
Fig. 2. AMPTE/IRM data during outbound pass through the MP/LLBL region on October 8, 1985; format as in Fig. 1.

probably should not, be interpreted as an indication of a thick layer: there are signs that the MP may have reversed its radial motion soon after 0857:45 UT causing the spacecraft to approach the inner edge of the LLBL around 0901:30 UT. There are also indications of a pair of MP encounters around 0914 UT when a large change in field angle, φ_B, took place. Following that change, a huge field maximum of about 85 nT is seen. It would be difficult to incorporate this feature as a semipermanent part of the LLBL; it seems more likely to have been a temporal effect. Except for this particular structure, it is clear from the figure that there was a substantial diagmagnetic field magnitude depression, relative to the magnetospheric field, over most of the LLBL(0857:45 to 0923:40 UT), but with a pronounced field maximum near its inner edge. This field maximum and the slow rise of the field, starting about 0853 UT, and continuing until the maximum was reached at 0857:45 UT is of principal interest to us.

During the interval 0853-0857:45 UT, the total pressure (panel 6) gradually rose as a direct consequence of the rising magnetic pressure. In this case, there is no indication that decreases in the thermal plasma pressure were present to counterbalance the increasing magnetic pressure: in fact, near the end of this interval, right at the field maximum, the plasma perpendicular pressure started to increase instead. The pressure contribution from high-energy particles (40<E<400

keV), measured by SULEICA, was not negligible for this event: it dropped from about 0.1 nPa prior to 0850 UT to 0.05 nPa at 0855 UT and then to zero at approximately 0856:30 UT. However, this decrease cannot compensate for the increase in P_{tot}, shown in panel 6 of Figure 2, from about 1.6 nPa at 0853 UT to 2.4 nPa at 0857:45 UT. In the regions of depressed magnetic field following after the latter time, the thermal plasma pressure increased a great deal (while the high-energy particle pressure remained zero) but did not fully compensate for the depressed magnetic pressure. An exceptionally large maximum in P_{tot} was associated with the aforementioned large field maximum at 0919:20 UT. This is an indication of two or three-dimensional structure and/or temporal evolution associated with this field structure.

The most significant features of this traversal are: (1) gradual field enhancement in the magnetosphere prior to the spacecraft entering the LLBL, with the field maximum located at the inner edge of that layer; (2) nearly constant level of the medium-energy ion density, N_{2p}, in the magnetospheric part of the field enhancement region; (3) partial dropout of medium-energy magnetospheric electrons and an associated abrupt drop in electron temperature near the inner edge of the LLBL; (4) a smaller drop in N_{2p} at the inner edge of the LLBL; (5) absence of total pressure balance in the interval 0853-0857:45 UT.

4. Discussion

The near constancy of total pressure in Type I MP/LLBL crossings indicates that field curvature effects and temporal effects play little role in them. The principal item that needs to be examined is the cause of the depressed densities, N_{2p} and N_{2e}, of medium-energy magnetospheric ions and electrons in the LLBL. It is the depression in N_{2p} that produces the main defect in total plasma pressure in the LLBL, a defect that is in turn compensated for by excess magnetic pressure in that layer. Although we agree with Neugebauer et al. [1974] that particles whose guiding centers are brought within one gyroradius of the magnetopause may get lost to the magnetosheath, and although the LLBL could perhaps at times be as thin as a typical medium-energy ion gyroradius, we do not see how the depression in the medium-energy electron density, N_{2e}, which started substantially earthward of the LLBL in the July 3 event but which more typically marks its inner edge, can be accounted for in this manner. Possible explanations for this behavior of N_{2e} are:

(a) Energetic particle diffusion from the magnetosphere towards the MP could be an important effect. From the considerably steeper N_p profiles it would appear that inward diffusion of magnetosheath protons is a much less effective process than outward diffusion of more energetic particles.

(b) Pitch-angle scattering with associated particle precipitation could be responsible for the depletion of N_{2e} and N_{2p} in the LLBL and perhaps for the depressed (relative to the magnetosheath) thermal plasma density, N_p, there.

(c) The LLBL could be on open field lines, i.e., field lines with only one end in the ionosphere.

(d) Magnetosheath plasma could have entered onto field lines in the LLBL at some upstream location where those field lines were temporarily opened by reconnection, allowing magnetosheath plasma to enter onto them and energetic magnetospheric ions and electrons to be drained from them. Subsequently, the field lines closed again, through a second reconnection process [Kan, 1988], and were then transported tailward along the magnetopause to the observation site. In an alternate scenario [Cowley, 1981], the entire LLBL is incorporated into the magnetosphere by cusp reconnection during periods of northward interplanetary magnetic field; if

formed in this manner the LLBL would be devoid, or partially devoid of energetic magnetospheric particles.

(e) Magnetosheath plasma could have moved onto closed magnetospheric field lines by $E \times B$ drift in some localized region where the magnetosheath field was aligned with the magnetospheric field. In such a process, the energetic magnetospheric particle population would be pushed out of the way, also as a result of $E \times B$ drift.

Without additional information, we cannot eliminate any of these possibilities. However, if (c), (d) or (e) were applicable in their purest form, i.e., without the presence of particle diffusion, then the density profiles N_{2p} and N_{2e} at the inner edge of the LLBL would be much steeper than they are observed to be. For this reason, we believe that diffusion must play a significant role, although it seems likely to occur in combination with one of the other effects. Also, the steepness of the N_p profiles suggests that the diffusion is by microscopic rather than macroscopic turbulence, since the latter would operate equally as effectively on the low energy LLBL plasma as on the more energetic particles.

Characteristic features of Type II traversals of the MP/LLBL region are that the magnetic-field magnitude is enhanced well within the magnetosphere proper and that the total pressure, P_{tot}, is not constant in this region. We argue that these effects are caused by field-line curvature, presumably associated with waves or bulges on the magnetopause moving past the spacecraft. It is well known that short-duration overshoots in P_{tot} occur during flux transfer events (FTEs). The explanation for this effect is the draping of ambient magnetic-field lines around an elongated MP structure such as a flux tube (along with twisting of the field within the tube). Farrugia et al. [1987] modeled the draping effect in terms of a vacuum field, generated by the superposition of the uniform ambient field component, B_{ox},
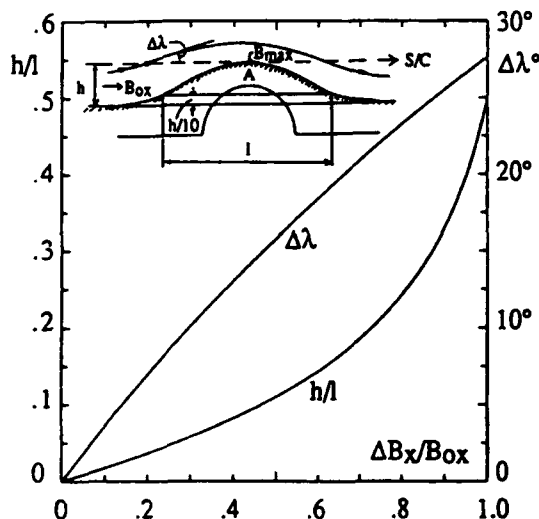

Fig. 3. Field-line aspect ratio, h/l, and maximum deflection angle, $\Delta\lambda$, as a function of maximum increase in transverse field, ΔB_x, for Farrugia et al. [1987] model. Field maximum occurs at A.

transverse to the flux tube, a constant field, B_{oz}, along the tube, and a two-dimensional dipole field, representing the field perturbation caused by the tube. This configuration has a field maximum immediately above the tube. Using this simple model, we can estimate the field-line deformation needed to increase the transverse field by an observed amount. The result is shown in Figure 3 in which the ratio of height to length, h/l, of a draped field-line surface through the field-

maximum point, A, is shown as a function of, $\Delta B_x/B_{ox}$, the ratio of the enhancement of the transverse field component to the ambient value of that component. Also shown is the maximum transverse field-angle change, $\Delta\lambda$, observed by a spacecraft as it travels parallel to the magnetopause towards the field maximum. It is seen that even gentle bending of the field-line surfaces may lead to a substantial field increase. In the October 8, 1985, event, a field increase from 60 nT to 70 nT is observed. Minimum-variance analysis of the magnetic-field data in the interval 0853:00-0856:48 UT indicates that most of this field was in the transverse (x) direction. Figure 3 shows that such an increase could be produced by a curved field-line surface having aspect ratio $h/l = 1/33$, with a maximum observed field deflection of $\Delta\lambda = 6°$ occurring well before the field maximum is reached. A negative deflection in λ_B of this order of magnitude is in fact seen to precede the field maximum (panel 4 of Figure 2).

Even near local noon, it is not surprising to find the MP to experience frequent undulations of this magnitude: multiple encounters of a spacecraft with the LLBL/MP would be a natural consequence. Thus Type II behavior should, and indeed frequently is observed to, accompany such multiple encounters (e.g., Figure 9 of Neugebauer et al. [1974]).

References

Cowley, S.W.H., Magnetic and ionospheric flow and the interplanetary magnetic field, in *The Physical Basis of the Ionosphere in the Solar-Terrestrial System*, p. 4-1, AGARD-CP, NATO, Neuilly-sur-Seine, 1981.

Farrugia, C.J., R.C. Elphic, D.J. Southwood, and S.W.H. Cowley, Field and flow perturbations outside the reconnected field line region in flux transfer events: Theory, *Planet. Space Sci.*, *35*, 227-240, 1987.

Hall, D.S., C.P. Chaloner, D.A. Bryant, D.R. Lepine, and V.P. Tritakis, Electrons in the boundary layers near the dayside magnetopause, *J. Geophys. Res.*, *96*, 7869, 1991.

Kan, J.R., A theory of patchy and intermittent reconnections for magnetospheric flux transfer events, *J. Geophys. Res.*, *93*, 5613, 1988.

Neugebauer, M., C.T. Russell, and E.J. Smith, Observations of the internal structure of the magnetopause, *J. Geophys. Res.*, *79*, 499, 1974.

Sonnerup, B.U.Ö., and B.G. Ledley, Electromagnetic structure of the magnetopause and boundary layer, in *Magnetospheric Boundary Layers*, edited by B. Battrick, pp. 401-411, ESA SP-148 European Space Agency, Paris, 1979.

B. Sonnerup, Thayer School of Engineering, Dartmouth College, Hanover, NH 03755.

G. Paschmann, and T.-D. Phan, Max-Planck-Institut für extraterrestrische Physik, 8046 Garching, Germany.

H. Lühr, Institut für Geophysik und Meteorologie der Technischen Universität Carolo-Wilhelmina, 3300 Braunschweig, Germany.